U.S.NRC
United States Nuclear Regulatory Commission
Protecting People and the Environment

NUREG/CR-7191

Thermal Analysis of Horizontal Storage Casks for Extended Storage Applications

Office of Nuclear Regulatory Research

AVAILABILITY OF REFERENCE MATERIALS IN NRC PUBLICATIONS

NRC Reference Material

As of November 1999, you may electronically access NUREG-series publications and other NRC records at NRC's Public Electronic Reading Room at http://www.nrc.gov/reading-rm.html. Publicly released records include, to name a few, NUREG-series publications; *Federal Register* notices; applicant, licensee, and vendor documents and correspondence; NRC correspondence and internal memoranda; bulletins and information notices; inspection and investigative reports; licensee event reports; and Commission papers and their attachments.

NRC publications in the NUREG series, NRC regulations, and Title 10, "Energy," in the *Code of Federal Regulations* may also be purchased from one of these two sources.

1. The Superintendent of Documents
   U.S. Government Printing Office
   Mail Stop SSOP
   Washington, DC 20402–0001
   Internet: bookstore.gpo.gov
   Telephone: 202-512-1800
   Fax: 202-512-2250
2. The National Technical Information Service
   Springfield, VA 22161–0002
   www.ntis.gov
   1–800–553–6847 or, locally, 703–605–6000

A single copy of each NRC draft report for comment is available free, to the extent of supply, upon written request as follows:

Address: U.S. Nuclear Regulatory Commission
Office of Administration
Publications Branch
Washington, DC 20555-0001
E-mail: DISTRIBUTION.RESOURCE@NRC.GOV
Facsimile: 301–415–2289

Some publications in the NUREG series that are posted at NRC's Web site address http://www.nrc.gov/reading-rm/doc-collections/nuregs are updated periodically and may differ from the last printed version. Although references to material found on a Web site bear the date the material was accessed, the material available on the date cited may subsequently be removed from the site.

Non-NRC Reference Material

Documents available from public and special technical libraries include all open literature items, such as books, journal articles, transactions, *Federal Register* notices, Federal and State legislation, and congressional reports. Such documents as theses, dissertations, foreign reports and translations, and non-NRC conference proceedings may be purchased from their sponsoring organization.

Copies of industry codes and standards used in a substantive manner in the NRC regulatory process are maintained at—

The NRC Technical Library
Two White Flint North
11545 Rockville Pike
Rockville, MD 20852–2738

These standards are available in the library for reference use by the public. Codes and standards are usually copyrighted and may be purchased from the originating organization or, if they are American National Standards, from—

American National Standards Institute
11 West 42nd Street
New York, NY 10036–8002
www.ansi.org
212–642–4900

Legally binding regulatory requirements are stated only in laws; NRC regulations; licenses, including technical specifications; or orders, not in NUREG-series publications. The views expressed in contractor-prepared publications in this series are not necessarily those of the NRC.

The NUREG series comprises (1) technical and administrative reports and books prepared by the staff (NUREG–XXXX) or agency contractors (NUREG/CR–XXXX), (2) proceedings of conferences (NUREG/CP–XXXX), (3) reports resulting from international agreements (NUREG/IA–XXXX), (4) brochures (NUREG/BR–XXXX), and (5) compilations of legal decisions and orders of the Commission and Atomic and Safety Licensing Boards and of Directors' decisions under Section 2.206 of NRC's regulations (NUREG–0750).

U.S.NRC
United States Nuclear Regulatory Commission
Protecting People and the Environment

NUREG/CR-7191

Thermal Analysis of Horizontal Storage Casks for Extended Storage Applications

Manuscript Completed: February 2014
Date Published: December 2014

Prepared by:
Kaushik Das, Debashis Basu, and Gary Walter

Center for Nuclear Waste Regulatory Analyses
Southwest Research Institute®
6220 Culebra Road
San Antonio, TX 78238-5166

S. Gonzalez, NRC Project Manager
A. Velazquez-Lozada, NRC Project Manager
G. Zigh, NRC Technical Lead

Office of Nuclear Regulatory Research

ABSTRACT

A computational fluid dynamics (CFD) model that can be used to reliably predict temperature distributions for long-term storage was developed for the ventilated horizontal dry storage system containing pressurized water reactor (PWR) fuel at the Calvert Cliffs Independent Spent Fuel Storage Installation (ISFSI). The model was developed systematically by (i) constructing a three dimensional (3-D) model for two horizontal modules at this ISFSI, (ii) comparing model results with measured temperature data, (iii) performing a parametric analysis to assess the impact of model inputs on temperature predictions, (iv) using the developed model to predict temperature distributions of critical components for a storage period of 300 years, and (v) conducting numerical uncertainty analyses of the solutions using the grid convergence index (GCI) method.

Three-dimensional (3-D) numerical models were developed using the commercial CFD software FLUENT, Version 14.5 [ANSYS Inc. 2012]. The horizontal storage modules (HSM) modeled in the analysis are the HSM–1 and HSM–15 units at Calvert Cliffs. Each of the storage modules contains a horizontal dry shielded canister (DSC) loaded with 24 fuel assemblies. The concrete storage units and DSC internal structures such as spacer plates, tie rods, fuel assemblies, and supporting rails were included in the model. Individual fuel rods were not explicitly modeled; instead, the volume within each fuel assembly was represented as a porous medium with specified frictional and inertial flow resistances to helium movement. An orthotropic temperature-dependent equivalent thermal conductivity was used to model conductive and radiative heat transfer in the porous zone. The discrete ordinate (DO) model was used for radiation, while the low Reynolds number k-ε model with buoyancy was used to simulate turbulence.

The baseline simulations were compared to measured temperature data for the HSM–1 and HSM–15 units from June 27 and 28, 2012 [Suffield et al. 2012]. The steady state temperature distributions on different components of the storage modules, and the corresponding air and helium circulation patterns, were calculated using ambient conditions representative of the measurement period. The models predicted a high-temperature region on the upper half of the curved surface of the DSC shell, resulting from a combination of temperature-driven natural convection flow of the helium coolant inside the DSC and buoyancy-driven upward flow of heated air around the DSC. Computed temperatures at selected locations on the DSC shell were compared with measured data. The simulated temperatures for both modules were, higher than the measured values, but the agreement between the modeled and measured data was better near the end cap of the DSC shell. Aspects of the temperature data collection suggest that there were a number of uncertainties involved with the method used for temperature measurement and the observed values were not representative of a normally operated closed module.

Sensitivity analyses of the simulated results included evaluations of the near wall mesh refinement, turbulence model, porous media resistance, insolation, and evaluation of the heat transfer coefficient using an extended domain analysis. The study showed that near wall mesh refinement above the baseline mesh had minimal impact on the temperature distribution. Therefore, the baseline mesh was deemed adequate to perform the benchmark studies, other parametric analyses, and the 300-year thermal evolution study. The turbulence models evaluated included the standard k-ε model, low Reynolds number k-ε model, standard SST k-ω model, and SST k-ω model with buoyance effects. Among the studied turbulence models, simulated results with the low Reynolds number k-ε model predicted the lowest temperatures. The study of porous media resistance showed that as long as some flow resistance exists within the porous zone of the fuel assemblies, the temperature distribution is not very sensitive to the

specified porous media resistance; however, the fundamental pattern of temperature distribution is altered if resistance is completely eliminated from this zone. Accordingly, reasonable resistance coefficients are necessary in this zone in order to accurately capture the temperature field. The sensitivity study also showed that insolation impacts the temperatures calculated on the internal components by a few degrees. To obtain an independent verification of the heat transfer coefficient on the exposed concrete surface of the module, a simulation was performed using an extended domain that included the surrounding atmosphere. Results indicated that the heat transfer coefficients used for the baseline simulation were reasonable.

The 300-year simulations for both the HSM–1 and HSM–15 configurations showed that (i) the drop in maximum cladding temperature along the profile is relatively rapid in the first 100 years and becomes more gradual thereafter and (ii) the minimum cladding temperature varies by a small amount as time progresses. All the component temperatures showed an asymptotic decline towards the ambient temperature over time.

The GCI method developed by Roache [1998, 2003] and adopted in the ASME standard V&V 20-2009 [Celik et al. 2008; ASME 2009] was used to calculate the observed order of accuracy and associated numerical uncertainty for the simulated results. Four levels of computational grids were used in the GCI analysis. The simulated results obtained from the different grid levels showed little variation. The apparent order of accuracy calculated using different combinations of solutions was not constant, which can be attributed to minor numerical oscillations in the results and possibly round-off errors. An alternative estimate of numerical uncertainty was made using an order of accuracy of 1 and a higher factor of safety. From this estimation, it was found that the GCI is less than 4 percent, indicating that there was no significant deviation of the predicted variables due to mesh refinement.

TABLE OF CONTENTS

Section Page

ABSTRACT iii
TABLE OF CONTENTS v
LIST OF FIGURES ix
LIST OF TABLES xv
EXECUTIVE SUMMARY xvii
ACKNOWLEDGMENTS xxi
ABREVIATIONS AND ACRONYMS xxiii

1. INTRODUCTION 1-1
   1.1 Regulatory and Technical Background 1-1
   1.2 Brief Literature Survey 1-1
   1.3 Objective and Scope of Work 1-3
   1.4 Description of the Dry Cask Storage Modules (HSM–1 and HSM–15) 1-3

2. NUMERICAL MODELING METHODS 2-1
   2.1 ANSYS-FLUENT Fluid Flow Solver 2-1
   2.2 Governing Equations 2-1
      2.2.1 Continuity and Momentum Equations 2-1
      2.2.2 Energy Equation 2-2
   2.3 Solid Modeling and Mesh Generation for HSM–1 and HSM–15 2-3
      2.3.1 Grid Generation 2-4
   2.4 Boundary and Operating Conditions 2-7
   2.5 Numerics, Radiation Heat Transfer, and Turbulence Models for the Simulations 2-12
   2.6 Fuel Assembly Model 2-13
      2.6.1 Porous Media Calculation 2-13
      2.6.2 Effective Thermal Conductivity Calculation 2-13
      2.6.3 Fuel Assembly Loading 2-14
   2.7 Material Properties Used in the Simulations 2-14

3. BENCHMARK MODELING AND SENSITIVITY ANALYSES 3-1
   3.1 Description of Field Temperature Measurement 3-1
   3.2 Results of Baseline Simulations 3-1
      3.2.1 HSM–1 3-1
         3.2.1.1 Temperature and Velocity Patterns 3-2
         3.2.1.2 Temperature Line Probes 3-4
         3.2.1.3 Comparison With Measured Data 3-11
      3.2.2 HSM–15 3-14
         3.2.2.1 Temperature Field 3-14
         3.2.2.2 Velocity Field 3-19
         3.2.2.3 Comparison with Measured Data 3-19
   3.3 Sensitivity Studies 3-19
      3.3.1 Effect of Mesh Refinement 3-21
      3.3.2 Effect of Turbulence Models 3-22
      3.3.3 Effect of Porous Media Resistance 3-27
      3.3.4 Effect of Insolation 3-31
      3.3.5 Effect of Including the Surrounding Atmosphere in the Computational Domain 3-33

TABLE OF CONTENTS
(continued)

Section Page

3.4 Observations From Benchmark Study....3-36

4. THERMAL EVOLUTION SIMULATIONS....4-1
4.1 Numerical Approach to Thermal Evolution Analysis....4-1
4.2 Results of Thermal Evolution Simulations....4-1
4.3 Observations from the Thermal Evolution Study....4-16

5. UNCERTAINTY QUANTIFICATION AND GRID CONVERGENCE INDEX (GCI) ANALYSIS....5-1
5.1 Uncertainty Analysis: Definitions and Concepts....5-1
5.1.1 Code Validation....5-1
5.1.2 Code Verification....5-2
5.1.3 Solution Verification....5-2
5.2 Grid Convergence Index Calculation Method....5-3
5.3 Uncertainty Quantification and GCI Analysis for HSM–1 Module....5-5
5.3.1 Assessment of Asymptotic Behavior of the Solution....5-9
5.3.2 Iteration Convergence....5-11
5.3.3 Other Numerical Issues....5-11
5.3.4 Modified Estimation of GCI for HSM-1....5-14
5.4 Uncertainty Quantification and GCI Analysis for HSM–15 Module....5-14
5.5 Observations from GCI Analysis....5-18

6. SUMMARY AND CONCLUSIONS....6-1
6.1 Baseline Simulations and Comparison of Simulated to Measured Temperatures....6-1
6.2 Sensitivity Analyses....6-2
6.3 Simulation of Long-Term Storage Conditions....6-3
6.4 Uncertainty Analysis....6-3

7. REFERENCES....7-1

APPENDIX A: NATURAL CONVECTION CORRELATION AND MODEL FOR VENT SCREENS AT INLET....A–1
A.1 Natural Convection Correlation....A–1
A.1.1 Correlations for Vertical Flat Plates....A–2
A.1.2 Correlation for Horizontal Flat Plates....A–3
A.2 Modeling of Vents Screens at Inlet....A–3

APPENDIX B: MATERIAL PROPERTIES USED IN THE SIMULATIONS....B–1

APPENDIX C: POROUS MEDIA MODEL....C–1

TABLE OF CONTENTS
(continued)

Section Page

APPENDIX D: CALCULATION OF FUEL EFFECTIVE THERMAL CONDUCTIVITY D–1
D.1 Radial Thermal Conductivity D–1
D.2 Axial Thermal Conductivity..... D–3

APPENDIX E: FUEL ASSEMBLY LOADING..... E–1

LIST OF FIGURES

Figure		Page
1-1	NUHOMS horizontal storage modules in Calvert Cliffs Nuclear Power Station ISFSI	1-4
1-2	The concrete storage module and DSC shell with support rail for unit HSM–1	1-5
1-3	DSC sell and internal components: spacer plates, fuel assemblies and tie rods for units HSM–1	1-5
2-1	Aerial view of the Calvert Cliffs Nuclear Power Station ISFSI housing HSM–1 and HSM–15 modules	2-3
2-2	Schematics showing the geometry of the DSC	2-4
2-3	Three-dimensional schematic view of the HSM–1 module	2-5
2-4	Three-dimensional view of the DSC internal showing the support rod, guide sleeve, spacer disk, and guide rails	2-5
2-5	Three-dimensional schematic for the fuel assemblies, tie rods, and spacer plates within the DSC shell	2-6
2-6	Two-dimensional cross-sectional view showing the computational grid for the fuel region	2-6
2-7	Three-dimensional view of the computational grid (exterior view) of the HSM–1 module	2-8
2-8	Transverse slice through center line showing computational grid of HSM–1, highlighting the airflow path	2-8
2-9	Planar slice through mid-section of the DSC showing computational mesh of HSM–1 module in transverse direction	2-9
2-10	Enlarged view of the computational grid in the guide sleeve, support rod, and spacer plate region	2-9
2-11	Three-dimensional view of the computational grid for the DSC internal and guide rails	2-10
2-12	Three-dimensional view of the DSC internal showing the fuel region, support rod, guide sleeve, spacer disk, and guide rails	2-10
2-13	Fuel assembly loading identification structure for HSM–1 module	2-15
2-14	Fuel assembly loading identification structure for HSM–15 module	2-15
3-1	Axial and transverse cross-sectional planes used to illustrate temperature and velocity distributions	3-2
3-2	Contours of DSC shell surface temperature for HSM–1 baseline case	3-3
3-3	Temperature distributions for the fuel region, spacer plates, and support rods for HSM–1 baseline case	3-3
3-4	Air and helium temperature distributions along transverse cross section for HSM–1 baseline case	3-5
3-5	Temperature distribution for the solid region at transverse cross section for HSM–1 baseline case	3-5
3-6	Temperature distribution for the fluid region along the axial cross-sectional plane for HSM–1 baseline case	3-6
3-7	Temperature distribution for the solid region along the axial cross-sectional plane the HSM–1 module	3-6
3-8	Streamlines showing the airflow path and airflow circulation within the HSM–1 module	3-7
3-9	Velocity vectors at the mid-plane in the transverse cross section for HSM–1	3-7

LIST OF FIGURES
(continued)

Figure — Page

3-10 Velocity vectors at the axial cross section for HSM–1 module 3-8
3-11 Line probe locations for extracting temperature distribution along the axial direction: locations shown on the DSC shell and on the heat shield 3-8
3-12 Line probe locations for extracting temperature distribution along the axial direction in the fuel region: locations shown for fuel assemblies 1 and 23 3-9
3-13 Computed temperature distributions along the axial distance for top of DSC shell and right of DSC shell 3-10
3-14 Computed temperature distributions along the axial distance for top of heat shield and right of heat shield 3-10
3-15 Computed temperature distributions along the axial distance for fuel region: distribution shown for fuel assemblies 1 and 23 for HSM–1 baseline case 3-11
3-16 Thermocouple locations shown at 0.0-, 0.51-, and 1.02-m axial distance 3-12
3-17 Thermocouple locations shown at the top, right side, left side, rail right, and rail left 3-13
3-18 Contours of DSC shell surface temperature for HSM–15 baseline case 3-15
3-19 Temperature distributions for the fuel assembly, spacer plates, and support rod for HSM–15 baseline case....3-15
3-20 Air and helium temperature distributions along transverse cross section for HSM–15 baseline case....3-16
3-21 Solid region (concrete, spacer plates) temperature distributions at the transverse cross section for HSM–15 baseline case....316
3-22 Temperature distribution for air and helium at axial cross-sectional plane for HSM–15 baseline case....3-17
3-23 Temperature distribution for the solid regions at axial cross-sectional plane for HSM–15 baseline case....3-17
3-24 Computed temperature distributions along the axial distance for top and right of DSC shell for HSM–15 module 3-18
3-25 Computed temperature distributions along the axial distance for top of heat shield and right of heat shield 3-18
3-26 Computed temperature distributions along the axial distance for fuel region: distribution shown for fuel assemblies 1 and 23 for HSM–15 baseline case 3-19
3-27 Streamlines showing the airflow path and airflow circulation within the HSM–15 module....3-20
3-28 Velocity vector distribution at the transverse cross section for HSM–15 module....3-20
3-29 Velocity distribution at the axial cross section for HSM–15 module....3-21
3-30 Computed temperature distributions along the axial distance for right side of DSC shell: mesh refinement for HSM–1 module....3-23
3-31 Computed temperature distributions along the axial distance for top of DSC shell: mesh refinement for HSM–1 module....3-23
3-32 Computed temperature distributions along the axial distance for fuel assembly 1: mesh refinement for HSM–1 module 3-24
3-33 Computed temperature distributions along the axial distance for right side of DSC shell: effect of turbulence model for HSM–1 module 3-25
3-34 Computed temperature distributions along the axial distance for top of DSC shell: effect of turbulence models for HSM–1 module....3-26

LIST OF FIGURES
(continued)

Figure Page

3-35 Computed temperature distributions along the axial distance for fuel assembly 1: effect of turbulence model for HSM–1 module 3-26
3-36 Computed temperature distributions along the axial distance for fuel assembly 23: effect of turbulence model for HSM–1 module 3-27
3-37 Computed temperature distributions along the axial distance for right side of DSC shell: effect of porous media for HSM–1 module 3-28
3-38 Computed temperature distributions along the axial distance for top of DSC shell: effect of porous media for HSM–1 module 3-29
3-39 Computed temperature distributions along the axial distance for fuel assembly 1: effect of porous media for HSM–1 module....3-29
3-40 Computed temperature distributions along the axial distance for fuel assembly 23: effect of porous media for HSM–1 module....3-30
3-41 Computed temperature distributions along the axial distance for right side and top of DSC shell: effect of insolation for HSM–1 module....3-32
3-42 Computed temperature distributions along the axial distance for fuel assemblies 1 and 23: effect of insolation for HSM–1 module....3-32
3-43 Extended domain for the study of the effect of atmosphere for HSM–1 module....3-34
3-44 Temperature contours at an axial mid-plane of the extended domain: effect of atmosphere for HSM–1 module 3-35
3-45 Velocity contours at an axial mid-plane of the extended domain: effect of atmosphere for HSM–1 module 3-35
3-46 Computed heat transfer coefficient distribution over the HSM–1 module: effect of extended domain and atmosphere....3-36

4-1 Variation of maximum and minimum cladding temperature over 300 years for HSM–1 module....4-5
4-2 Variation of maximum and minimum fuel sleeve temperature over 300 years for HSM–1 module....4-5
4-3 Variation of maximum and minimum spacer plates temperature over 300 years for HSM–1 module....4-6
4-4 Variation of maximum and minimum DSC shell temperature over 300 years for HSM–1 module....4-6
4-5 Variation of maximum and minimum heat shield temperature over 300 years for HSM–1 module....4-7
4-6 Air and helium temperature distributions at a transverse plane for HSM–1: year 1993....4-7
4-7 Air and helium temperature distributions at a transverse plane for HSM–1: year 2093 (100 years after storage)....4-8
4-8 Air and helium temperature distributions at a transverse plane for HSM–1: year 2193 (200 years after storage)....4-8
4-9 Air and helium temperature distributions at a transverse plane for HSM–1: year 2193 (300 years after storage)....4-9

LIST OF FIGURES
(continued)

Figure — Page

4-10 Variation of maximum and minimum cladding temperature over 300 years for HSM–15 module....4-9
4-11 Variation of maximum and minimum fuel sleeve temperature over 300 years for HSM–15 module....4-10
4-12 Variation of maximum and minimum spacer plates temperature over 300 years for HSM–15 module....4-10
4-13 Variation of maximum and minimum DSC shell temperature over 301 years for HSM–15 module....4-11
4-14 Variation of maximum and minimum heat shield temperature over 301 years for HSM–15 module....4-11
4-15 Air and helium temperature distributions at a transverse plane for HSM–15: year 1996....4-12
4-16 Air and helium temperature distributions at a transverse plane for HSM–15: year 2097 (101 years after storage)....4-12
4-17 Air and helium temperature distributions at a transverse plane for HSM–15: year 2197 (201 years after storage)....4-13
4-18 Air and helium temperature distributions at a transverse plane for HSM–15: year 2297 (301 years after storage)....4-13

5-1 Temperature contours along the mid-plane for four mesh levels for simulations of HSM–1 at year 1993....5-7
5-2 Deviation of temperature values calculated at different mesh levels for HSM–1: deviations are calculated as percentage of fine mesh temperatures....5-8
5-3 Calculated apparent order using different mesh levels for HSM–1....5-10
5-4 Distribution of discretization error with mesh refinement for HSM–1....5-11
5-5 Variation of convergence coefficient with mesh refinement for HSM–1....5-12
5-6 Variation of average temperature of selected monitor points with iteration, showing overall convergence....5-12
5-7 Variation of average temperature of selected monitor points with iteration for last 6,000 iterations, highlighting minor oscillations....5-13
5-8 Deviation of temperature values calculated at different mesh levels for HSM–15: deviations are calculated as percentage of fine mesh temperatures....5-16
5-9 Calculated apparent order using different mesh levels for HSM–15....5-17
5-10 Distribution of discretization error with mesh refinement for HSM–15....5-17
5-11 Variation of convergence coefficient with mesh refinement for HSM–15....5-19

C–1 Longitudinal full view of the computational domain for the CE 14 × 14 fuel assembly for porous media parameter calculation showing the fuel rod....C–2
C–2 $1/4^{th}$ cross-sectional domain for the CE 14 × 14 fuel assembly for porous media parameter calculation....C–2
C–3 Two-dimensional view of the computational domain for the CE 14 × 14 fuel assembly for porous media parameter calculation....C–3

D–1 Computational domain and grid for fuel, clad, and helium gas grids in the effective thermal conductivity calculation....D–2
D–2 Predicted temperature contours for an edge temperature of 300 K [80.3 °F]....D–2

LIST OF FIGURES
(continued)

Figure		Page
E–1	Fuel assembly loading identification structure for HSM–1 module	E–2
E–2	Fuel assembly loading identification structure for HSM–15 module	E–2
E–3	Axial distribution of the peaking factor used in current simulations	E–4

LIST OF TABLES

Table		Page
2-1	Total number of cells for different grid levels used in the GCI study	2-11
3-1	Comparison of measured and predicted temperatures for the baseline case simulations for HSM–1 module	3-12
3-2	Computational mesh used in the mesh refinement study	3-24
3-3	Comparison of predicted temperatures for the three different levels of mesh: simulations for HSM–1 module	3-24
3-4	Comparison of predicted temperatures for different turbulence models: simulations for HSM–1 module	3-28
3-5	Resistance coefficients used porous media resistance parametric study	3-30
3-6	Comparison of predicted temperatures (K) for different porous media resistance values: simulations for HSM–1 module	3-31
3-7	Comparison of predicted temperatures (K) for with and without insolation: simulations for HSM–1 module	3-34
4-1	Calculated decay heat load values at different year for HSM–1 module	4-2
4-2	Calculated decay heat load values at different year for HSM–15 module	4-3
4-3	Calculated temperature values at different years for HSM–1 module	4-14
4-4	Calculated temperature values at different years for HSM–15 module	4-15
5-1	Mesh levels used in GCI analysis of HSM–1 module	5-6
5-2	Computed maximum and minimum cladding temperature for HSM–1 module (1993)	5-8
5-3	Computed maximum and minimum cladding temperature for HSM–1 module (2012)	5-8
5-4	Computed maximum and minimum cladding temperature for HSM–1 module (2093)	5-8
5-5	Apparent order (p) and calculated GCI for HSM–1 module	5-9
5-6	GCI value for a conservative bounded value of p = 1 for HSM–1 module	5-15
5-7	Mesh levels used in GCI analysis of HSM–15 module	5-15
5-8	Computed maximum and minimum cladding temperature for HSM–15 module (1996)	5-15
5-9	Computed maximum and minimum cladding temperature for HSM–15 module (2012)	5-15
5-10	Computed maximum and minimum cladding temperature for HSM–15 module (2097)	5-15
5-11	Apparent order (p) and calculated GCI for HSM–15 module	5-17
5-12	GCI value for a conservative bounded value of p = 1 for HSM–15 module	5-19
B–1	Properties of air used in the simulations	B–1
B–2	Properties of helium used in the simulations	B–1
B–3	Properties of concrete used in the simulations	B–1
B–4	Properties of carbon steel used in the simulations	B–1
B–5	Properties of stainless steel used in the simulations	B–2
B–6	Properties of lead used in the simulations	B–2
B–7	Emissivity of materials used in the simulations	B–2

LIST OF TABLES
(continued)

Table		Page
C–1	Dimensions used in the simulations	C–3
C–2	Inlet condition and parameters for calculations of loss factors	C–4
D–1	K_{eff} of fuel region in the radial direction with helium backfill	D–3
D–2	K_{eff} of fuel region in the axial direction with helium backfill	D–3
E–1	Calculated decay heat load values at year 2012 for HSM–1 module	E–3
E–2	Calculated decay heat load values at year 2012 for HSM–15 module	E–3

EXECUTIVE SUMMARY

The U.S. Nuclear Regulatory Commission (NRC) regulates storage of spent nuclear fuel (SNF) from commercial nuclear power plants. An increasing amount of the SNF is in dry storage systems, mostly at current and decommissioned plants. The existing regulatory framework in the Code of Federal Regulations (CFR) for storage (10 CFR 72) and transportation (10 CFR 71) of SNF supports dry cask storage for at least 80 years (i.e., a 40-year initial licensing term, followed by a license renewal for a term of up to 40 years, although many of the existing facilities were licensed for an initial term of 20 years under the regulations in place at the time). The NRC staff is currently considering the performance of storage systems over an initial 300-year period following discharge of the SNF from the reactor, in advance of potential changes to the existing regulatory framework.

This report describes an independent computational analysis designed to predict the thermal behavior of dry cask storage systems for periods of up to 300 years. The simulations were performed for ventilated dry cask horizontal storage modules HSM–1 and HSM–15 at the Calvert Cliffs Independent Spent Fuel Storage Installation (ISFSI). Three-dimensional (3-D) numerical simulations were performed using the computational fluid dynamics (CFD) software ANSYS-FLUENT® Version 14.5 [ANSYS 2012]. Initially, a baseline model of the storage modules was developed, and the results highlighted the general pattern of the flow and temperature fields within the storage units. Temperature values calculated from the baseline study were compared with available measured data. Subsequently, a sensitivity study was conducted to understand the effects on the numerical solutions of different modeling parameters, such as the turbulence model, porous media resistance, and insolation. The baseline computational model was then used to predict the thermal behavior of the dry storage modules over 300 years of storage. Finally, a study to quantify numerical uncertainty was performed using the grid convergence index (GCI) method.

The HSM–1 and HSM–15 ventilated dry cask storage modules each contain a dry shield canister (DSC) that is loaded horizontally. The DSC shell holds 24 fuel assemblies, each containing an arrangement of Combustion Engineering (CE) 14 × 14 fuel rods. The void spaces within the DSC shell contain helium as a coolant, maintained above atmospheric pressure. Ambient air enters the base of each storage module, passes over the surface of the DSC shell, and exits from vents at the top of the module. The 3-D computational model developed in this study explicitly includes the concrete storage units and DSC shells, along with internal structures such as spacer plates, tie rods, fuel assemblies, and the supporting rails. The individual fuel rods within an assembly were not explicitly represented; instead, the volume within each fuel assembly was modeled as a porous medium to represent flow of the helium coolant. Inertial and frictional flow resistance factors, which were obtained using a separate 3-D CFD model of the fuel assembly, were specified for helium movement in the porous zone as shown in Appendix C. An orthotropic temperature-dependent equivalent thermal conductivity, which was calculated based on the CE 14 × 14 fuel configuration, was used to model the conductive and radiative heat transfer in the porous zone. Hexahedral grids were used to mesh the fluid and solid volumes in the domain. The discrete ordinate (DO) model was used for radiation. The low Reynolds number k-ε model with buoyancy effect consideration was used to simulate turbulence.

All of the simulations used ambient conditions corresponding to June 27 and 28, 2012, when HSM–1 and HSM–15 were opened for temperature measurements. The baseline simulations calculate the steady-state temperature distribution for different components of the storage module and the circulation pattern for ventilation air and the helium coolant. In general, a

high-temperature region resides on the upper half of the curved surface of the DSC shell, resulting from temperature-driven natural convection flow of the helium coolant inside the DSC and the flow of ventilation air around the DSC. Computed temperature values at selected locations on the DSC shell surface were compared with measured data. The computed results were consistently higher than the measured temperatures. Measurement uncertainty may be significant because of the difficult access conditions and exchange of air through the open DSC door, and may have contributed to the differences between computed and measured values.

Once the 3-D baseline model was developed and benchmarked with experimental data, it was used to perform a series of sensitivity studies. The sensitivity studies involved analyzing the effects of near wall mesh refinement, turbulence model, porous media resistance, an extended computational domain, and insolation. The mesh refinement study was done by adapting and refining the mesh near the DSC shell wall. A comparison of temperature distributions among solutions using three levels of adapted mesh showed minimal impacts of near wall refinement. Therefore, the baseline mesh was considered adequate to perform the present analyses. The turbulence models considered in the sensitivity analysis included the baseline low Reynolds number k-ε model, the standard k-ε model with scalable wall function and buoyancy effects, the shear stress transport (SST) k-ω model, and the SST k-ω model with buoyancy effects. A comparison of results obtained using the different turbulence models showed that the low Reynolds number k-ε model predicted the lowest temperatures. To study the sensitivity to the specified porous media resistance, the resistances were increased and decreased by an order of magnitude from the baseline values. It was found that varying the resistances compared to baseline values did not affect the temperature distribution. However, case studies with zero resistance in the porous media and with no porous media assumption predicted a fundamentally altered temperature distribution pattern, indicating that a reasonable specification of porous resistance is necessary to obtain meaningful results. For the sensitivity analysis on the effect of insolation, a simulation was performed with no insolation flux at the boundary wall. Calculated temperatures on the DSC shell with no insolation were found to be lower than the baseline simulation results by a few degrees, indicating that insolation minimally impacts the internal component temperatures within the storage system. An analysis was performed to assess the validity of the convective heat transfer coefficient specified at the outer exposed boundary walls by extending the computational domain to include the surrounding atmosphere. It was found that the average convective heat transfer coefficient calculated from the extended domain calculation was comparable to the specified value at the boundaries of the baseline case.

The baseline computational model was used to predict the long-term (300 years) thermal behavior of the dry storage casks. Multiple steady-state cases were simulated at discrete time points. For the first 100 years, steady-state simulations were performed at 5-year intervals, dropping to 10-year intervals thereafter. In both the HSM–1 and HSM–15 configurations, (i) the drop in maximum cladding temperature along the profile is relatively rapid in the first 100 years and becomes more gradual thereafter and (ii) the minimum cladding temperature drops to a few degrees above the ambient temperature within 100 years. All of the component temperatures show an asymptotic decrease with time.

The GCI method, applied to evaluate numerical uncertainty in the simulations, uses the Richardson extrapolation approach to quantify the discretization error of the computed solution. Four levels of computational grids were used in the analysis: the baseline grid, a coarser grid, and two levels of finer grids. Maximum and minimum cladding temperatures were used as target variables to estimate the uncertainty of the numerical simulations. These variables were selected as representative parameters because other component temperatures follow the same pattern over time. The calculated results obtained from different grid levels showed almost no variation. The minor variation between values could be attributed to effects such as machine

round-off error. The apparent order of accuracy calculated using different combinations of solutions was not constant, and was larger than the theoretical order of accuracy in many of the cases. It appears that the small differences in temperature among different mesh levels disproportionally affected some terms associated with the calculation of apparent order, yielding an artificially high value. The calculation of order p was also affected by minor oscillations of the results, even when overall convergence was achieved. To provide an estimate of numerical uncertainty, a theoretical order of accuracy of p = 1 was used with a higher factor of safety of 3. It was found that the GCI is less than 4 percent, indicating that there was no significant deviation due to mesh refinement.

ACKNOWLEDGMENTS

The authors gratefully acknowledge S. Stothoff for his technical review, G. Wittmeyer and D. Pickett for programmatic reviews, L. Mulverhill for her editorial review, A. Ramos for his administrative support, and G. Zigh and J. Solis for technical guidance. ANSYS Inc. is also acknowledged for its advice and help in ANSYS-FLUENT related issues used in this study.

QUALITY OF DATA, ANALYSES, AND CODE DEVELOPMENT

DATA: All CNWRA-generated original data contained in this report meet quality assurance requirements described in the Geosciences and Engineering Division Quality Assurance Manual. Sources of other data should be consulted for determining the level of quality of those data.

ANALYSES AND CODES: The general purpose computational fluid dynamics simulation code ANSYS® FLUENT™ Version 14.5 [ANSYS Inc. 2012a] was used to generate results for this report and is controlled in accordance with the CNWRA Technical Operating Procedure (TOP)–018, Development and Control of Scientific and Engineering Software. Post-processing was done using TECPLOT® 360™ Version 2009 [TECPLOT Inc. 2009] and ANSYS CFDPOST [ANSYS 2012b].

ABBREVIATIONS AND ACRONYMS

2-D	two-dimensional
3-D	three-dimensional
ASME	American Society of Mechanical Engineers
CE	Combustion Engineering
CFD	computational fluid dynamics
CFR	Code of Federal Regulations
CNWRA	Center for Nuclear Waste Regulatory Analyses
DO	discrete ordinate
DOE	U.S. Department of Energy
DSC	dry storage cask
EPRI	Electric Power Research Institute
GCI	grid convergence index
HSM	horizontal storage module
ISFSI	Independent Spent Fuel Storage Installation
LES	large eddy simulation
MMS	method of manufactured solution
NMSS	Office of Nuclear Material Safety And Safeguards
NRC	U.S. Nuclear Regulatory Commission
RES	Office of Nuclear Regulatory Research
ORNL	Oak Ridge National Laboratory
PDE	partial differential equations
PNNL	Pacific Northwest National Laboratory
PWR	pressurized water reactor
RE	Richardson extrapolation
RMS	root mean square
RTD	resistance temperature detector
RTE	radiative transfer equation
SFS	spent fuel storage
SNF	spent nuclear fuel
SSC	structures, systems, and components
SST	shear stress transport
V&V	verification and validation

1. INTRODUCTION

1.1 Regulatory and Technical Background

The U.S. Nuclear Regulatory Commission (NRC) regulates storage of spent nuclear fuel (SNF) from commercial nuclear power plants. The existing NRC regulatory framework for storage and transportation of SNF is specified in Title 10 of the Code of Federal Regulations (CFR) Part 72, "Licensing Requirements for the Independent Storage of Spent Nuclear Fuel, High-Level Radioactive Waste, and Reactor-Related Greater than Class C Waste" and 10 CFR Part 71, "Packaging and Transportation of Radioactive Material," respectively. The current regulatory framework supports at least the first 80 years of dry cask storage (i.e., a 40-year initial licensing term, followed by a license renewal for a term of up to 40 years), although many of the existing facilities were licensed for an initial term of 20 years under the regulations in place at the time. As directed by the Commission [in SRM–COMSECY–10–0007, December 6, 2010][1] in expectation of continued use of dry storage for extended periods of time, the NRC staff is examining the technical needs and potential changes to the regulatory framework that may be needed to continue licensing SNF storage over periods beyond 120 years. For this evaluation, the NRC staff has considered performance of the systems over an initial 300-year period following discharge of the SNF from the reactor. Modeling of long-term thermal behavior patterns forms an integral part of this assessment. Improvements in thermal calculations can enhance understanding of both the interior (e.g., fuel and cladding) and exterior (susceptibility of canisters to stress corrosion cracking) performance of system components. There is, therefore, a technical need to assess the thermal behavior of spent fuel canisters for extended periods of storage.

As part of this dry storage evaluation, the NRC Office of Nuclear Material Safety and Safeguards (NMSS) requested support from the NRC Office of Nuclear Regulatory Research (RES) to address the issues related to determining axial and radial temperature distributions of the fuel cladding as a function of time. This task involves performing state-of-the-art modeling of the thermal behavior of fuel in dry cask storage systems for periods of up to 300 years [NRC 2012a]. This research will support risk-informed long-term storage regulations. For the foreseeable future, the staff anticipates dry cask storage will be the industry-preferred alternative for providing (i) additional storage capacity at operating and new reactors and (ii) the spent fuel management needs at decommissioned sites or at away-from-reactor sites.

The current work by the Center for Nuclear Waste Regulatory Analyses (CNWRA®) provides technical assistance to the Division of Systems Analysis in RES to support the NRC evaluation of the long-term dry storage of SNF in the area of thermal modeling and uncertainty estimation of thermal models. This activity will help the CNWRA and NRC staffs prepare for potential technical issues related to the thermal behavior of SNF in storage.

1.2 Brief Literature Survey

Heat transfer in the cask is a complicated process because of the geometry of the spent fuel assemblies and dry cask canister, and the combined convection induced by the thermal radiation process [Heng et al. 2002]. Other factors that contribute to the overall heat transfer

[1] **Vietti-Cook, A.L,** "Staff Requirements–COMSECY–10–0007—Project Plan for Regulatory Program Review to Support Extended Storage and Transportation of Spent Nuclear," email communication (December 6, 2010) to R.W. Borchardt, U.S. Nuclear Regulatory Commission, 2010.

include the heat generation by the spent fuel, the ambient thermal boundary conditions, the filling medium within the storage cask, and the vertical or horizontal orientation of the cask. Some of the earliest studies performed in this area of cask modeling [Nishimura et al. 1996; Shibazaki et al. 1998] showed that the convective heat transfer in a storage cask depends on the Grashof number, the Prandtl number, and the relevant geometry parameters. Some of the earliest investigations [Arya and Keyhani 1990; Cannan and Klein 1998] focused on natural convection within the spent fuel assemblies. Gomez et al. [2005] performed two-dimensional (2-D) heat transfer simulations to predict the maximum cladding temperature in a boiling water reactor fuel assembly in a horizontal support basket. Simulated results showed that the predicted maximum cladding temperature is more sensitive to the assumed value of the fuel cladding emissivities when nitrogen is the backfill gas than when helium is used. Heng et al. [2002] found that with an increase in Rayleigh number, the dominant heat transfer mode in the cask changes from conduction to convection. Heng et al. [2002] also determined that at Rayleigh number = 1.3×10^9, turbulent convective heat transfer is so strong that the temperature gradient is very steep near the wall of the cask, and that local convection circulation near the individual guide sleeves and the canister shell is more important to heat transfer than large-scale circulation within the canister. Walavalkar and Schowalter [2004] performed a computational fluid dynamics (CFD) analysis of the VSC–17 spent fuel dry storage system using the FLUENT code with the thermal radiation equations solved for a 90° section of the VSC–17 system.

Zigh and Solis [2008] analyzed the effect of different turbulence models and boundary conditions on modeling uncertainty for the VSC–17 system. The simulations using the low Reynolds number k-ε and the transitional k-ω turbulence models compared well with measured temperatures. The simulation results also identified that the operating density and the ambient pressure significantly influence the results. The porous media model used to simulate the flow inside the storage canister in the current report was based on the approach described by Zigh and Solis [2008]. In previous numerical studies of dry storage canisters at CNWRA, Das et al. [2010] simulated the VSC–17 system and compared the results with available experimental data. The simulated peak cladding temperature was slightly higher than the experimental data. However, the simulated results showed that the match between the computed results and the experimental data was better when nitrogen was used as a backfill gas inside the canister instead of helium.

Hoo et al. [2010] performed FLUENT numerical simulations of thermal hydraulic phenomena in a TN24P cask. They performed a full-scope simulation of the TN24P cask without using the concept of effective thermal conductivity or the porous media approach for the fuel region. The results from the FLUENT simulations were compared with experimental data on COBRA-SFS (Spent Fuel Storage) results. These comparisons showed good agreement with the observed deviation of the peak guide tube temperature, in that the temperature was within the uncertainty range of the thermocouples used in the experiment. However, there were deviations between the FLUENT and COBRA-SFS predicted velocity distributions. Cha et al. [2009] performed a preliminary thermal safety analysis of a commercial dry storage facility designed for the Korea standard SNF, in which they calculated the surface temperature of the storage canister corresponding to the SNF clad temperature.

Banken et al. [2010] used CFD analysis to validate the system designs for SNF storage and transportation applications. They explored the analytical steps necessary to achieve validation of the FLUENT CFD code models against the test results of Transnuclear's SNF dry storage systems and the CFD code model's subsequent implementation in the analysis of another higher capacity system. The analysis found that the choices of meshing scheme,

temperature-dependent thermal properties, and turbulence modeling approach all influence the solution results.

Adkins et al. [2013] presented thermal modeling studies for active storage modules in the Calvert Cliffs Nuclear Power Station Independent Spent Fuel Storage Installation (ISFSI). The thermal analysis was performed using the STAR-CCM+ commercial software, and the models developed for the specific ISFSI modules yielded temperature predictions in actual storage conditions for the concrete structure and the dry shield canister (DSC) and its contents, including preliminary estimates of fuel cladding temperatures for the SNF. The paper also presented a sensitivity analysis on boundary conditions to evaluate the effect of the modeling approach on predicted temperatures and temperature distributions. The results of this work demonstrated that existing CFD modeling tools can be used to obtain reasonable and accurate detailed representations of SNF storage systems with realistic decay heat loadings.

RES recently published NUREG–2152 [NRC 2012b], developed in cooperation with the Division of Spent Fuel Storage and Transportation (SFST) under NMSS. This NUREG provides practical advice and suggestions for reviewing CFD methods used in vendor applications of dry storage casks and for conducting high-fidelity CFD simulations of dry storage cask systems. It outlines procedures, analysis methods, and assumptions used for CFD simulations of dry storage cask systems. The procedures and the guidelines explained in NUREG–2152 for setting up the computational mesh and selecting the numerical schemes and turbulence models were adopted in the current work.

1.3 Objective and Scope of Work

The objective of this work was to realistically model the thermal behavior of SNF in dry cask storage systems for periods of up to 300 years. The model was benchmarked with data from the Calvert Cliffs Nuclear Power Station ISFSI, and parametric studies and uncertainty analyses appropriate to the model were performed. The scope of this investigation consisted of three tasks. Task 1 was development of a three-dimensional (3-D) model of the NUHOMS® ventilated casks in the Calvert Cliffs Nuclear Power Station ISFSI. The model was benchmarked against measured profiles reported by a consortium of organizations including Pacific Northwest National Laboratory (PNNL), Oak Ridge National Laboratory (ORNL), Sandia National Laboratory (SNL), Electric Power Research Institute (EPRI), AREVA, and Constellation Energy [Suffield et al. 2012]. Task 2 consisted of simulating the thermal evolution of the casks for a period of 300 years. The thermal evolution was simulated for a range of heat generation rates from the spent fuel and ambient environmental conditions. Task 3 consisted of an analysis of the uncertainty in the simulation results using the GCI methodology described by ASME [2009].

The results of the analyses are presented and documented so that additional cases covering other dry cask storage system designs can be developed in a consistent manner for future licensing applications.

1.4 Description of the Dry Cask Storage Modules (HSM–1 and HSM–15)

The dry cask storage modules at the Calvert Cliffs Nuclear Power Station ISFSI are a version of the NUHOMS design developed by Transnuclear, Inc., in which the spent fuel is sealed within a DSC that is loaded into a horizontal storage module (HSM). The DSC provides confinement, an inert environment with helium filling the void spaces, structural support, and criticality control for PWR fuel assemblies [Banken et al. 2010]. The horizontal storage module is a reinforced

concrete storage overpack that provides for the passive removal of the spent fuel decay heat, environmental and seismic protection for the DSC, and radiological shielding from the DSC's contents [Banken et al. 2010]. Figure 1-1 shows a typical NUHOMS HSM at the Calvert Cliffs Nuclear Power Station ISFSI. The figure shows the inlet vents and the front cover of the outlet vent structure. This figure also highlights the general arrangement of the storage modules on the ISFSI base pad. The specific storage modules considered in the present analysis are HSM–1 and HSM–15. Both HSM–1 and HSM–15 contain a DSC loaded with 24 CE 14 × 14 assemblies. HSM–1 was loaded in November 1993, and the decay heat load for the DSC in HSM–1 calculated as of June 2012 was 4.1 kW [Suffield et al. 2012]. HSM–15 was loaded in November 1996, and the decay heat load for the DSC in HSM–15 was 10.8 kW at the time of loading and was calculated as 7.6 kW as of June 2012 [Suffield et al. 2012]. HSM–15 is one of the center units in a 2 × 6 array, while HSM–1 is a corner unit.

Figure 1-2 shows the main components of the concrete structure, which has approximately a length of 6.1m [20.1ft], height of 6.5m [21.ft] and a width of 3.2m [10.6ft], (e.g., the air inlet, outlet, and plenum) and the position of the DSC shell. The ventilated storage system depends on natural convection for cooling. Cool air enters the system through the inlet vent and circulates in the plenum. Inside the concrete structure, the ventilation air absorbs decay heat, warming and expanding. The warmer, lighter air leaves the system through the outlet vent shown in Figure 1-2. To protect the concrete wall from the heat, a thin metallic heat shield is placed on the top and side internal walls of the concrete module. Internal components of the DSC shell, such as the spacer plates, tie rods, and fuel assemblies, are highlighted in Figure 1-3. The DSC is backfilled with pressurized helium to provide an inert atmosphere and enhance heat removal. Heat transfer from the fuel assemblies to the surrounding components and backfill helium takes place by conduction, convection, and radiation. The spacer plates shown in Figure 1-3 enhance the heat transfer and provide mechanical support to the fuel assemblies. The tie rods provide structural integrity and support to the system. The front and back covers of the DSC provide shielding. The DSC is placed on a pair of rails within the HSM module, as shown in Figures 1-2 and 1-3.

Figure 1-1. NUHOMS horizontal storage modules in Calvert Cliffs Nuclear Power Station ISFSI [from Suffield et al. 2012]

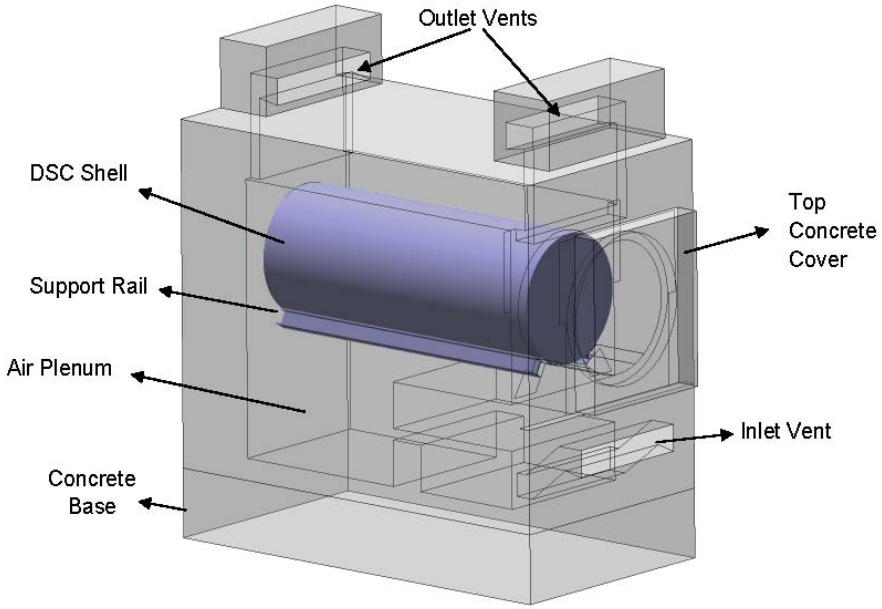

Figure 1-2. The concrete storage module and DSC shell with support rail for unit HSM–1

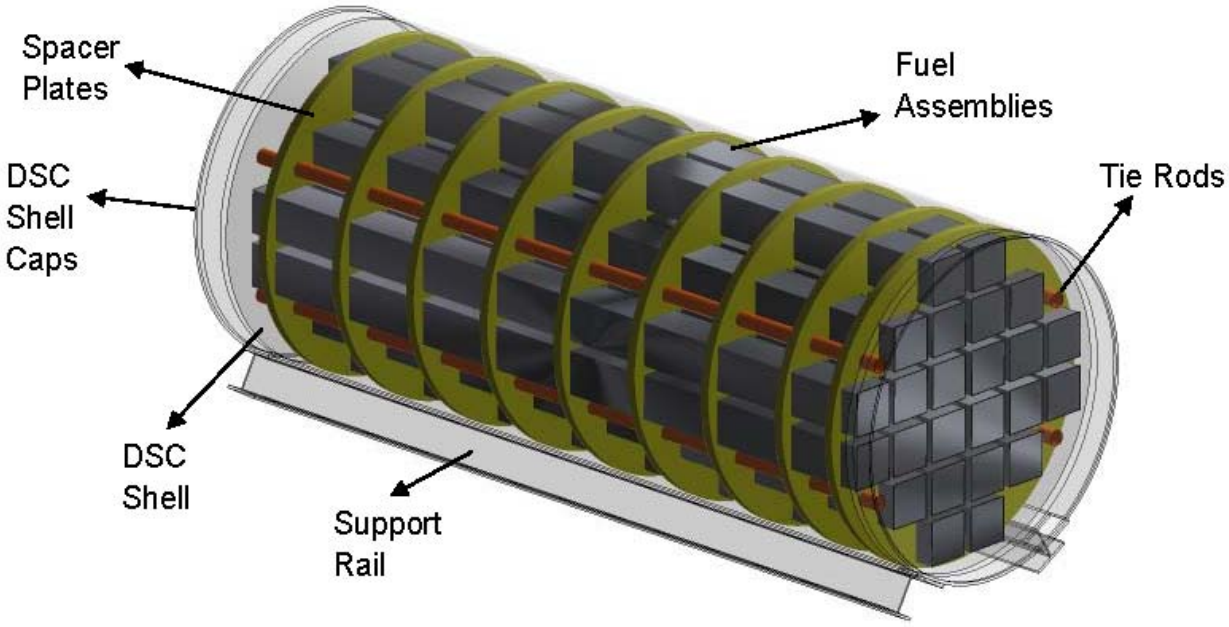

Figure 1-3. DSC shell and internal components: spacer plates, fuel assemblies, and tie rods for unit HSM–1

2. NUMERICAL MODELING METHODS

This chapter describes the mathematical and numerical models used to perform the simulations; the rationale for selecting these models; assumptions, methods, and rationale used for mesh generation; and the basis for the material properties used in the simulations. Most of the numerical models used in the present work, the turbulence models used in the sensitivity analysis, the basis for mesh generation, and the material properties used in the simulations are based on guidelines provided in NUREG–2152, "Computational Fluid Dynamics Best Practice Guidelines for Dry Cask Applications" [NRC 2012b].

2.1 ANSYS-FLUENT Fluid Flow Solver

The commercial computational fluid dynamics (CFD) package ANSYS-FLUENT® Version 14.5 [ANSYS 2012] was used for the simulations in the present study. ANSYS-FLUENT solves the governing integral equations for the conservation of mass and momentum, and (when appropriate) for energy and other scalars such as turbulence and chemical species concentrations. ANSYS-FLUENT uses a control-volume-based technique to convert a general scalar transport equation to an algebraic equation that is solved numerically. The following steps are used to solve the equations.

(i) Division of the domain into discrete control volumes using a computational grid.

(ii) Integration of the governing equations on the individual control volumes to construct algebraic equations for the discrete dependent variables ("unknowns"), such as velocities, pressure, temperature, and conserved scalars.

(iii) Linearization of the discretized equations and solution of the resultant linear equation system to yield updated values of the dependent variables.

2.2 Governing Equations

For numerical simulation of all types of flows, ANSYS-FLUENT solves conservation equations for mass and momentum. For flows involving heat transfer or compressibility, an additional equation for energy conservation is solved. For flows involving species mixing or reactions, a species conservation equation is solved or, if the non-premixed combustion model is used, conservation equations for the mixture fraction and its variance are solved. Additional transport equations are also solved when the flow is turbulent. Only the governing equations relevant to gas flow and heat transport in the dry storage canister (DSC) are presented in this section.

2.2.1 Continuity and Momentum Equations

The equation for conservation of mass, or the continuity equation, can be written as follows:

$$\frac{\partial \rho}{\partial t} + \nabla \bullet (\rho \vec{\upsilon}) = S_m \qquad \text{Equation (2-1)}$$

Equation (2-1) is the general form of the mass conservation equation and is valid for incompressible as well as compressible flows. Here ρ is the density and $\vec{\upsilon}$ is the velocity. The term $\rho\vec{\upsilon}$ defines the momentum. The source, S_m, is any user-defined source—for example, the mass added to the continuous phase from the dispersed second phase (due to vaporization of liquid droplets).

The conservation of momentum in an inertial (nonaccelerating) reference frame is described by

$$\frac{\partial}{\partial t}(\rho\vec{v})+\nabla\bullet(\rho\vec{v}\vec{v})=-\nabla p+\nabla\bullet(\bar{\bar{\tau}})+\rho\vec{g}+\vec{F} \qquad \text{Equation (2-2)}$$

where p is the static pressure, $\bar{\bar{\tau}}$ is the stress tensor, and $\rho\vec{g}$ and $\vec{F}$ are the gravitational and external body forces, respectively. $\vec{F}$ also contains other model-dependent source terms, such as porous media and user-defined sources.

The stress tensor $\bar{\bar{\tau}}$ is given by

$$\bar{\bar{\tau}}=\nu\left[\left(\nabla\vec{v}+\nabla\vec{v}^{T}\right)-\frac{2}{3}\nabla\bullet\vec{v}I\right] \qquad \text{Equation (2-3)}$$

where ν is the molecular viscosity, I is the unit tensor, and the second term on the right-hand side is the effect of volume dilation.

2.2.2 Energy Equation

The energy transport equation is given by

$$\frac{\partial(\rho E)}{\partial t}+\nabla\bullet\left[V(\rho E+p)\right]=\nabla\bullet\left[k_{eff}\nabla T-\sum_{j}h_{j}J_{j}+\tau_{eff}\bullet V\right]+S_{h} \qquad \text{Equation (2-4)}$$

where

$\frac{\partial(\rho E)}{\partial t}$	= Unsteady term
$\nabla\bullet\left[V(\rho E+p)\right]$	= Convection term
$k_{eff}\nabla T$	= Conduction term
$h_{j}J_{j}$	= Species diffusion term
$\tau_{eff}\bullet V$	= Viscous dissipation term
S_{h}	= Source term
V	= Velocity magnitude

In Equation (2-4), V is the velocity, k_{eff} is the effective thermal conductivity, h is the enthalpy, and J is the diffusion constant.

The energy, E, per unit mass is defined as

$$E=h-\frac{p}{\rho}+\frac{V^{2}}{2} \qquad \text{Equation (2-5)}$$

The numerics used in the present simulations, including the spatial scheme, the temporal scheme, and turbulence models, are explained in Section 2.5.

2.3 Solid Modeling and Mesh Generation for HSM–1 and HSM–15

The two major differences between horizontal storage modules HSM–1 and HSM–15 in the Calvert Cliffs Independent Spent Fuel Storage Installation (ISFSI) are the heat load and the location of the module within the storage array. The HSM–15 module includes spent fuel with the highest decay heat load values in the entire Calvert Cliffs ISFSI [Adkins et al. 2013; Suffield et al. 2012]. The DSC located within the HSM–1 module was the first canister loaded at the Calvert Cliffs ISFSI. According to Adkins et al. [2013], the decay heat load for the DSC in HSM–15 was 10.8 kW during the time of initial loading and the corresponding decay heat load for the DSC in HSM–1 was 5.8 kW (nearly 50 percent lower than HSM–15). HSM–15 is a central module in the 2 × 6 array of modules as shown in Figure 2-1, with only the top and front exposed to the atmosphere. The HSM–1 module is located on a corner of the 2 × 6 array and therefore has one side exposed to the atmosphere, in addition to the front and top. The exposed side wall of the HSM–1 module is much thicker than the interior walls between modules. External convection, insolation, and thermal radiation exchange with the environment were included in the model for the exposed side boundary of HSM–1.

The solid modeling and mesh generation for HSM–1 and HSM–15 include the mesh generated for the module internals, including the air inlet and air outlet vents; DSC support structures inside the concrete modules; and the heat shields (thin steel sheets) on the side walls and ceilings to protect the concrete walls from the thermal load of the DSC. The generated model and computational grid also include the DSC interior structure, comprising the spacer disks, tie

Figure 2-1. Aerial view of the Calvert Cliffs Nuclear Power Station ISFSI housing HSM–1 and HSM–15 modules [imagery© U.S. Geological Survey, Map Data© Google Inc. 2013]

rods, fuel assemblies, and the DSC top and bottom end caps. The stainless steel guide sleeves surrounding the fuel, along with the air gap between the sleeve and fuel assemblies, were also explicitly modeled. Figure 2-2 illustrates the geometry of the DSC and the three-dimensional (3-D) model of the DSC and its components. Figure 2-3 shows a 3-D schematic view of HSM–1. The construction of HSM–15 (not shown) is very similar to HSM–1, except that both side walls are the same thickness. Figure 2-4 shows a 3-D view of the solid model developed for DSC internals, such as the support rod, guide sleeve, and spacer disk, and the supporting structure, such as guide rails. Figure 2-5 shows the solid model developed for the fuel assemblies, tie rods, and the spacer plates.

2.3.1 Grid Generation

The same basic grid generation methodology was used for both HSM-1 and HSM-15. The computational domain consisted of the DSC geometry, the HSM module, the airflow path, the inlet and outlet vent, and a portion of the surrounding ambient environment. The baseline mesh consisted of 3.5 million cells over the entire computational domain. The computational grid was generated following guidance in NUREG–2152 [NRC 2012b]. To develop a controlled and systematic grid, the mesh density along the edges of the geometrical entities and the mesh refinement parameters such as stretching ratios were specified. Hexahedral grids were utilized to mesh the fluid and solid volumes in the domain. In most cases, the volume meshing was done by sweeping a two-dimensional (2-D) quadrilateral mesh along a specific direction. Figure 2-6 shows such a 2-D meshed surface that was used to generate the grid for the internal components within the DSC shell. The mesh generation method used in this study created a

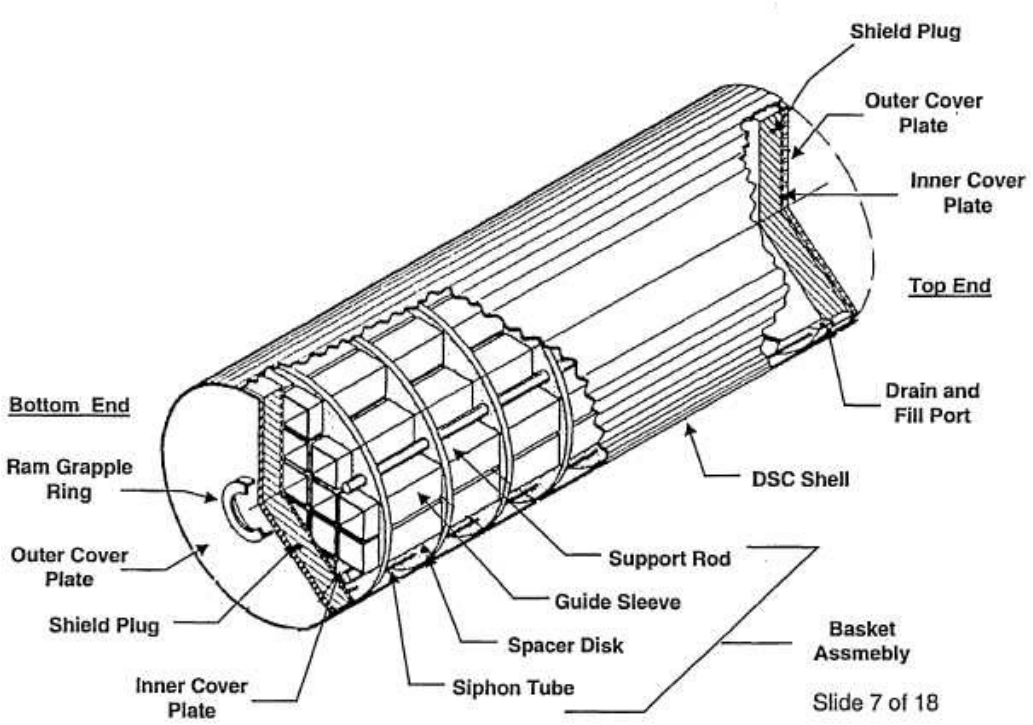

Figure 2-2. Schematics showing the geometry of the DSC [courtesy AREVA, PNNL]

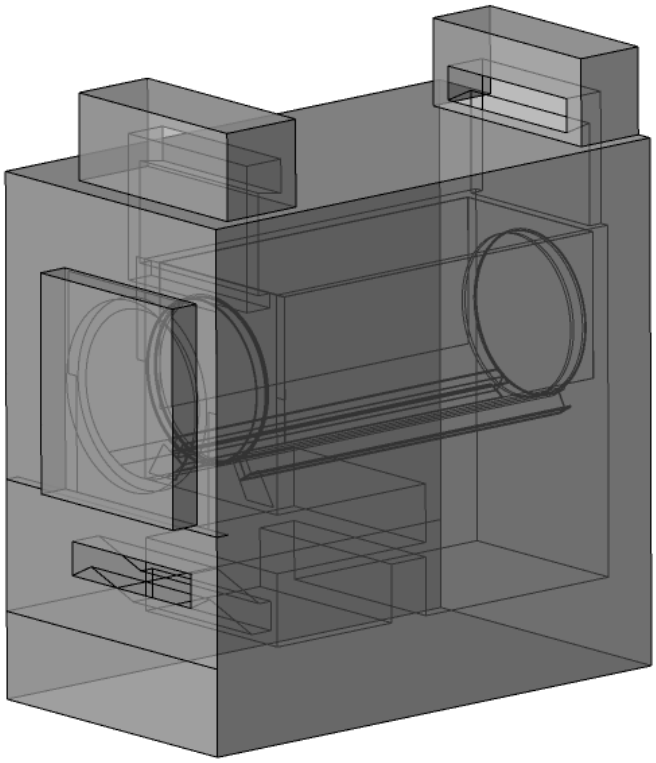

Figure 2-3. Three-dimensional schematic view of the HSM–1 module

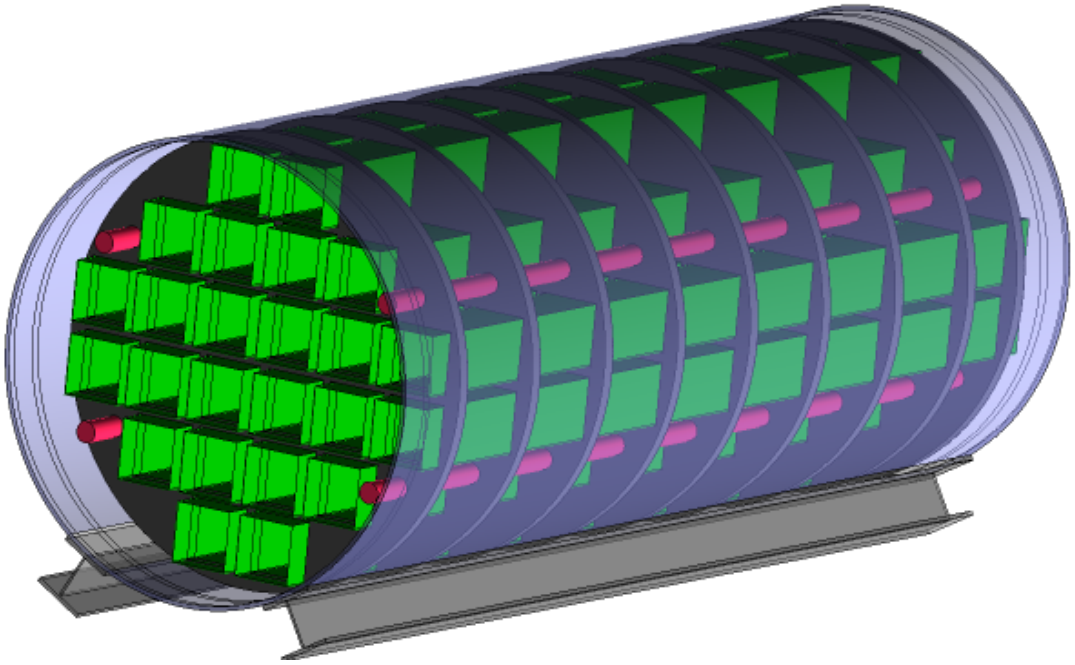

Figure 2-4. Three-dimensional view of the DSC internal showing the support rod, guide sleeve, spacer disk, and guide rails

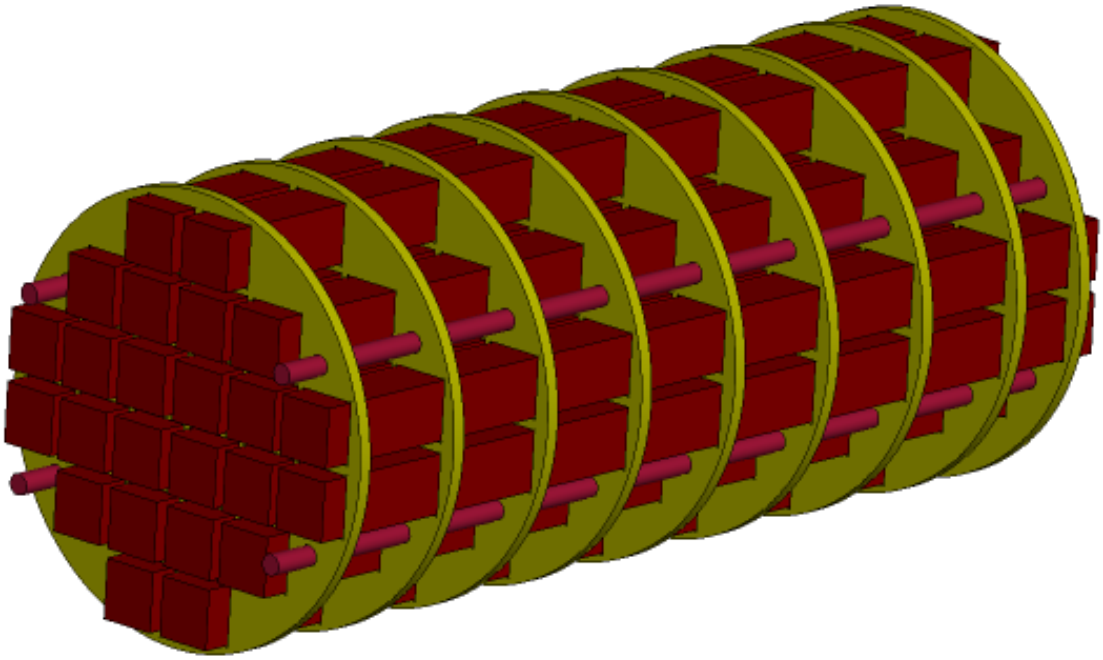

Figure 2-5. Three-dimensional schematic for the fuel assemblies, tie rods, and spacer plates within the DSC shell

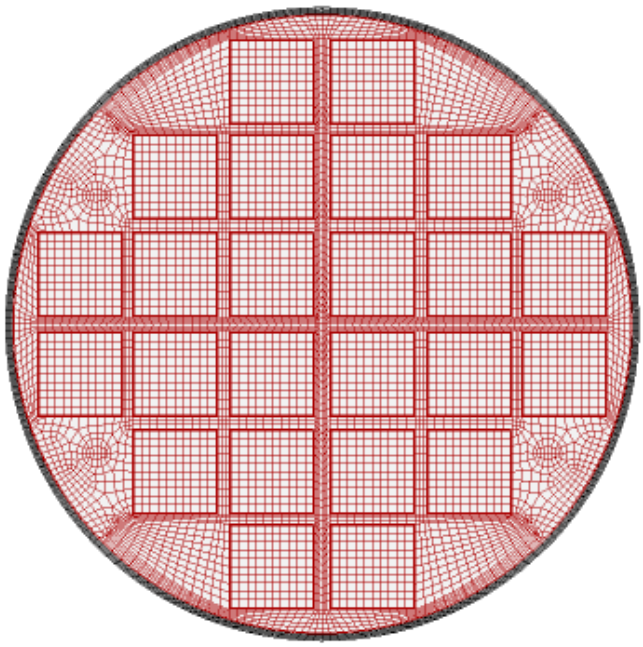

Figure 2-6. Two-dimensional cross-sectional view showing the computational grid for the fuel region

compact mesh that was amenable to systematic and controlled refinement, which was needed for the grid convergence index study described in Chapter 5.

The mesh spacing within the DSC region and in the region of the airflow path around the DSC was resolved more finely for accurately (i) simulating the airflow through the airflow path around the DSC and (ii) capturing the temperature and velocity gradients in the DSC region. A fine-resolution mesh was used in the near-wall region to facilitate the use of the low Reynolds number k-ε model. Ideally, a y^+ of 1 should be used to resolve velocity and temperature gradients up to the wall without the use of any wall functions. From the baseline simulations, it was found that the surface average wall y^+ for the DSC shell outer wall was approximately 2.97. Subsequently, a wall mesh refinement study was performed to understand the effect of near wall mesh size on the computational results (Section 3.3.1). It was found that near wall mesh refinement did not significantly affect the results and the baseline mesh was deemed appropriate for use in the study. In the regions where the velocity and temperature gradients are mild (such as in the concrete walls and in the airflow regions far from the DSC), a relatively coarse mesh was used for computational efficiency.

Figures 2-7 through 2-10 show the exterior and interior meshes for the HSM–1 module. The schematic for HSM–15 is the same. Figure 2-7 shows the 3-D exterior view of the computational grid for the HSM–1 module. Figure 2-8 shows a transverse cross-sectional plane of the domain and highlights the internal mesh used for the air volume within the concrete structure surrounding the DSC shell. Figure 2-9 shows a cross-sectional plane highlighting the general pattern of the internal mesh used in the axial plane. Figure 2-10 provides a closer look at the axial mesh generated within and around the DSC shell, fuel assemblies, spacer plates, and helium backfill region. The interior mesh, including the DSC within the HSM–1 module, is illustrated in Figures 2-11 and 2-12. Figure 2-11 shows the mesh generated on the DSC shell and support structure, while Figure 2-12 illustrates the mesh generated for the fuel assemblies, spacer plates, and tie rods.

The computational grid for HSM–15, with its thinner side wall, consisted of 3.2 million cells. The grid generation for the HSM–15 module followed the same principles that were used to generate the computational grid for the HSM–1 module and is not discussed in detail. As a part of the numerical uncertainty analysis, a detailed grid convergence index (GCI) study was performed (Chapter 5). The GCI study requires at least four mesh levels that are developed based on systematic refinement or coarsening of a baseline mesh. The existing mesh for HSM–1 and HSM–15 was used as the baseline mesh. Two levels of refinement and one level of coarsening were performed to create the four meshes necessary for the GCI study. The approach for mesh refinement and coarsening used in this study was adopted from the guidelines for best practice use of CFD for dry storage cask analysis provided in NUREG–2152 [NRC 2012b]. The total number of cells for each mesh level is shown in Table 2-1.

2.4 Boundary and Operating Conditions

The following subsections describe the boundary conditions used for HSM–1 and HSM–15 in the current simulations. Though mostly similar, some of the boundary conditions for HSM–1 and HSM–15 were applied differently because of the different locations of the modules. As mentioned in an earlier section, the HSM–15 module is located in the middle of the 2 × 6 array of modules and, hence, an adiabatic wall (no heat flow) boundary condition was applied for both side walls assuming similar decay heat of the casks at both sides. The HSM–1 module is located at one end (edge) of the 2 × 6 array of modules and therefore has one side exposed to the ambient condition and the other is assumed to be symmetric. In reality, some heat transfers

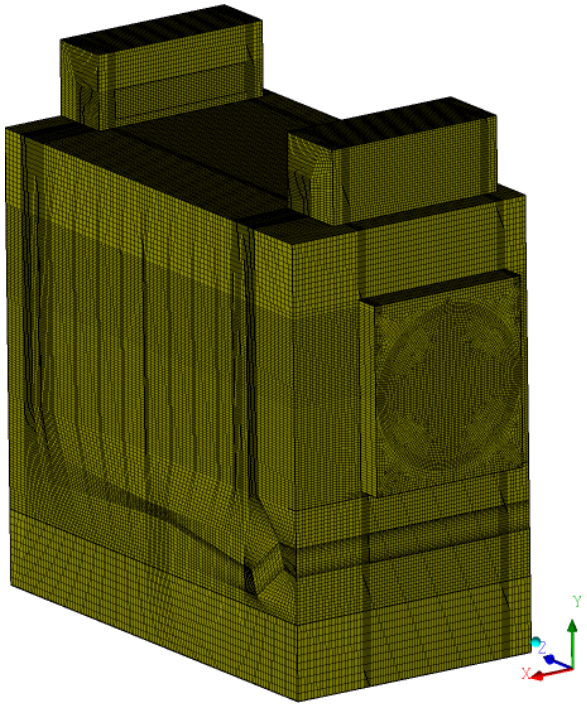

Figure 2-7. Three-dimensional view of the computational grid (exterior view) of the HSM–1 module

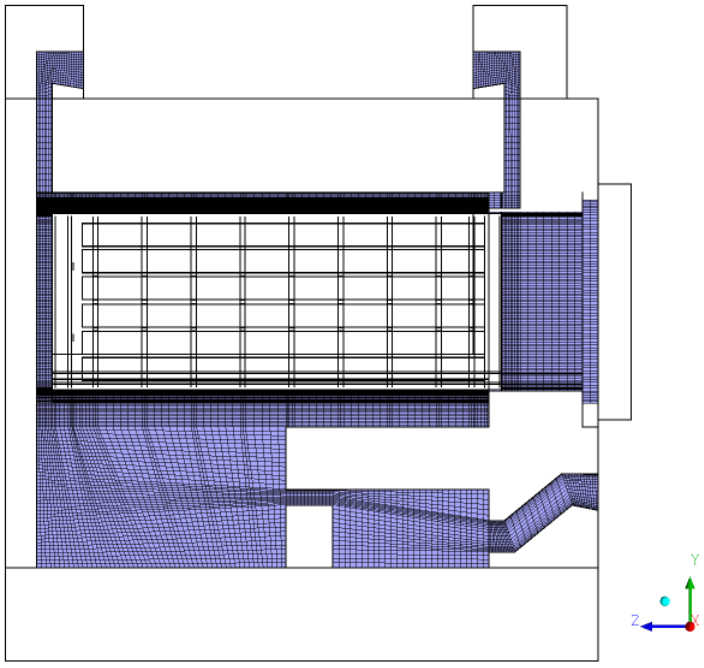

Figure 2-8. Transverse slice through center line showing computational grid of HSM–1, highlighting the airflow path

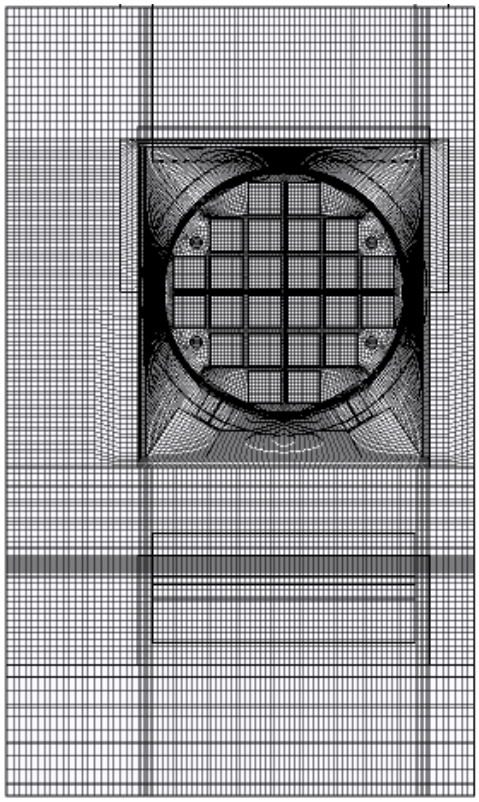

Figure 2-9. Planar slice through mid-section of the DSC showing computational mesh of HSM–1 module in transverse direction

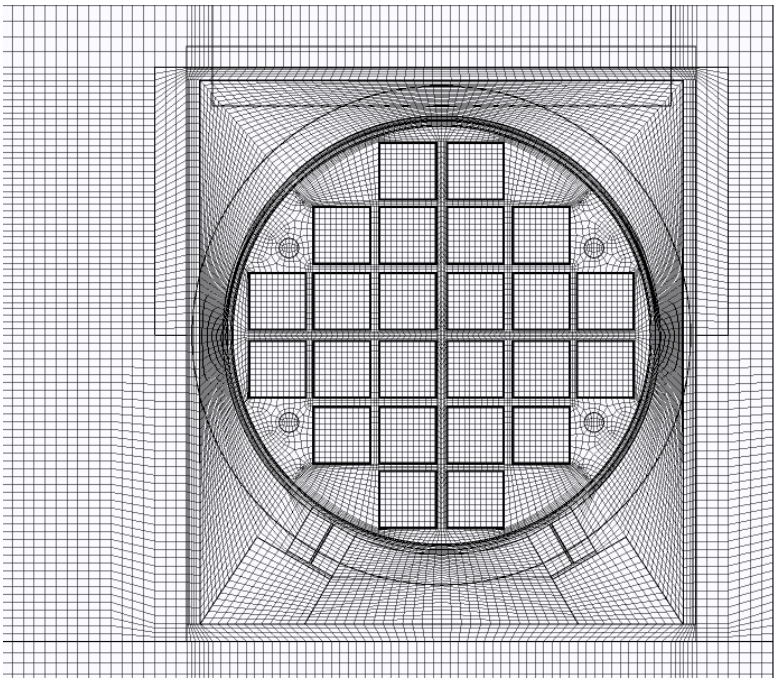

Figure 2-10. Enlarged view of the computational grid in the guide sleeve, support rod, and spacer plate region

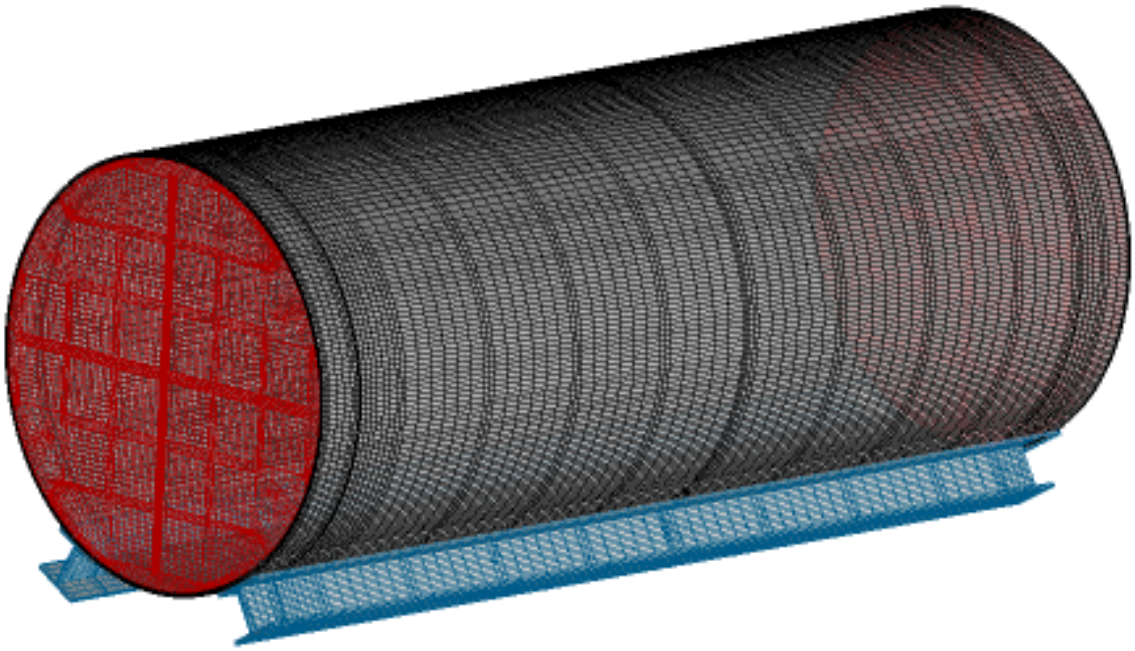

Figure 2-11. Three-dimensional view of the computational grid for the DSC internal and guide rails

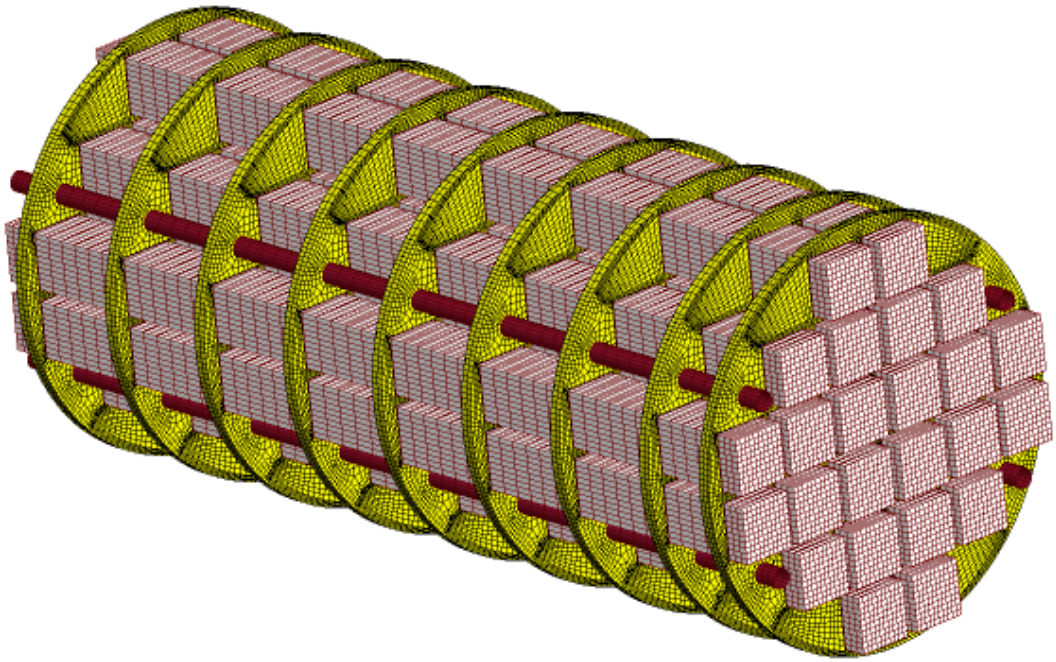

Figure 2-12. Three-dimensional view of the DSC internal showing the fuel region, support rod, guide sleeve, spacer disk, and guide rails

Table 2-1. Total number of cells for different grid levels used in the GCI study

	Total number of cells (in millions)	
Refinement/Coarsening	HSM–1	HSM–15
Refinement Level 2	24.51	22.63
Refinement Level 1	9.21	8.51
Baseline	3.52	3.27
Coarsening Level 1	1.22	1.13

from the central module to the adjacent corner modules through the side walls, depending upon the heat load of adjacent modules.

Once the model development and mesh generation for all the components were complete, fluid and solid regions were specified within the storage module and the canister. An air region was specified within the concrete structure of the storage module that surrounds the DSC. A helium-filled region was specified within the DSC. The solid region was composed of the concrete structure, DSC shell, support structure (e.g., rails), and DSC shell internals (e.g., spacer plates, fuel sleeves, tie rods, and end caps). The material for each of the solid regions was also specified. Suitable boundary conditions were specified at the exposed outer surface of the domain. An ambient environment was assumed to exist outside the HSM.

On the exposed boundary of the concrete (for both HSM–1 and HSM–15), a combination of external convection and thermal radiation exchange with the environment was allowed. The heat transfer factors for the convection heat transfer were calculated based on the correlation for free convection from the vertical flat plates and horizontal surfaces to the surrounding still air. The natural convection correlations used to calculate the heat transfer factors are presented in Appendix A. Radiation from the side surfaces and top walls was also included and an emissivity of 0.9 for the concrete external surface was specified. An ambient temperature was specified at 301 K [82 °F] for all the simulations, representing equilibration to late June air temperatures at the site to represent conditions during the temperature measurements. On the bottom surface, which is the interface between the module and underlying soil, conduction through the base to a concrete pad and underlying soil was specified by defining appropriate thermal resistance. This thermal resistance is determined as an equivalent conduction through 1.8 m [6 ft] of soil to a temperature of 288 K [58.73 °F], with a typical soil conductivity of 0.52 W/m-K [8.34 BTU/ft-sec-°F] [Zigh and Solis 2008]. The temperature at depth within the soil is the mean annual air temperature at the site. Solar heat loads were applied at the outer exposed surfaces of the modules. The regulations for packaging and transportation of radioactive material (10 CFR Part 71, Section 71.71) specify, for a 12-hour period, a solar load of 800 g-cal/cm^2 [2,949.35 BTU/ft^2] for horizontal surfaces, 200 g-cal/cm^2 [737.337 BTU/ft^2] for flat non-horizontal surfaces, and 400 g-cal/cm^2 [1,474.675 BTU/ft^2] for curved surfaces. Because there are no curved external surfaces, the solar load specification used the values for horizontal and vertical flat surfaces. A heat generation rate that produces a heat flux equivalent to the required solar loading was specified on the external surfaces in the ANSYS-FLUENT model.

The storage modules at Calvert Cliffs have a single air inlet on the bottom of the front face and two exit vents at the top of the module. These vents are protected by a number of screens, which provide resistance to airflow and therefore cause a pressure drop. To appropriately account for the pressure drop, the inlet and outlets are modeled as vents in ANSYS-FLUENT, where the pressure loss factor is specified as a piecewise linear function of normal velocity. The terms of this equation were derived based on the pressure drop equation for incompressible flows through screens [Perry and Green 1997]. This method is described in Appendix A.

The back surface of the storage module for both HSM–1 and HSM–15 was assumed to be symmetric to account for the presence of another storage module with similar decay heat. Both the side surfaces of HSM–15 and one of the side surfaces of HSM–1 were also specified to have a symmetric boundary. Though specification of symmetry implicitly assumes that the thermal loads of the adjoining modules are the same, this assumption enables estimating the temperature field with reasonable computing resources and without including all storage modules in the computational domain.

The ambient pressure was specified as 101,325 N/m^2 [2,116 lbf/ft^2]. The operating ambient air density was specified as 1.173 kg/m^3 [0.072 lbm/ft^3], which was calculated using the ideal gas law based on the ambient pressure and temperature. For the internal surfaces that are not exposed to the ambient environment, coupled boundary conditions were used at the solid–fluid interface. Based on the material of the solid body, emissivity values were specified for the surface. The emissivity values associated with specific materials used in the model are listed in Table B–7 of Appendix B. These values were obtained from engineering handbooks and textbooks, and were not directly measured or tested for the actual cask configuration.

2.5 Numerics, Radiation Heat Transfer, and Turbulence Models for the Simulations

The pressure-based, steady-state solver of ANSYS-FLUENT was used in simulating the flow field of the HSM–1 and HSM–15 modules. The velocity coupling was done using the SIMPLE algorithm. For spatial discretization, second-order upwind spatial differencing was used for all variables except the pressure equation (continuity equation), where a body force weighting factor was used. Gradients were calculated with a Green-Gauss node-based method. Suitable under-relaxation factors were used for all the variables to optimize numerical stability and achieve faster convergence.

Thermal radiation between surfaces within the HSM module elements and DSC components is vital to the overall heat transfer process. In the present study, the discrete ordinate model (DO) was used for thermal radiation modeling. In this approach, the radiative transfer equation (RTE) for an absorbing, emitting, and scattering medium is solved for a finite number of discrete solid angles. The discrete ordinate model transforms the RTE into a transport equation for the radiation intensity in the spatial coordinates. The number of equations the DO model solves is controlled by the angular discretization. To solve the HSM–1 and HSM–15 problems, four angular discretizations were used in each direction of the spherical coordinate system [theta (θ) and phi (φ)]. The number of energy iterations per radiation iteration was limited to 10 for optimal convergence. The modeled storage systems do not have any semi-transparent media; hence explicit DO-energy coupling was not needed to enhance convergence.

The Reynolds number for the airflow within the concrete module was estimated using the average air velocity and density from initial HSM–1 runs and a characteristic length representing the flow path. The calculated Reynolds number was approximately 8,399, which is significantly higher than the threshold of 4,000 for producing turbulent internal flows. As the physics of the problem involves natural convection, the Rayleigh number of the flow was determined based on the DSC shell diameter, average temperature of the air and DSC shell, and average density and fluid properties. The calculated Rayleigh number was 8.45×10^9, which is higher than the critical value for natural convection on vertical plates (10^9). Because the flow within the storage module is different from simple vertical flat plate flows, the added complexity is expected to trigger an early transition to turbulence, thus the flow will be in the transitional turbulent regime for HSM–1. HSM–15 contains hotter fuels, so the flow velocity for HSM–15 will be higher and

result in a larger Reynolds number. The higher HSM–15 temperature will yield a larger Rayleigh number, so the airflow within HSM–15 will also be in the transitional or turbulent regime. An appropriate turbulence model is needed to accurately predict local velocities and temperatures in the air stream. The low Reynolds number k-ε model with full buoyancy effects was used for the majority of the simulations performed in this study. In addition, a sensitivity study was performed to assess the effect of turbulence models on calculated quantities (Section 3.3.2). The standard k-ε model with scalable wall function and buoyancy effects, SST k-ω model with low Reynolds number corrections, and SST k-ω model with buoyancy effects were used in this sensitivity study. The Reynolds number for the helium flow within the DSC shell was in the laminar region; thus, the helium flow was treated as a laminar zone in the simulations.

2.6 Fuel Assembly Model

HSM–1 and HSM–15 both contain 24 pressurized water reactor (PWR) fuel assemblies, each carrying an arrangement of CE 14 × 14 fuel rods. Each fuel assembly inside the DSC shell was modeled as a porous medium using guidelines provided in NUREG–2152 [NRC 2012b] and as described in Appendix C. The fuel assembly model development consisted of three steps: (i) a porous media model calculation to determine flow resistances, (ii) an effective thermal conductivity calculation, and (iii) a fuel assembly decay heat loading specification. Each of these steps is detailed in separate appendices.

2.6.1 Porous Media Calculation

The porous media model was used in the HSM–1 and HSM–15 models to represent flow inside the fuel assemblies, which are each treated as a continuous porous medium with predetermined resistance specified in the axial and radial flow directions. These parameters are used as surrogates for the pressure loss caused by the presence of fuel rods. In essence, the porous media model adds a momentum sink in the governing momentum equations. This approximation significantly reduces the computational mesh requirements needed to explicitly model each fuel rod in the assembly.

A frictional resistance and an inertial resistance factor must be specified for the porous media model in ANSYS-FLUENT. 3-D CFD simulations of an isolated fuel assembly were performed to determine these resistance factors. The 3-D simulations model the complete length of a fuel assembly containing CE 14 × 14 fuel rods, represented as solid cylindrical objects. Simulations were performed for a number of inlet velocities encompassing the range of velocities expected. From each simulation, the pressure drop across the fuel assembly was determined, then frictional and inertial resistances were calculated from the set of calculated pressure drops and input velocities. The porous media model calculations are described in Appendix C.

2.6.2 Effective Thermal Conductivity Calculation

The fuel assemblies were modeled as porous regions, assumed to have anisotropic thermal conductivity. Based on the fuel arrangement within an assembly, the effective radial and axial thermal conductivities were determined in a separate, stand-alone calculation.

The temperature-dependent effective thermal conductivity was determined in the axial direction using a simple weighted-area-average method. The fuel (UO_2) material, helium fill gas, and Zircaloy cladding of the fuel rod were considered in the averaging process. In the radial direction, the effective thermal conductivity method [Bahney and Lotz 1996] was used to obtain the conductivity of the fuel as a function of temperature. To calculate the

temperature-dependent thermal conductivity, a separate 2-D finite volume model, using ANSYS-FLUENT 14.5, was built to represent a planar section of the fuel assembly. This 2-D model considered each fuel rod along with fuel cladding and the backfill helium gas. Every fuel rod in the assembly was assumed to have the same heat load. A heat load value representative of the conditions expected in the present study was used in the analysis. A series of simulations was performed to determine the temperature-dependent effective radial thermal conductivity of the fuel assembly. The calculated axial and radial effective thermal conductivity values were used in ANSYS-FLUENT as temperature-dependent conductivity functions using an orthotropic distribution. The effective thermal conductivity calculations are described in Appendix D.

2.6.3 Fuel Assembly Loading

The decay heat load was defined for each of the 24 active fuel regions of the CE 14 × 14 assemblies within the DSC for both HSM–1 and HSM–15 based on the decay heat load data from the Calvert Cliffs ISFSI provided by NRC. The fuel structure and fuel identification location for HSM–1 and HSM–15 are shown in Figures 2-13 and 2-14, respectively. The decay heat load was applied as a uniform volumetric heat generation rate over the active fuel length within each fuel region. This volumetric heat generation rate was modified to include the axial variation by multiplying the volumetric heat generation rate by an axial peaking factor. The axial variation of heat load was implemented as a user-defined function in the ANSYS-FLUENT solver. The decay heat calculation and fuel assembly loading for the HSM–1 and HSM–15 modules are detailed in Appendix E.

2.7 Material Properties Used in the Simulations

In general, temperature-dependent material properties were used in the simulations. Concrete, stainless steel, carbon steel, and lead are the solid materials used in the model, and air and helium are the fluid materials. The material properties are detailed in Tables B–1 through B–7 of Appendix B.

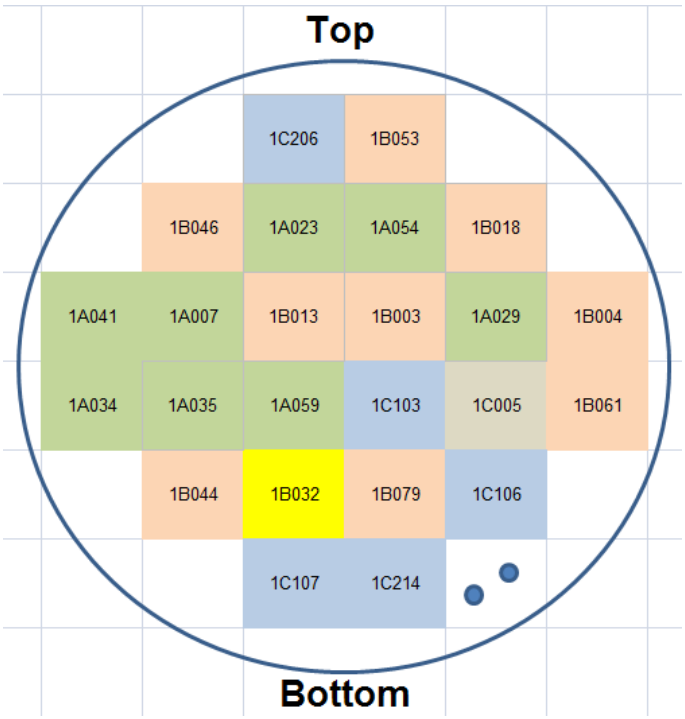

Figure 2-13. Fuel assembly loading identification structure for HSM–1 module

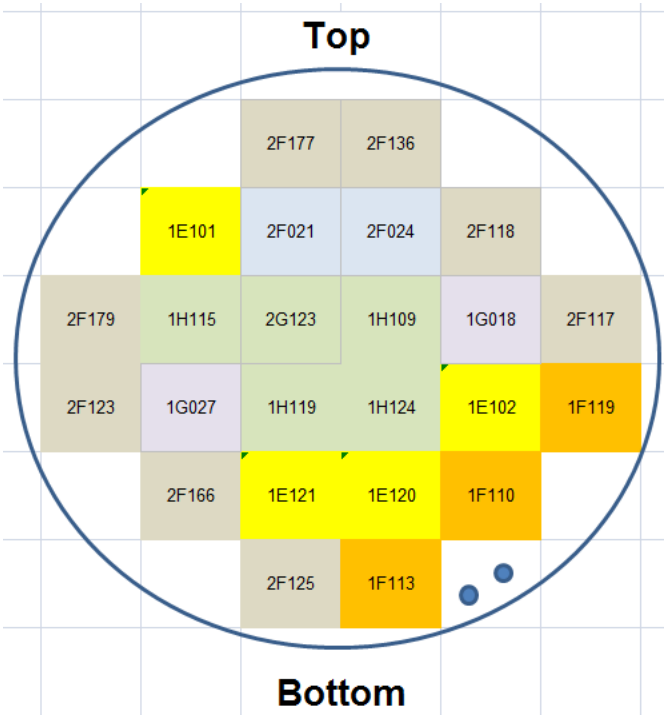

Figure 2-14. Fuel assembly loading identification Structure for HSM–15 module

3. BENCHMARK MODELING AND SENSITIVITY ANALYSES

This chapter discusses the results of the benchmark simulations for horizontal storage modules HSM–1 and HSM–15. The computed temperature data are compared with field measurements. This chapter also presents results from a series of sensitivity studies on the HSM–1 simulation, performed to assess the effects of turbulence models, porous media resistance, and insolation. An additional simulation was performed using an extended computational domain to include the surrounding atmosphere to verify the convective heat transfer coefficient used at the outer walls in the baseline study.

3.1 Description of Field Temperature Measurement

The field temperature measurements for the HSM–1 and HSM–15 modules in the Calvert Cliffs Nuclear Power Station Independent Spent Fuel Storage Installation (ISFSI) were taken on June 27 and 28, 2012. The direct temperature measurements were conducted under the Used Fuel Disposition Campaign of the U.S. Department of Energy (DOE) [Suffield et al. 2012]. Visual inspections and surface sampling were also performed. Due to safety constraints and physical constraints related to accessing the different regions of the DSC, reliable temperature measurements were obtained only on the exposed face of the canister base and a short distance along the canister side [Suffield et al. 2012]. The front door of each module was opened to obtain the temperature measurements. The HSM–15 module was open for about 20 minutes, with a single temperature measurement obtained on the exposed base of the DSC [Suffield et al. 2012]. HSM–1 was open for approximately 160 minutes, with 16 temperature measurements obtained on the base and sides of the canister [Suffield et al. 2012]. The temperatures were measured with an Omega “all-in-one” hand-held thermometer, Model 450-AET with Type E Chromega®-constantan thermocouple, or a Model 450-APT platinum resistance temperature detector (RTD) thermocouple [Suffield et al. 2012]. The observation points and comparisons between the measured and simulated data are presented in the following sections.

3.2 Results of Baseline Simulations

Computed results from the baseline steady-state simulations of HSM–1 and HSM–15 are presented in this section. The decay heat loads for each fuel assembly used in the baseline steady-state simulations are listed in Appendix E. The ambient temperature considered in the simulations is 27.9 °C [301 K, 82.19 °F], corresponding to the mean air temperature for the day when measurements were taken.

The spatial distributions of simulation results are presented using three-dimensional (3-D) plots and cross sections. Figure 3-1 displays the axial and transverse cross sections used to display temperature and velocity patterns for both the HSM–1 and HSM–15 simulations. Both of these cross sections pass through the centroid of the DSC.

3.2.1 HSM–1

The total decay heat load for the dry storage canister (DSC) in the HSM–1 module was calculated at approximately 4.1 kW [13,990 BTU/hr]. This decay heat was used along with the volume of each fuel assembly region to determine the volumetric heat generation rate input in the simulations. This volumetric heat generation rate was applied over the active fuel length within each fuel region and was modified to include the axial variation through an axial peaking

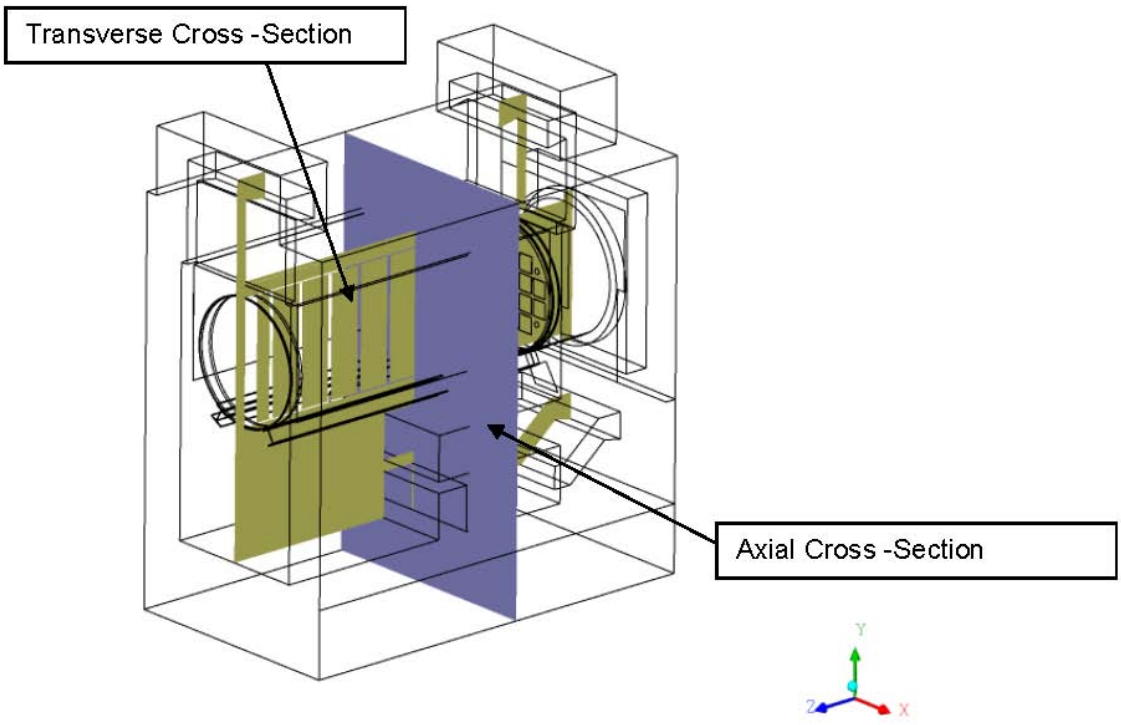

Figure 3-1. Axial and transverse cross-sectional planes used to illustrate temperature and velocity distributions

factor. The peaking factor is constant at a maximum value over the central 60 percent of the axial length, and drops approximately linearly to the end of the canister to roughly half of the peak value. The peaking factor calculations are described in Appendix E.

3.2.1.1 Temperature and Velocity Patterns

Figures 3-2 and 3-3 present simulated temperatures on the DSC shell surface and on internal metal surfaces within the DSC for the HSM–1 module. Figure 3-2 shows that temperatures peak at approximately 75 K [135 °F] above the ambient temperature in the upper middle section of the DSC, and drop to approximately 15 K [27 °F] and 20 K [36 °F] above ambient at the back and front ends, respectively. The back end of the DSC is cooler than the front end because of enhanced ventilation flow and the location of the active fuel zone. The high-temperature region is located at the upper middle section of the DSC because (i) decay heat loads are largest in the central portions of the individual fuel assemblies and (ii) temperature-driven natural convection flow of the helium coolant inside the DSC transports heat up from the core of the DSC. The helium coolant forms two natural convection cells, with warming helium rising in the center of the DSC and cooling helium falling along the DSC side walls as heat is transferred through the DSC wall to the ventilation air. It can also be observed that the support rails, at only 10 K [18 °F] above ambient, are relatively cool compared to the other parts of the DSC shell, losing heat by conduction through contact with the concrete side walls.

Figure 3-3 illustrates the temperature distributions for the fuel region, spacer plates, and support rods. Temperature is highest at the upper part of the fuel region and peaks at 85K [153 °F] above ambient, which is approximately 10K [18 °F] higher than the peak DSC shell temperature.

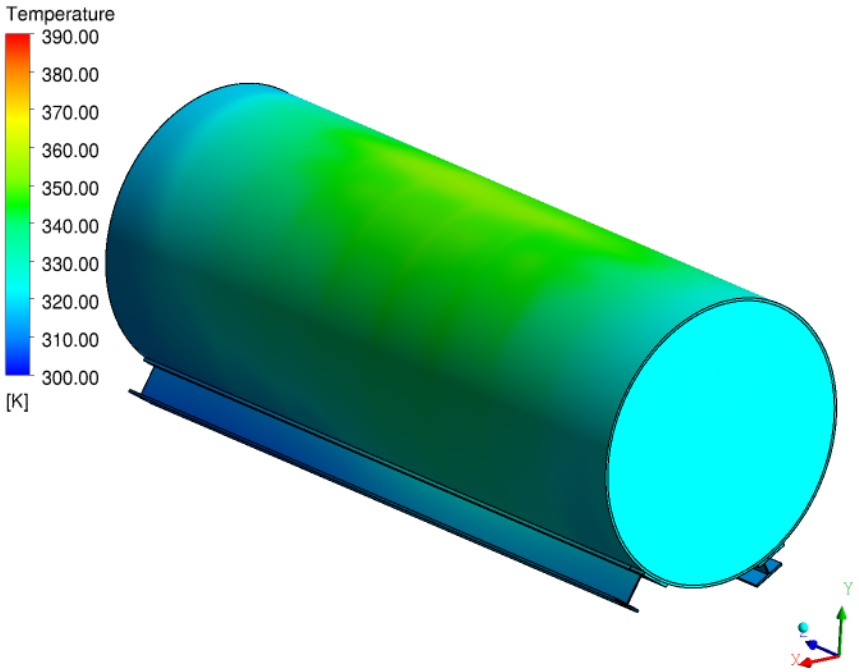

Figure 3-2. Contours of DSC shell surface temperature for the HSM–1 baseline case

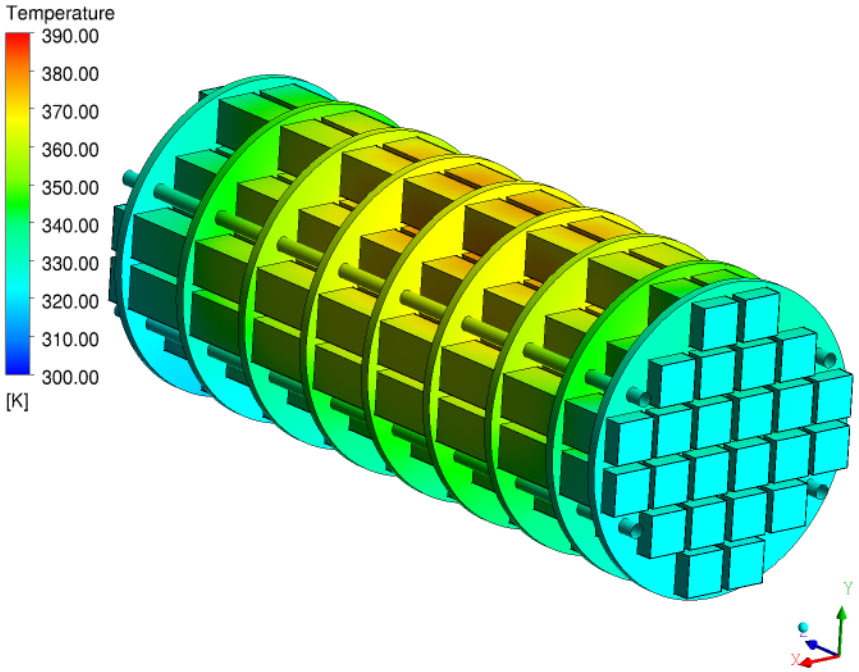

Figure 3-3. Temperature distributions for the fuel region, spacer plates, and support rods for HSM–1 baseline case

This can again be attributed to buoyancy driven natural convection transporting warmer helium upwards, resulting in a high temperature region at the upper section of the fuel region. The high temperature region is also located near the middle of the fuel region in the axial direction, with cooler temperatures at the front and back of the assemblies. As observed in connection with Figure 3-2, this pattern results from the peaking factor and heat load distribution along the axial direction.

Figures 3-4 through 3-7 illustrate the spatial distribution of temperature in (i) fluids in the transverse cross section, (ii) solids in the transverse cross section, (iii) fluids in the axial cross section, and (iv) solids in the axial cross section, respectively. The warm temperatures in the upper middle DSC are clearly evident in all four figures. Figure 3-4 shows that the ventilation air is approximately 10 K [18 °F] warmer in the poorly connected volume between the HSM–1 door and the front end of the DSC than in the well-connected volume at the back end of the DSC, and shows that the ventilation air increases in temperature by 45 K [81 °F] from the inlet to the outlet. A comparison of Figures 3-6 and 3-7 illustrates the sharp drop in temperature {30 K [54 °F] to 50 K [90 °F]} across the DSC shell.

Figures 3-8 through 3-10 show the predicted velocity field of the HSM–1 module, using airflow streamlines in Figure 3-8 and air and helium velocity vectors on the transverse and axial cross sections in Figures 3-9 and 3-10.

The airflow streamlines in Figure 3-8 illustrate the ventilation process for the dry storage system. Cool air enters the system at the inlet and gains heat from the DSC. The air expands as it warms, with the less-dense air inducing flow out the top vents and causing air to flow within the cavities around the DSC. The relatively large velocities in the cavity along the DSC walls and above the top of the DSC are examples of buoyancy-induced convection due to the strong heating from the DSC. The colored streamlines and velocity magnitude plots indicate that the fastest air movement is near the inlet and outlet, and in the narrow cavity below the DSC. Low velocities occur in the open region below the DSC, where the inlet jet creates a large recirculation zone. The poorly connected volume at the front end of the DSC has very low velocities and no streamlines enter the volume; the well-connected volume at the back end of the DSC also has relatively low velocities, but some streamlines do enter this zone. In general, the air flow within the concrete module and around the DSC shell is asymmetric as a result of design features such as the locations of the air inlet vents, outlet paths, and internal obstructions. This flow asymmetry contributes to the uneven cooling of the DSC shell and internal components in the axial direction, as illustrated previously in Figures 3-2 and 3-3.

Figures 3-9 and 3-10 show that the movement of helium within the DSC is highly localized into channels between the fuel assemblies and is roughly proportional to the heat loading. Within these channels, helium velocities are comparable to the ventilation air velocities outside the DSC shell, but helium is essentially stagnant within each fuel assembly. Warming helium moves upward within the channels and cooling helium drops along the DSC side walls.

3.2.1.2 Temperature Line Probes

The simulated temperature distribution on the DSC shell, heat shield, and fuel region can be examined by extracting values along predefined axial probe lines from the ANSYS-FLUENT results. Probe lines were selected to demonstrate relatively high and low temperatures on the DSC shell, on the heat shield, and within particular fuel assemblies. Figure 3-11 shows top and right probe lines for the DSC shell and heat shield, representing high and low temperatures, respectively. Figure 3-12 shows fuel assembly probe lines for relatively hot (fuel assembly 1)

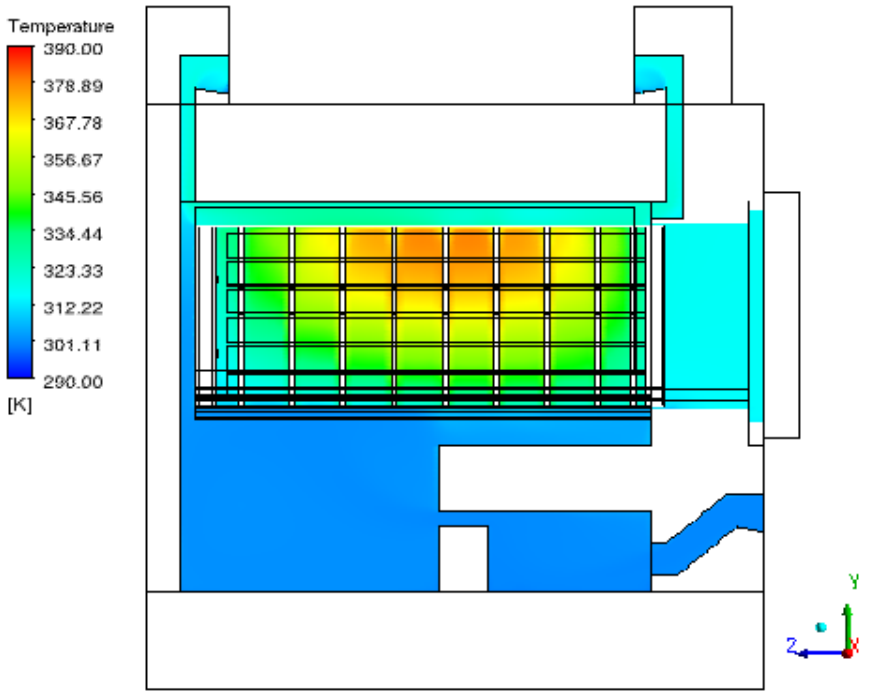

Figure 3-4. Air and helium temperature distributions along the transverse cross section for the HSM–1 baseline case

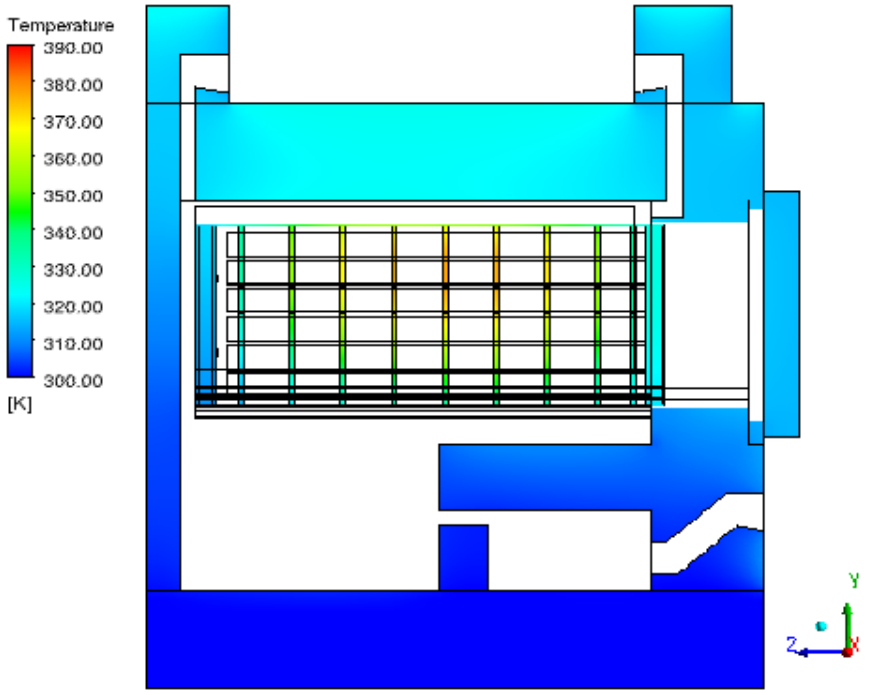

Figure 3-5. Temperature distribution for the solid region at transverse cross section for HSM–1 baseline case

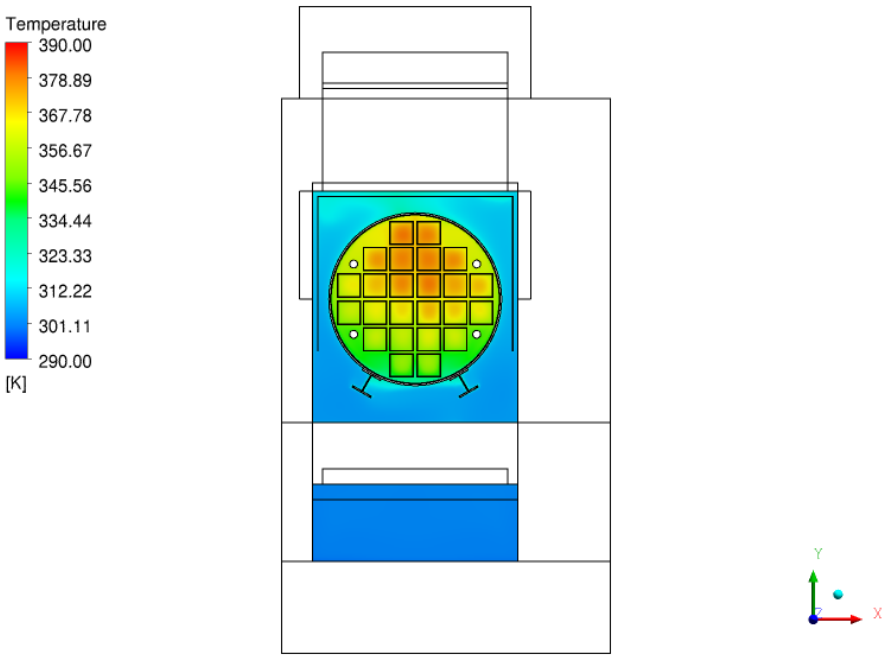

Figure 3-6. Temperature distribution for the fluid region along the axial cross-sectional plane for the HSM–1 baseline case

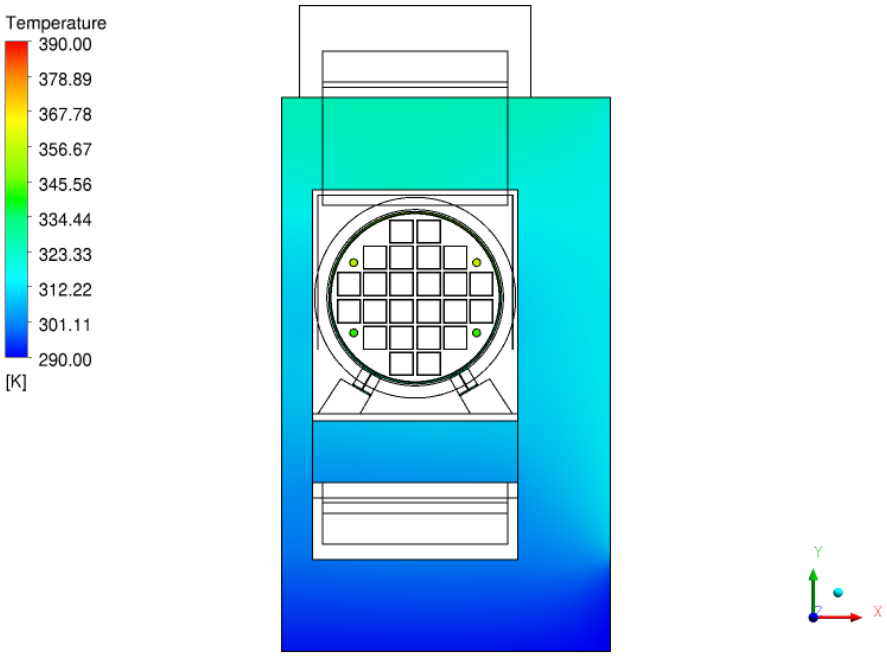

Figure 3-7. Temperature distribution for the solid region along the axial cross-sectional plane for the HSM–1 baseline case

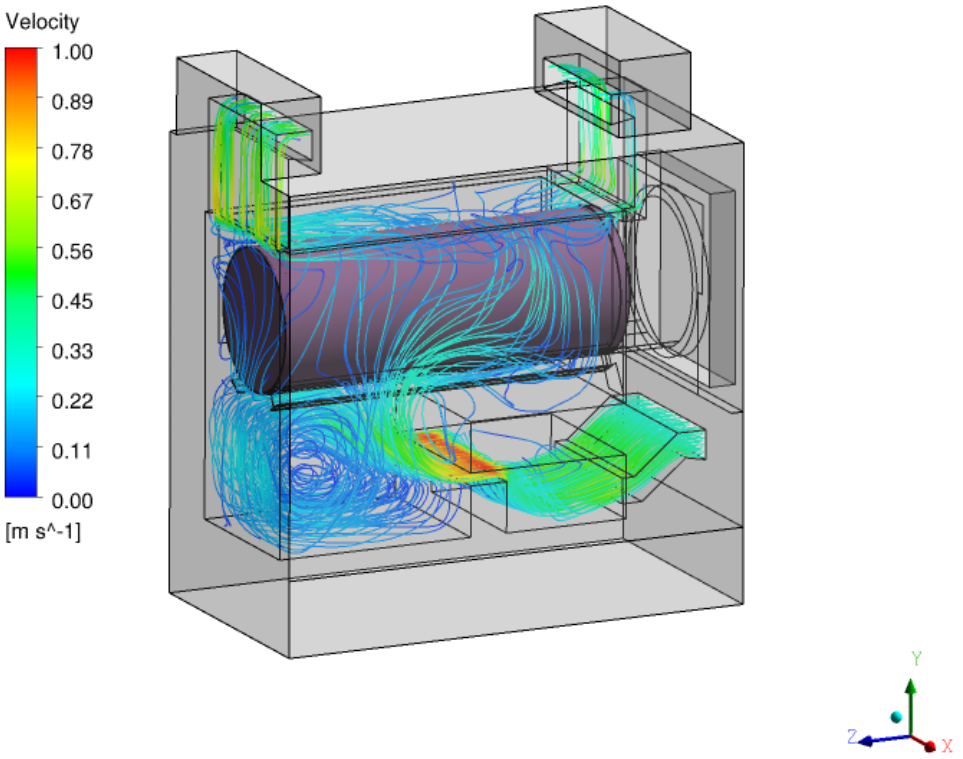

Figure 3-8. Streamlines showing the airflow path and airflow circulation within the HSM–1 module

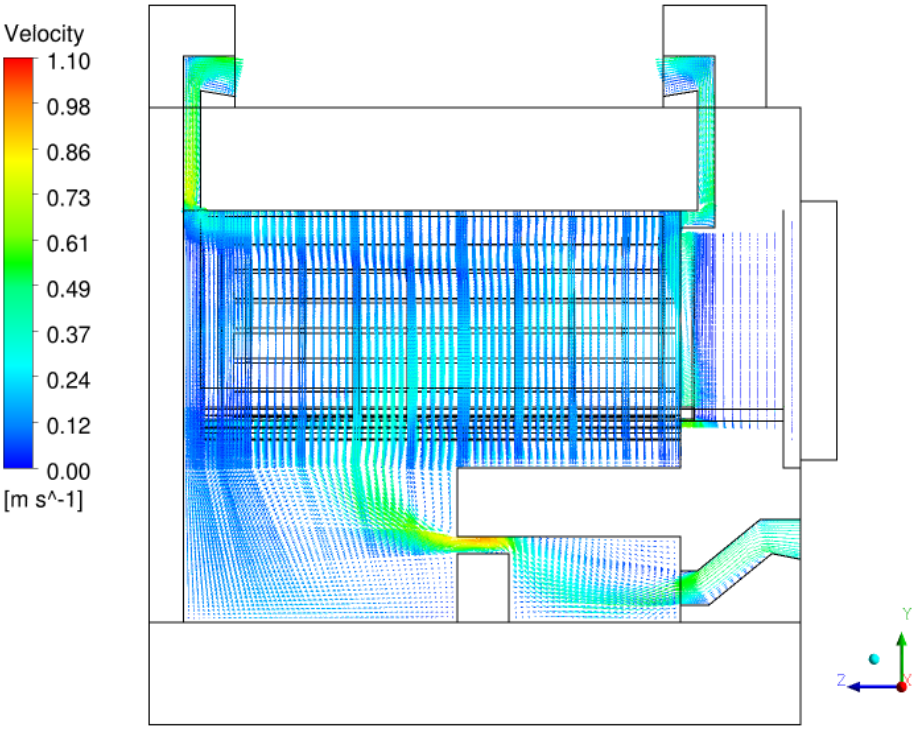

Figure 3-9. Velocity vectors at the mid-plane in the transverse cross section for HSM–1 module

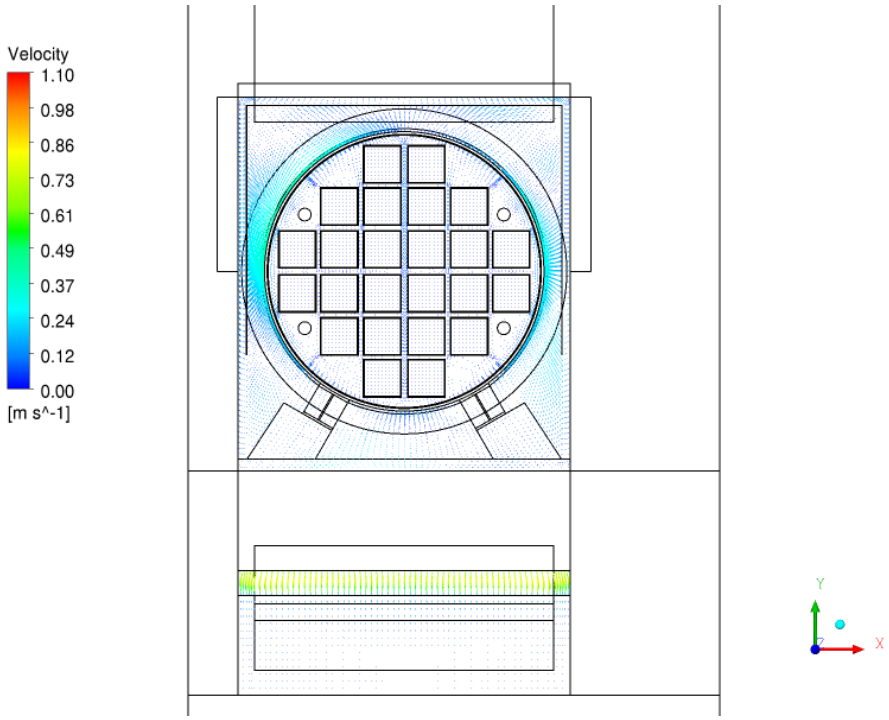

Figure 3-10. Velocity vectors at the axial cross section for HSM–1 module

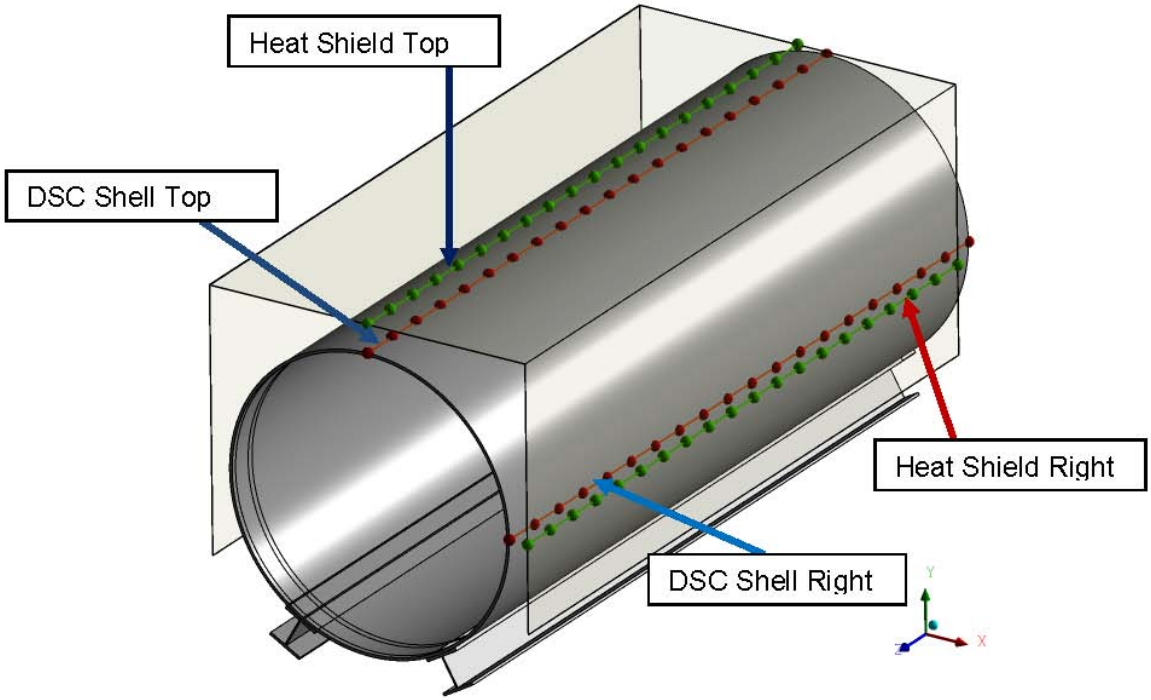

Figure 3-11. Line probe locations for extracting temperature distribution along the axial direction: locations shown on the DSC shell and on the heat shield

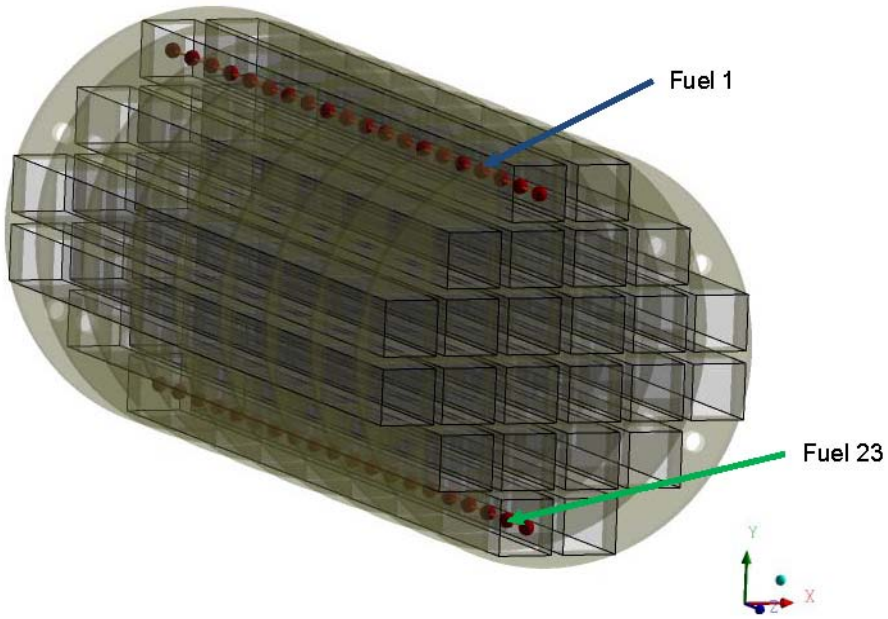

Figure 3-12. Line probe locations for extracting temperature distribution along the axial direction in the fuel region: locations shown for fuel assemblies 1 and 23

and cool (fuel assembly 23) assemblies. The corresponding temperature profiles are shown in Figures 3-13 through 3-15.

Comparing Figures 3-13 and 3-14, it can be seen that the temperature difference between the top and right probe lines is essentially the same for the DSC shell and the heat shield. The right side of the DSC shell shows a fluctuating pattern with spikes (Figure 3-13), which can be attributed to the presence of spacer plates. In general, the spacer plates have a higher temperature than the surrounding helium. Hence, the proximity of spacer plates to the DSC shell wall enhances radiative heat transfer, resulting in localized high temperature zones. The relatively hot helium at the top of the DSC shell provides a more uniform temperature field next to the shell, damping the peaks. In both the DSC shell and the heat shield, the temperature distribution is skewed towards the module door as a result of asymmetric ventilation air patterns and the location of the active fuel zone (see Figure 3-8).

Figure 3-15 contrasts temperatures along fuel assemblies 1 and 23. The assemblies are both hotter and more symmetric than the shell and heat shield. Assembly 1 is much hotter than assembly 23 because of natural convection within the DSC. The peak temperatures in these assemblies are not located at the center, but are biased towards the front of the module. This effect, more prominent in assembly 23, is primarily due to the distribution of heat load along the axial direction of the fuel assemblies (illustrated by the peaking factor distribution in Appendix E). However, this may also be related to uneven cooling due to asymmetric flow around the DSC shell, as highlighted in Figure 3-8.

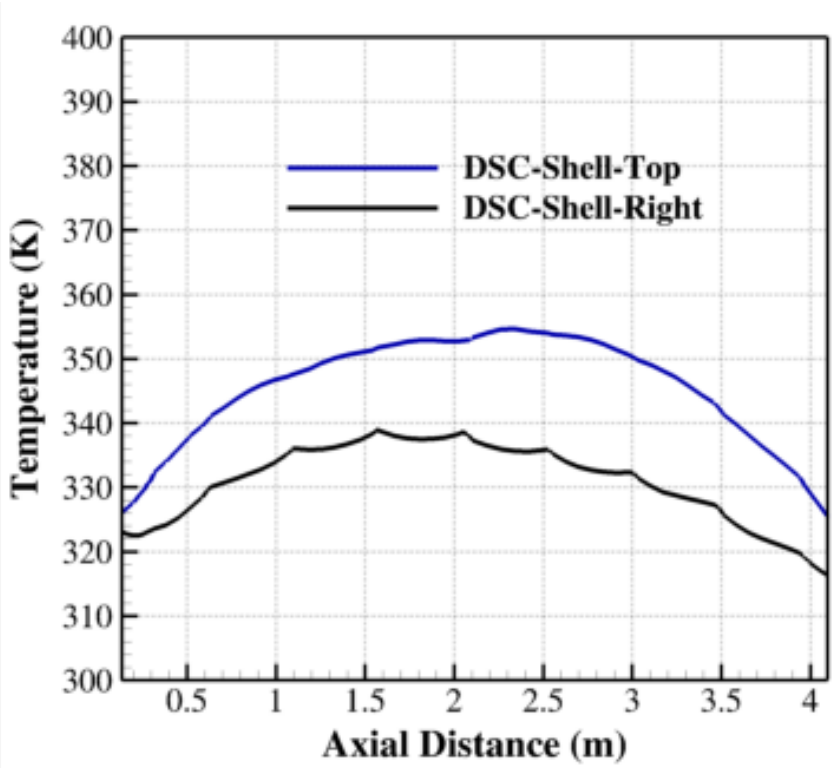

Figure 3-13. Computed temperature distribution along the axial distance for top of DSC shell and right of DSC shell

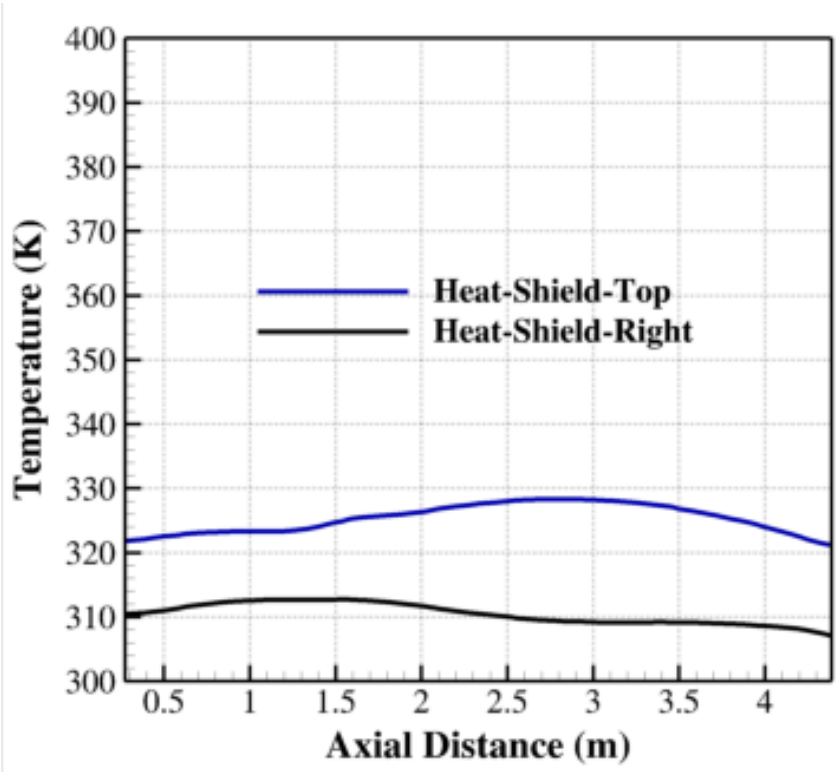

Figure 3-14. Computed temperature distributions along the axial distance for top of heat shield and right of heat shield

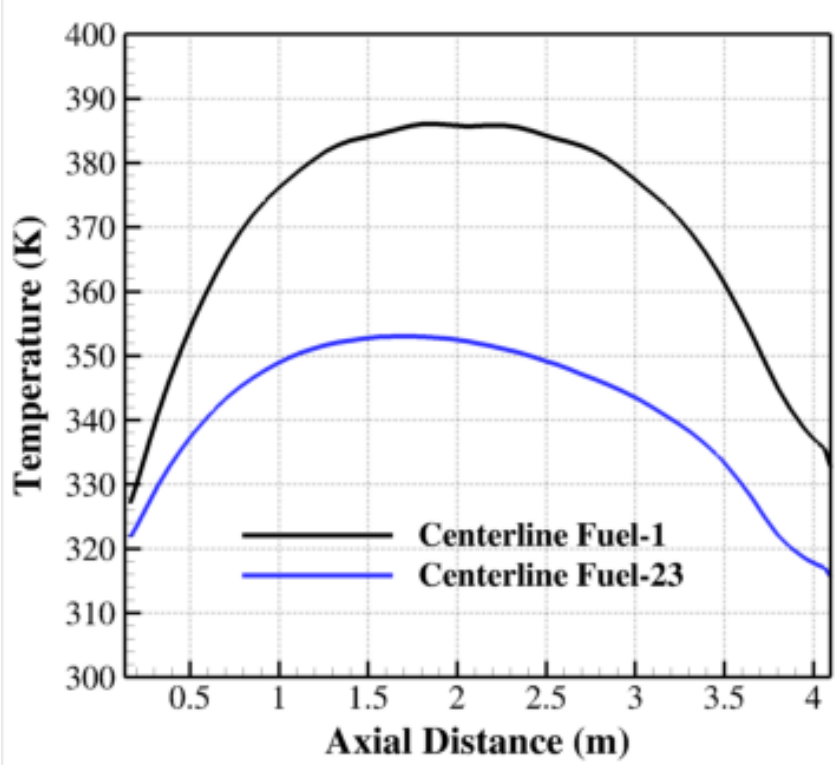

Figure 3-15. Computed temperature distributions along the axial distance for fuel region: distribution shown for fuel assemblies 1 and 23 for HSM–1 baseline case

3.2.1.3 Comparison With Measured Data

Table 3-1 presents a comparison of the computed temperature with measured temperatures at specified locations. The measurement locations were constrained by the length of the thermocouple probe, which reached a maximum of 1.016 m [3.33 ft] along the sides of the DSC.

Measurements were obtained at the top, sides, and support rail locations (Figures 3-16 and 3-17). The temperature measurements were taken at three axial locations:

- 1.02 m [3.34 ft] from the exposed surface of the DSC surface,
- 0.51 m [1.67 ft] with the probe inserted half the length, and
- 0 m [0.0 ft].

From the description of the measurement procedure [Suffield et al 2012], it is apparent that the measured temperatures have significant uncertainty. Before the measurements, the front door of HSM-1 was open for approximately 160 minutes. This allowed hot air from within the module to escape and lower the temperature within the system. Therefore, the measured temperatures would be lower than the temperatures of a normally operated closed module. Temperature measurements were taken by touching a handheld device to the canister surface [Suffield et al 2012]. It is not clear if the probe was in contact with the surface for a period long enough to establish thermal equilibrium between the proble and surface. Without thermal equilibrium, the probe would record a temperature lower than the actual value. A review of measured data from Table 3-1 shows a relatively flat temperature distribution along the axial direction, especially at the DSC shell top wall. Given the magnitude of the heat load and the axial distribution of the peaking factor, a flat axial temperature distribution is unlikely. This may indicate that, due to the

Table 3-1. Comparison of measured and predicted temperatures for the baseline case simulations for HSM–1 module

Location 1 m [3.28 ft]	Measured value (K) [°F = 1.8 K-460]	Baseline case simulation value (K) [with insolation, low Re standard k-ε model with buoyancy] (K) [°F = 1.8 K-460]
Under Grapple ring	317.44	324.18
0-m-side-right	315.22	323.04
0-m-side-top	319.11	325.18
0-m-side-left	313	322.68
0-m-rail-right	313.55	319.05
0-m-rail-left	314.11	319.05
0.51-m-side-right	315.77	325.74
0.51-m-side-top	320.22	336.94
0.51-m-side-left	313.55	324.94
0.51-m-rail-right	314.11	318.81
0.51-m-rail-left	314.66	318.7
1.02-m-side-right	315.22	334.35
1.02-m-side-top	321.33	346.89
1.02-m-side-left	315.22	333.39
1.02-m-rail-right	314.11	322.04
1.02-m-rail-left	315.22	321.97

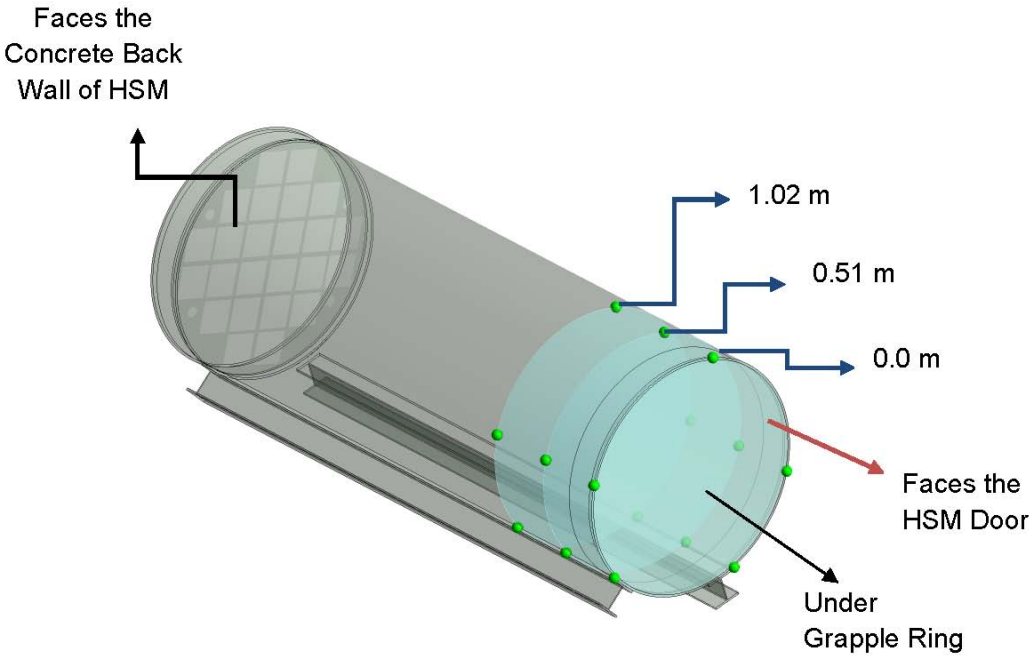

Figure 3-16. Thermocouple locations shown at 0.0-, 0.51- and 1.02-m axial distance

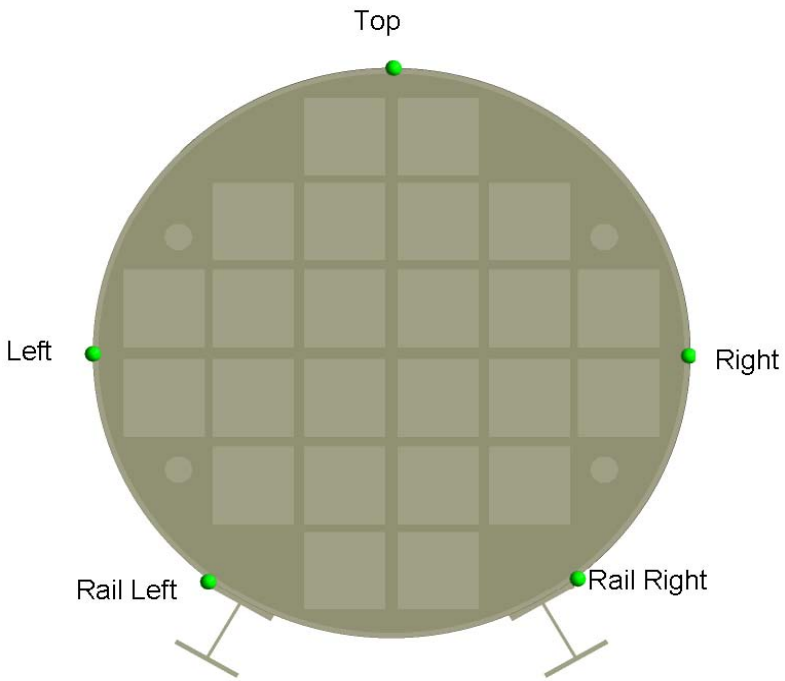

Figure 3-17. Thermocouple locations shown at the top, right side, left side, rail right, and rail left

difficulty of inserting the proble in the narrow space between the DSC shell and module concrete wall, complete contact between the probe and DSC shell wall was not established and the probe reported the air temperature rather than the solid surface temperature. Finally, the temperature measurement was performed only once. Without repeated measurements, the uncertainty in the measurement cannot be evaluated.

At each axial location, temperature measurements were taken at five different locations: at two horizontal sides and the top of the DSC shell, and at the two sides of the support rails. These locations are highlighted in Figure 3-17. In addition, a measurement was taken under the grapple ring, which is located on the cover of the DSC (Figure 3-16).

Table 3-1 illustrates that the simulated temperatures, in general, overpredict the measured temperatures. The minimum deviation between the computed and measured data is approximately 4 K [7.3 °F] and occurs at the middle section on the rail. The maximum deviation is around 25.5 K [46.0 °F] and occurs at the top interior section of the DSC shell. The difference between measured and observed temperatures increases with distance from the opening. As discussed previously in this section, there is significant uncertainty associated with the measured temperatures and whether they are appropriate for comparison with the current predicted results. The simulated temperatures are in reasonable agreement with the measured temperatures near the cap of the DSC {i.e., at an axial location of 0.0 m [0.0 ft]}, but the temperatures measured at 0.51 and 1.02 m [1.67 and 3.34 ft] at the surface are significantly lower than the simulated temperatures. In addition, as discussed previously in this section, the thermocouple probe may not have made good contact with the DSC surface on the side of the DSC, in which case the measured temperatures at 0.51 m [1.67 ft] and 1.02 m [3.34 ft] may actually be air temperatures and not DSC surface temperatures. Suffield et al. [2012] expressed similar observations and views.

3.2.2 HSM–15

Computed results from the baseline simulation of the HSM–15 module are presented in this section. The baseline simulations were performed using an ambient temperature of 28 °C [301 K, 82.19 °F] and decay heat load values calculated for June 2012. The total heat load for HSM–15 in June 2012 was 7.6 kW [25,933 BTU/hr], compared to 4.1 kW [13,990 BTU/hr] for HSM–1. The decay heat load distribution for each fuel assembly region in the HSM–15 module is provided in Appendix E, using the same axial peaking factor distribution as was used for HSM–1. This decay heat was divided by the volume of each fuel assembly region and used as the volumetric heat generation rate input in the simulations. The HSM–15 module is located at the middle of the 2 × 6 array of modules, thus only the top and front are exposed to the atmosphere. In contrast, the HSM–1 module is located at one corner of the 2 × 6 array of modules and therefore has a side exposed to the atmosphere. Because the general patterns of temperature and flow are similar to those reported for HSM–1, only the differences between the HSM–15 and HSM–1 simulations will be discussed.

3.2.2.1 Temperature Field

Figures 3-18 through 3-26 present the simulated temperature field of the HSM–15 module. Figures 3-18 and 3-19 show the temperature distribution along the DSC shell surface and on internal surfaces, respectively. The highest simulated temperature for the HSM–15 DSC shell {391.46 K [245.2 °F]} is significantly higher than the highest temperature simulated on the DSC shell for the HSM–1 module {355.27 K [179.82 °F]}. This observation is consistent with the larger decay heat load of the fuel stored in HSM-15 compared to HSM-1. Considering the configurations of HSM–15 and HSM–1 in the module array, the higher temperatures simulated for HSM–15 could also reflect the lower exposure of outer surfaces to atmosphere compared to HSM–1. However, this effect is expected to be minor compared to the difference in decay heat load, which is the principal cause of the higher temperatures realized for HSM–15. The general temperature distribution patterns for the HSM–15 and HSM–1 DSC shells and internal surfaces are similar.

Figures 3-20 through 3-23 show temperature distributions for HSM–15 along transverse (Figures 3-20 and 3-21) and axial (Figure 3-22 and Figure 3-23) cross sections. The highest simulated helium temperature for the HSM–15 DSC internal fuel region in Figure 3-20 {454.48 K [359 °F]} is significantly higher than the highest simulated temperature for the HSM–1 DSC internal fuel region {390 K [243 °F]}. This is due to the higher decay heat load for HSM–15. The spacer plates have the highest temperatures shown in Figure 3-21, as was the case for HSM–1 (see Figure 3-5), but the maximum temperature of the spacer plates for HSM–15 is higher than HSM–1. The concrete at the base remains at a relatively lower temperature (almost the same as the ambient temperature) and the pattern is the same for both HSM–1 and HSM–15, indicating that the difference in decay heat load did not significantly affect the base temperatures. Figures 3-22 and 3-23 demonstrate a sharp temperature difference across the DSC shell at the top of the shell.

Axial simulated temperature profiles for the HSM–15 module are presented in Figures 3-24 through 3-26. While HSM–15 temperatures are generally higher than HSM–1 temperatures, the patterns of temperature distribution are similar. Therefore, the HSM–1 observations of Section 3.2.1.2 apply also to HSM–15.

.

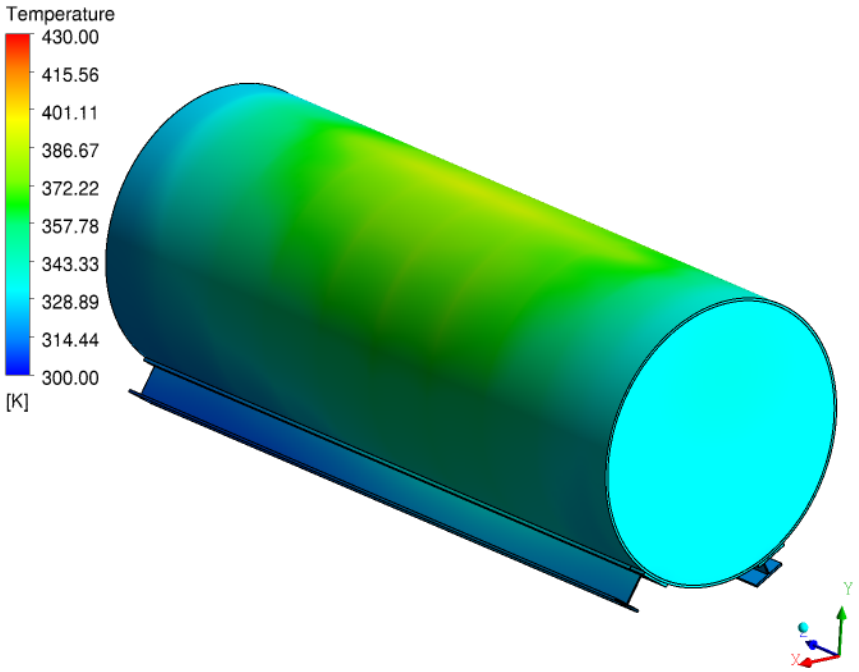

Figure 3-18. Contours of DSC shell surface temperature for HSM–15 baseline case

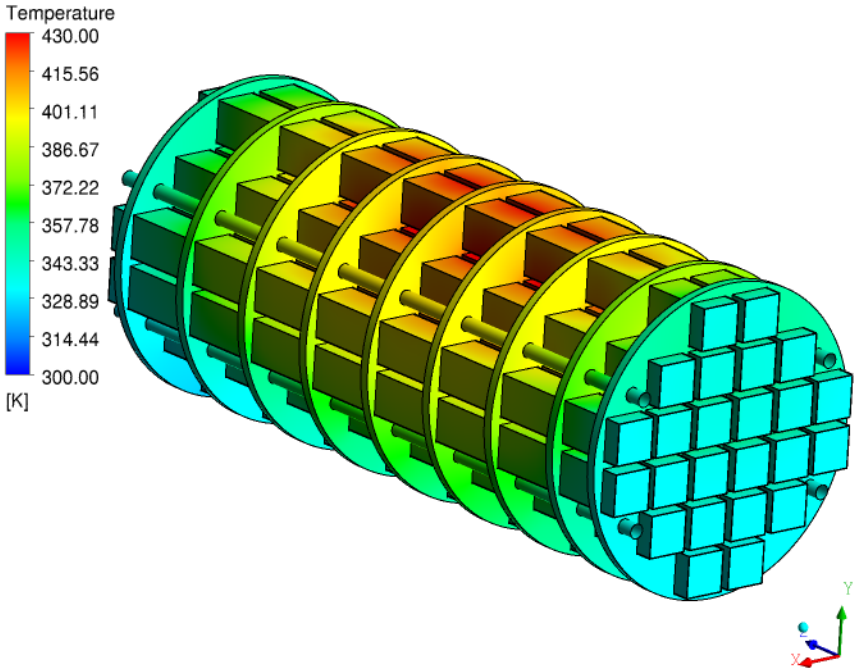

Figure 3-19. Temperature distributions for the fuel assembly, spacer plates, and support rod for HSM–15 baseline case

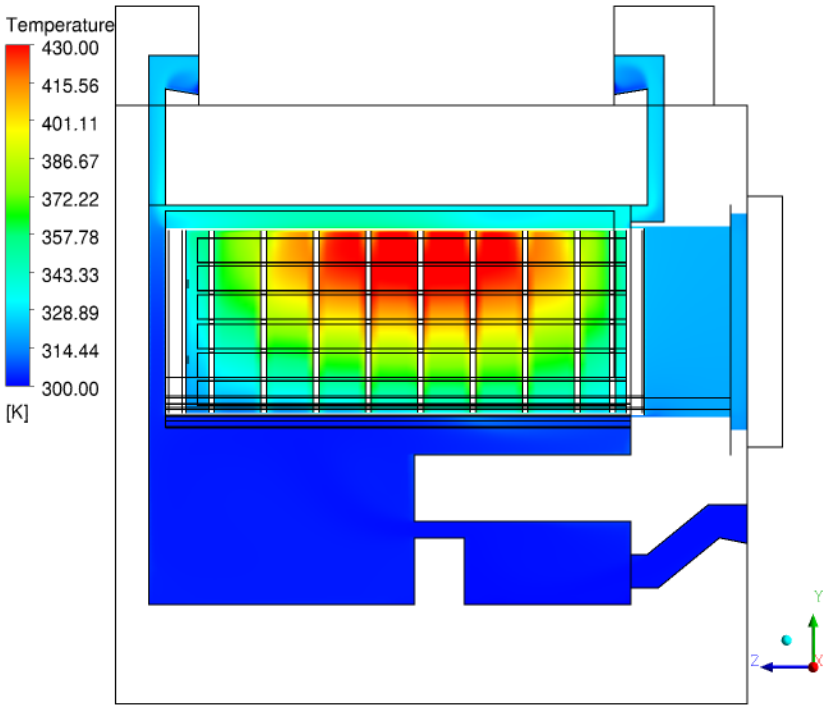

Figure 3-20. Air and helium temperature distributions along transverse cross section for HSM–15 baseline case

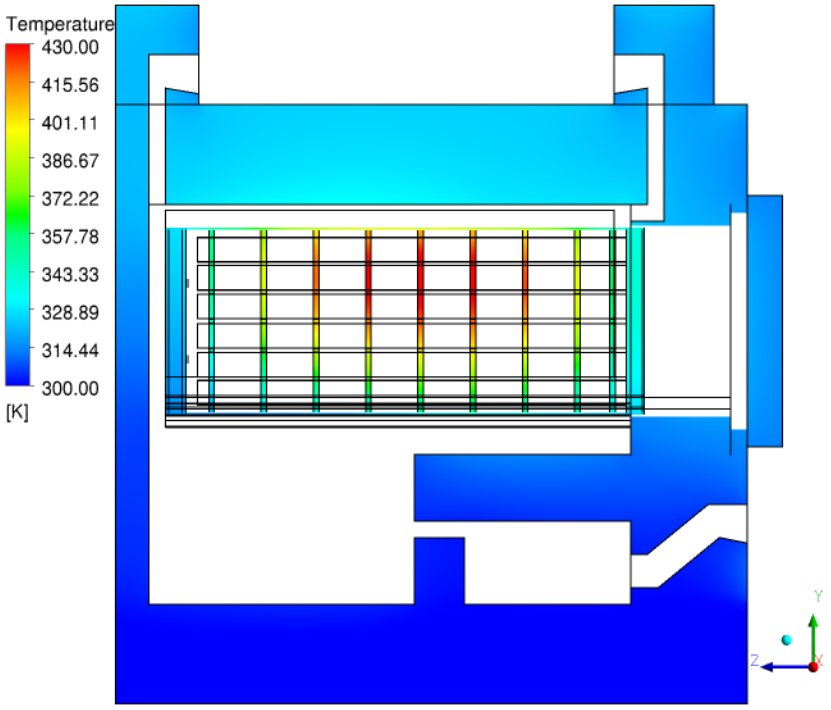

Figure 3-21. Solid region (concrete, spacer plates) temperature distributions at the transverse cross section for HSM–15 baseline case

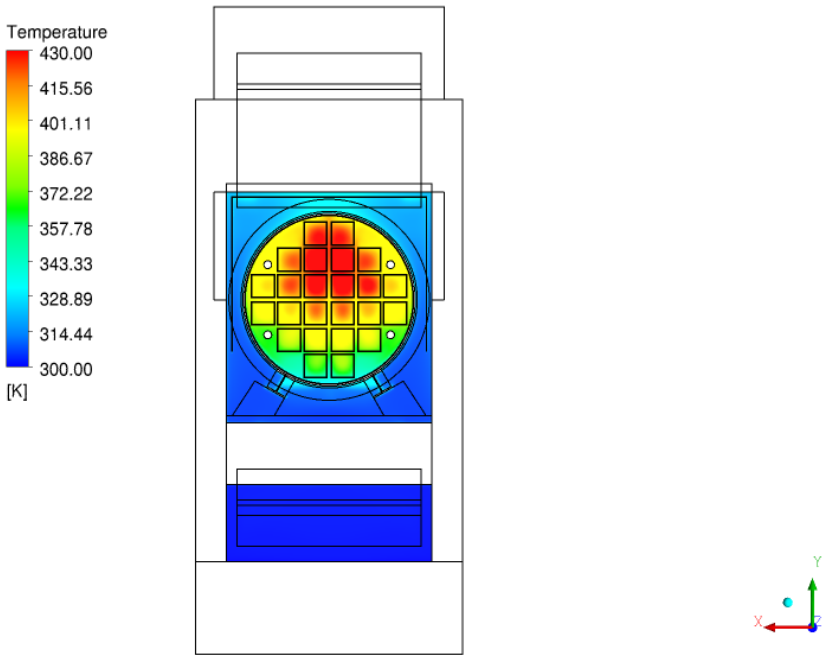

Figure 3-22. Temperature distribution for air and helium at axial cross-sectional plane for HSM–15 baseline case

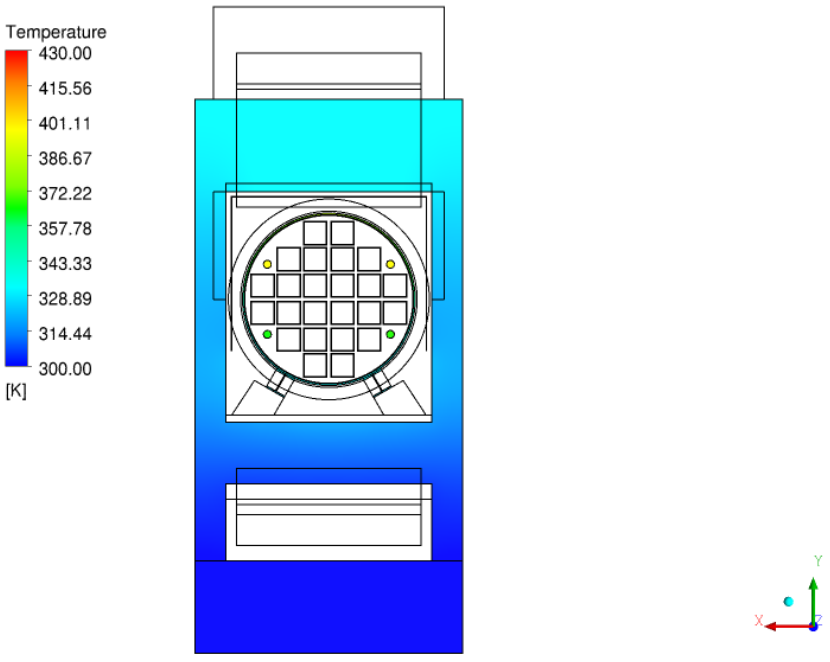

Figure 3-23. Temperature distribution for the solid regions at axial cross-sectional plane for HSM–15 baseline case

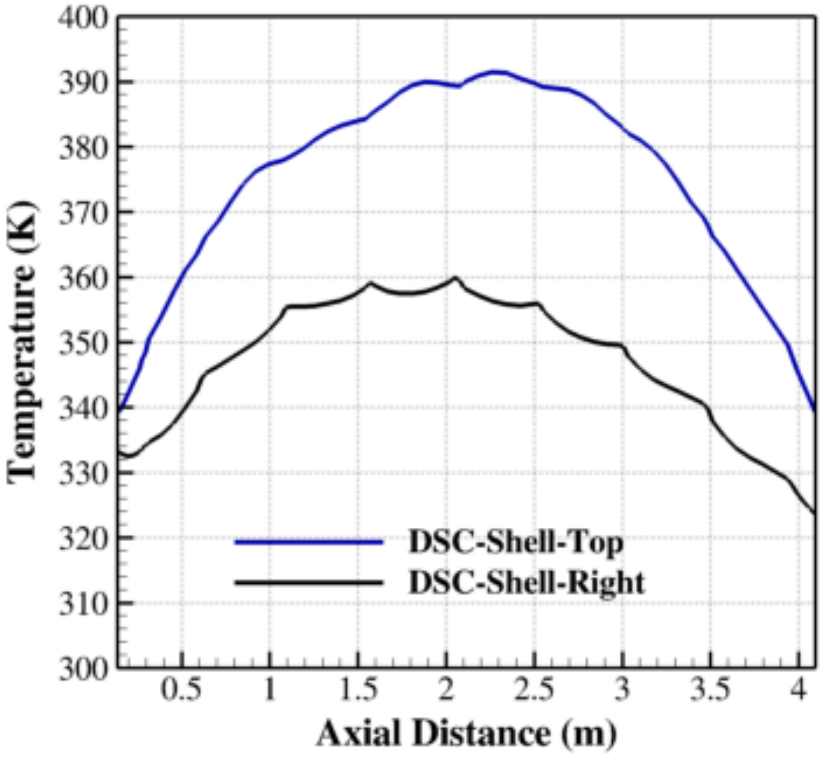

Figure 3-24. Computed temperature distributions along the axial distance for top and right of DSC shell for HSM–15 module

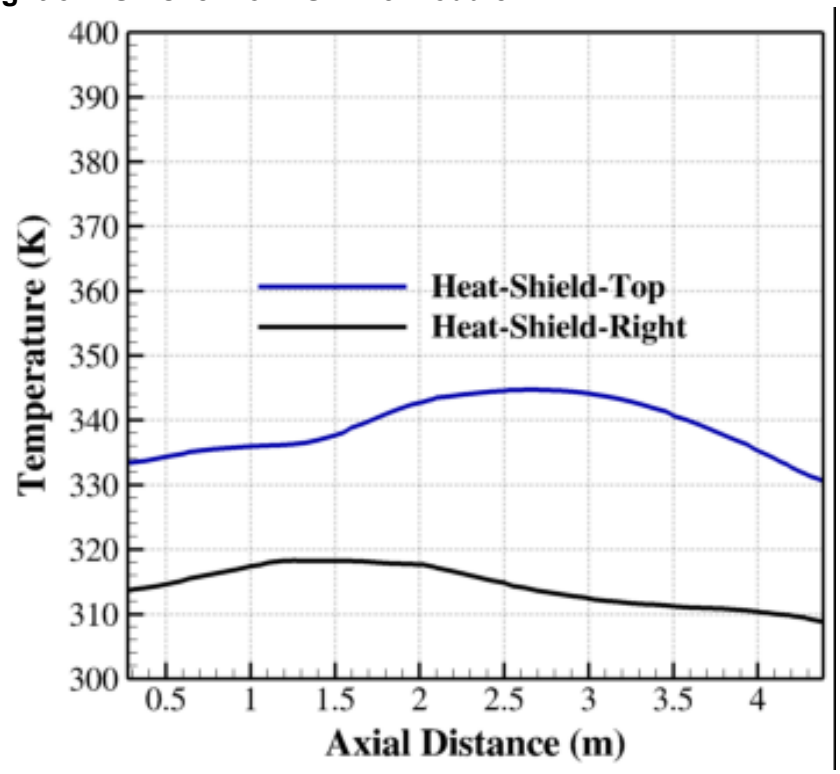

Figure 3-25. Computed temperature distributions along the axial distance for top of heat shield and right of heat shield

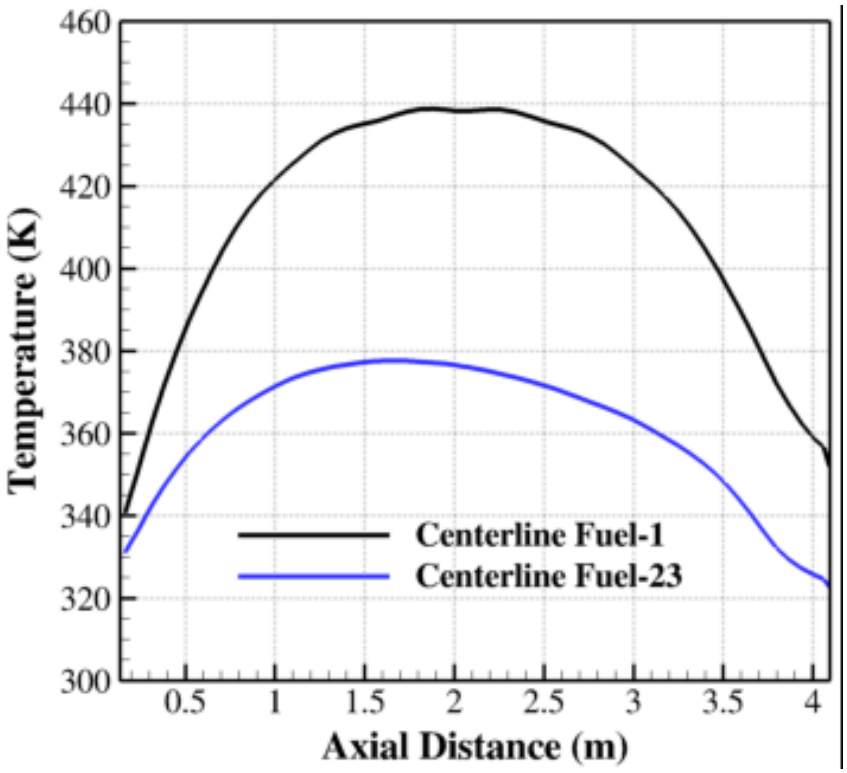

Figure 3-26. Computed temperature distributions along the axial distance for fuel region: distribution shown for fuel assemblies 1 and 23 for HSM–15 baseline case

3.2.2.2 Velocity Field

Figures 3-27 through 3-29 present the results for the predicted velocity field of the HSM–15 module. The airflow path and airflow circulation within the HSM–15 module are similar to those for HSM–1. However, the highest magnitude of the velocity {1.18 m/s [3.9 ft/s]} observed in the HSM–15 simulations is greater than the corresponding value {1.0 m/s [3.28 ft/s]} in the HSM–1 simulations observed in Figure 3-7. The higher velocity magnitude can be attributed to the higher heat load of HSM–15, which caused stronger convective flow.

3.2.2.3 Comparison with Measured Data

For the HSM–15 module, the only measured temperature is from under the grapple ring. The measured temperature is 324 K [124 °F], while the predicted temperature is 335 K [144 °F]. Prior to the measurement [Suffield et al 2012], the module door was open for approximately 20 minutes. For the same reasons discussed for HSM–1 (Section 3.2.1.3), it is expected that the measured temperature was lower than the temperature for the normally operated closed module.

3.3 Sensitivity Studies

Sensitivity studies of the HSM–1 module simulations were designed to evaluate the effects on computed results of mesh refinement, different turbulence models, varying porous media resistance, and insolation. In addition, a study was performed to assess the validity of the heat transfer coefficient, specified as a boundary condition on the external wall, by performing a simulation on an extended domain that included the surrounding atmosphere. Apart from the

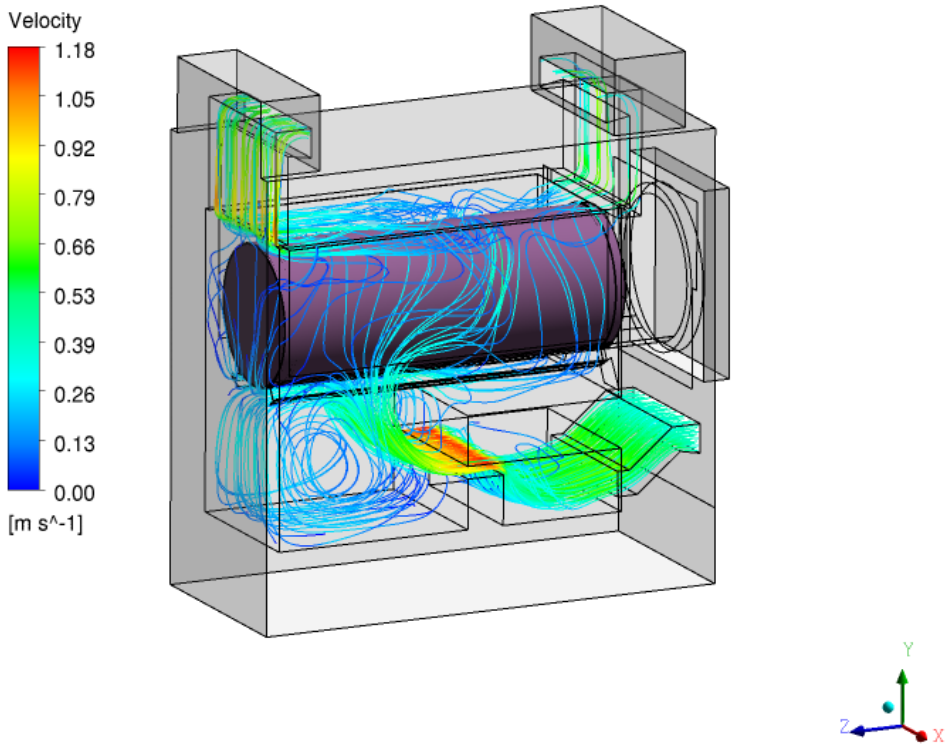

Figure 3-27. Streamlines showing the airflow path and airflow circulation within the HSM–15 module

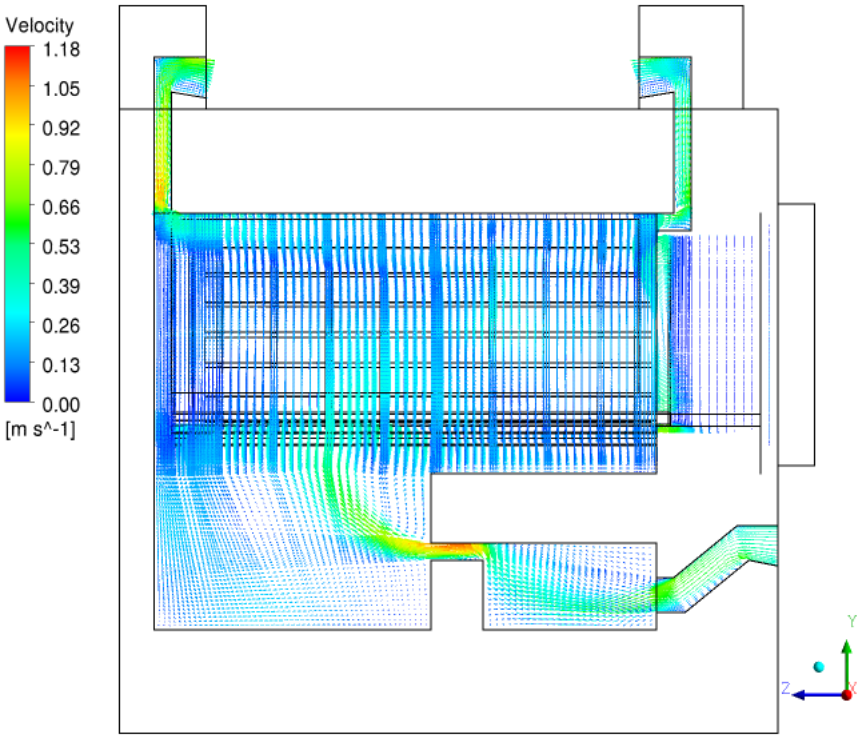

Figure 3-28. Velocity vector distribution at the transverse cross section for HSM–15 module

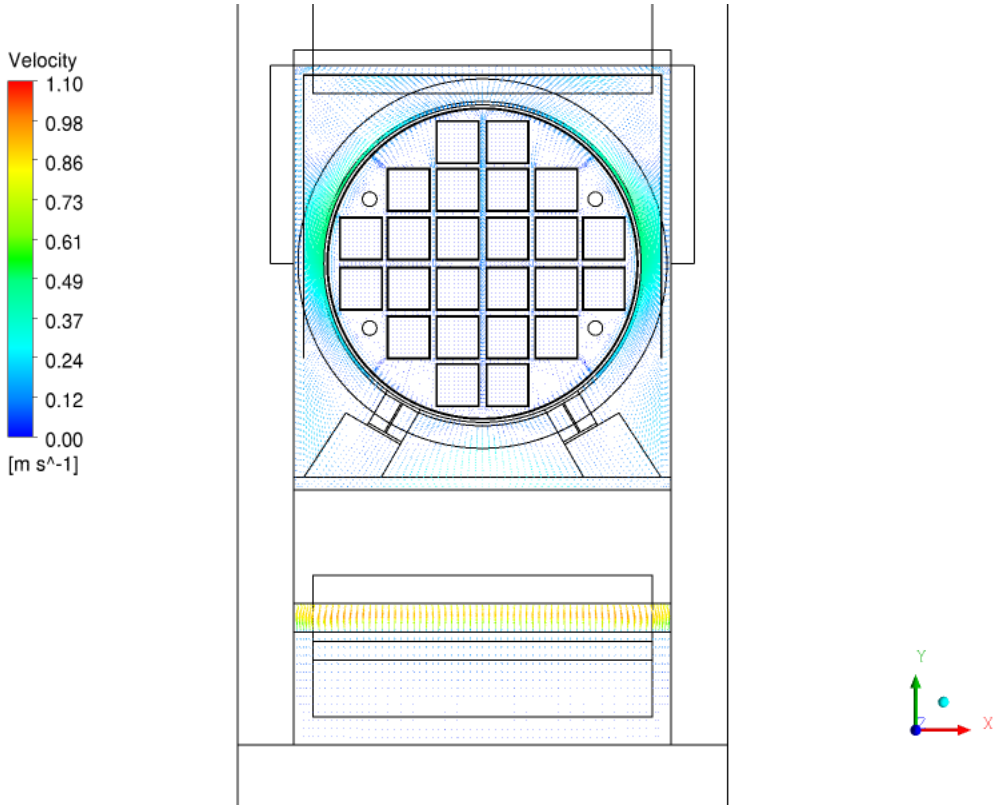

Figure 3-29. Velocity distribution at the axial cross section for HSM–15 module

sensitivity study on mesh refinement, all simulations used the baseline mesh. The decay heat load values calculated for June 2012 were used, as was a 28 °C [301 K, 82.19 °F] ambient temperature.

3.3.1 Effect of Mesh Refinement

The objective of this study was to evaluate the sensitivity of calculated temperature values to the DSC shell wall y^+ parameter, which is defined as the non-dimensional wall distance for a wall bounded flow and is often termed the law of the wall coordinate. The y^+ parameter is often used to describe the quality of mesh in the near wall region.

The specification of the DSC shell wall y^+ parameter controls the location of first node spacing perpendicular to the shell wall and the distribution of nodes within the boundary layer. The sharp temperature and velocity gradients in the boundary layer provide a strong control on the overall heat transfer process and, therefore, temperatures are likely to be especially sensitive to inadequate refinement in this zone. The sensitivity study was conducted by adapting and refining the mesh near the DSC shell outer wall, but not for the DSC shell inner wall. Due to the presence of smaller annuli between the DSC shell and spacer plates, mesh refinement for the inner wall was deemed not feasible. It is likely that outer wall mesh refinement has more effect on overall heat transfer, since the air flow outside of the DSC shell is turbulent and the helium flow inside the DSC shell is laminar. However, for a more comprehensive estimation of the effect of y^+, mesh refinement for both inner and outer walls of the DSC shell would be necessary. The effect of outer wall mesh refinement on the computed temperature distribution

is shown in Figures 3-30 through 3-32. Table 3-2 shows the computational mesh obtained due to adaptation and refinement that was used for this sensitivity study and the corresponding average y^+ value for the first grid point near the DSC outer wall.

Figure 3-30 shows that there is very little difference among the axial distributions of the predicted temperatures on the right side of the DSC shell for the three levels of grids. However, for the axial temperature distribution on the top of the DSC shell (Figure 3-31), the temperature distribution for the baseline grid is 5–7 K [9–13 °F] lower than the temperature distributions for the two fine discretization levels at the middle of the axial length. This is probably because the maximum temperature is predicted in the mid-region at the top of the DSC shell; that region is characterized by sharp near-wall gradients. The baseline grid, with a relatively higher value of y^+, results in lower values of predicted temperatures near the wall. The baseline grid was not fine enough in the near-wall region to capture the flow and temperature gradients in that particular region. The two levels of finer grid had enough resolution (lower values of y^+) to predict a higher value of the temperature. At the beginning and end of the axial length, the temperature distributions for the three grids are almost the same. Figure 3-32 shows an insignificant difference in the predicted temperatures in the axial direction for the three grids at fuel assembly 1. This may be due to the fact that the mesh was not refined for the DSC internal components and, as a result, the heat transfer rates calculated by the three meshes were nearly identical. The calculated values of the temperatures for the three levels of refinement are listed in Table 3-3. The maximum difference among the results for any location is 1.76 K [3.17 °F] and for almost all the observations, the difference is less than 0.5 K [0.9 °F].

In general, the close agreement between the simulated temperatures from all three grid levels indicates that all the computational meshes used in the simulations capture the thermal field adequately. The majority of the volume had a good quality grid in the original baseline mesh, resulting in no significant change in heat transfer and temperature values when the mesh was refined. In summary, the simulated temperatures and temperature distributions were generally not sensitive to the DSC shell y^+.

3.3.2 Effect of Turbulence Models

The effect of the choice of turbulence model on the computed temperature distribution is shown in Figures 3-33 through 3-36. The turbulence models considered in the sensitivity study were:

(i) standard k-ε model with scalable wall function,

(ii) k-ε model with near-wall low Reynolds number correction and buoyancy effects without wall functions (baseline case),

(iii) standard shear stress transport (SST) k-ω model with low Reynolds number correction without wall functions, and

(iv) SST k-ω model with buoyancy and low Reynolds number correction without wall functions.

Figures 3-33 and 3-34 show the axial temperature distributions on the right side of the DSC shell and on the top of the DSC shell for the turbulence models. Figures 3-35 and 3-36 show the axial temperature distribution in fuel assemblies 1 and 23, respectively, for the turbulence models. The simulated results for the SST k-ω models (both with and without buoyancy) are almost identical. For the k-ε model, results show that including low Reynolds number correction with buoyancy resulted in lower values of the predicted temperatures than any other model, and

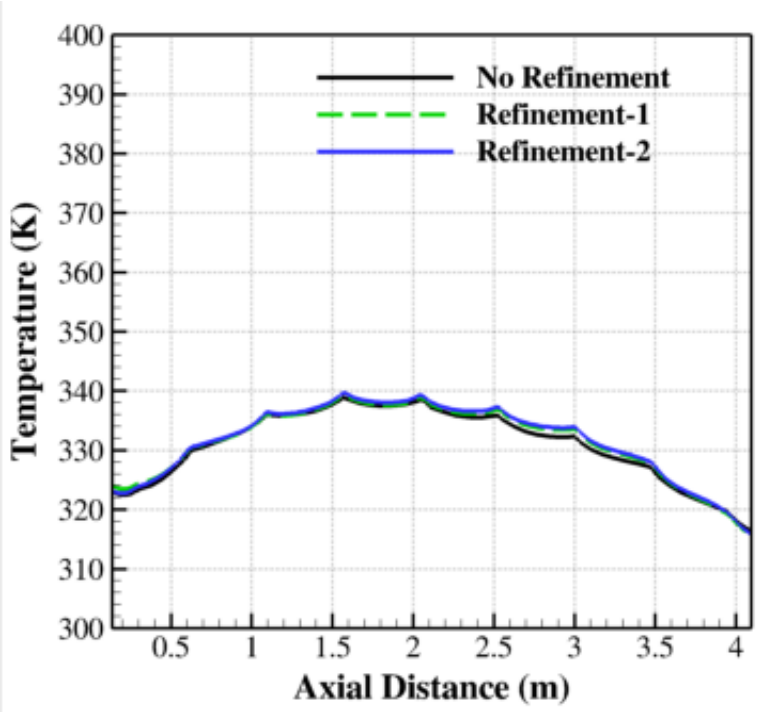

Figure 3-30. Computed temperature distributions along the axial distance for right side of DSC shell: mesh refinement for HSM–1 module

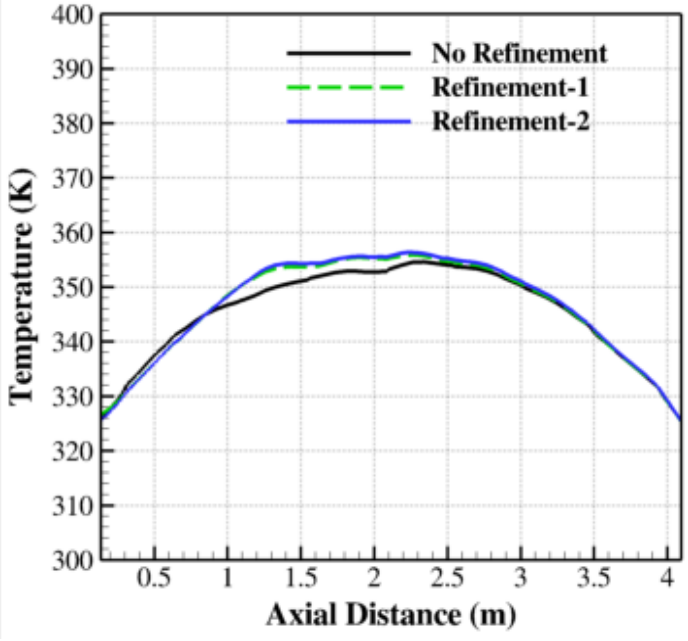

Figure 3-31. Computed temperature distributions along the axial distance for top of DSC shell: mesh refinement for HSM–1 module

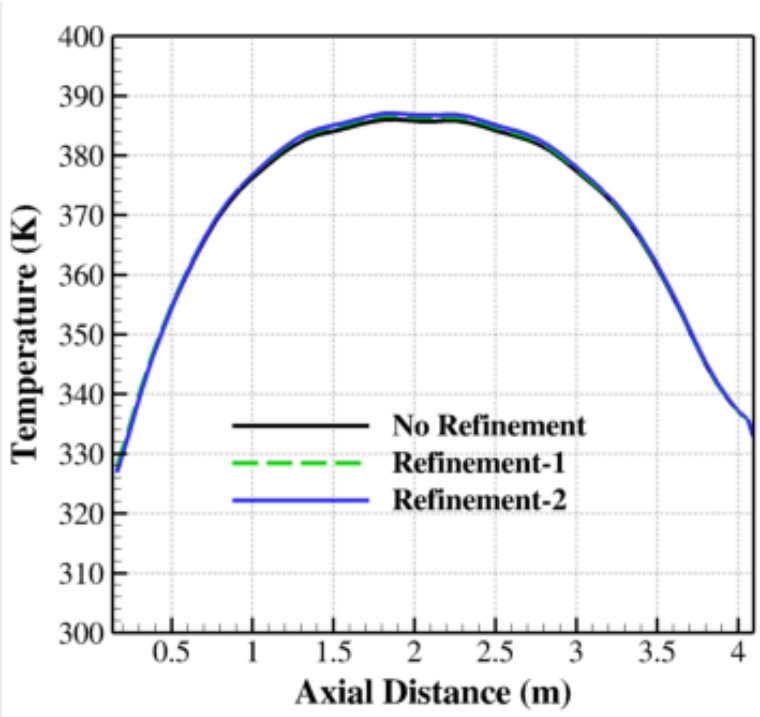

Figure 3-32. Computed temperature distributions along the axial distance for fuel assembly 1: mesh refinement for HSM–1 module

Table 3-2. Computational mesh used in the mesh refinement study

Simulation cases for HSM–1	Total number of grids	Minimum y^+ on DSC outer wall	Maximum y^+ on DSC outer wall	Surface Average y^+ on DSC outer wall
Baseline Grid	3.2×10^6	0.054	12.21	2.97
Refinement-1	4.2×10^6	0.038	10.60	1.575
Refinement-2	6.5×10^6	0.027	7.01	0.8193

Table 3-3. Comparison of predicted temperatures for the three different levels of mesh: simulations for HSM–1 module

Location	Baseline mesh (K) [°F = 1.8 K-460]	Fine mesh 1 (refinement-1) (K) [°F = 1.8 K-460]	Fine mesh 2 (refinement-2) (K) [°F = 1.8 K-460]
Under Grapple ring	324.18	325.29	324.20
0-m-side-right	323.04	323.70	322.94
0-m-side-top	325.18	326.04	324.98
0-m-side-left	322.68	323.61	322.81
0-m-rail-right	319.05	319.09	319.51
0-m-rail-left	319.05	320.01	319.67
0.51-m-side-right	325.74	326.94	327.17
0.51-m-side-top	336.94	336.01	336.25
0.51-m-side-left	324.94	326.04	326.63
0.51-m-rail-right	318.81	319.31	319.48

Table 3-3. Comparison of predicted temperatures for the three different levels of mesh: simulations for HSM–1 module

Location	Baseline mesh (K) [°F = 1.8 K-460]	Fine mesh 1 (refinement-1) (K) [°F = 1.8 K-460]	Fine mesh 2 (refinement-2) (K) [°F = 1.8 K-460]
0.51-m-rail-left	318.7	319.16	319.29
1.02-m-side-right	334.35	334.05	334.51
1.02-m-side-top	346.89	348.65	347.68
1.02-m-side-left	333.39	333.86	334.34
1.02-m-rail-right	322.04	322.22	322.74
1.02-m-rail-left	321.97	321.93	322.44

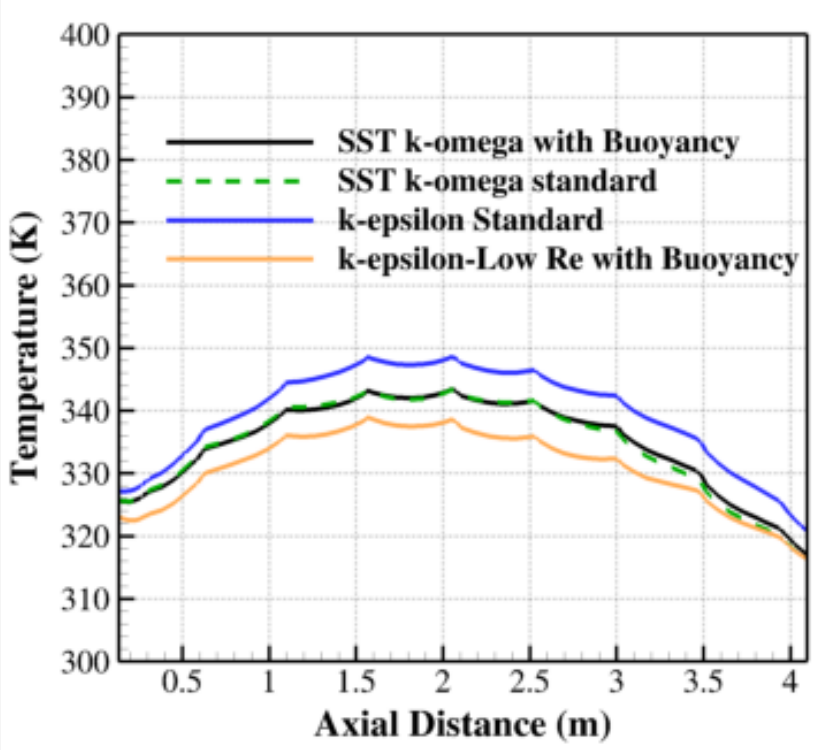

Figure 3-33. Computed temperature distributions along the axial distance for right side of DSC shell: effect of turbulence model for HSM–1 module

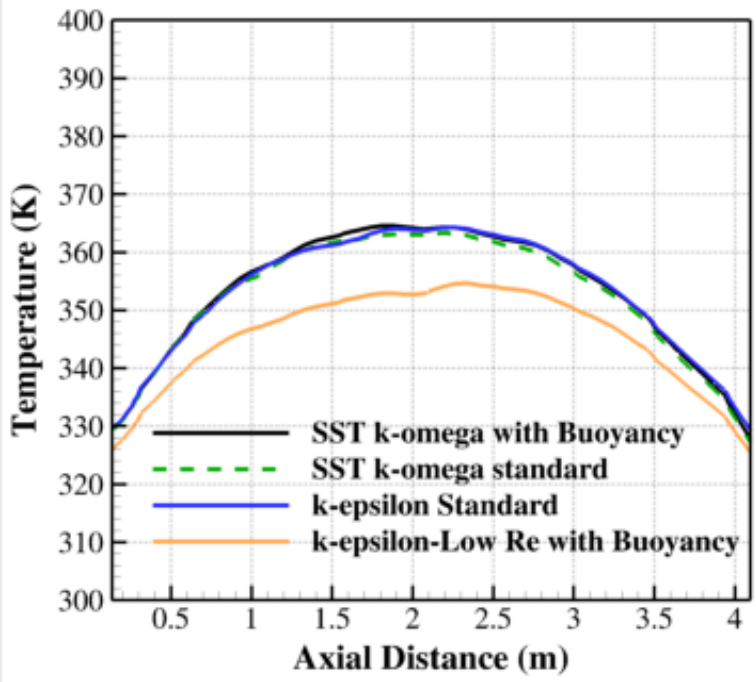

Figure 3-34. Computed temperature distributions along the axial distance for top of DSC shell: effect of turbulence models for HSM–1 module

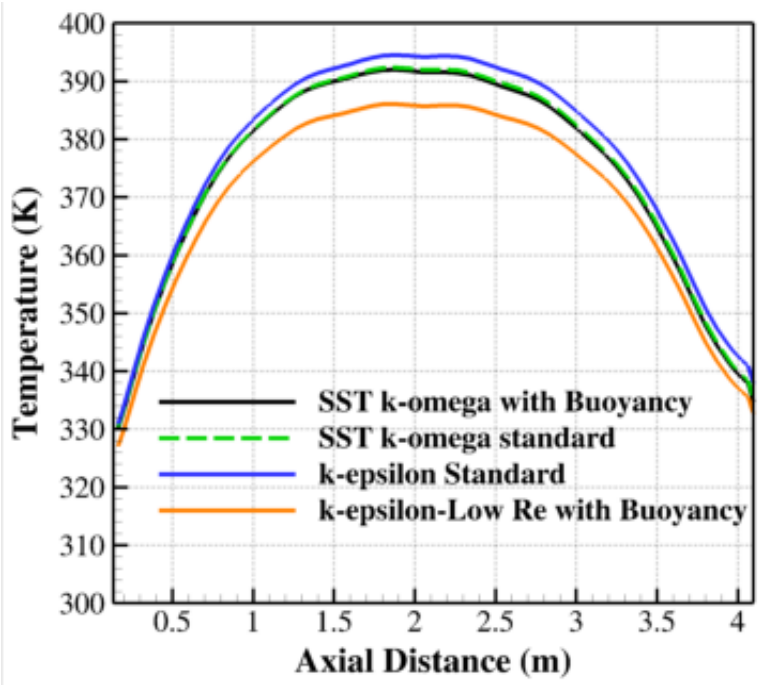

Figure 3-35. Computed temperature distributions along the axial distance for fuel assembly 1: effect of turbulence model for the HSM–1 module

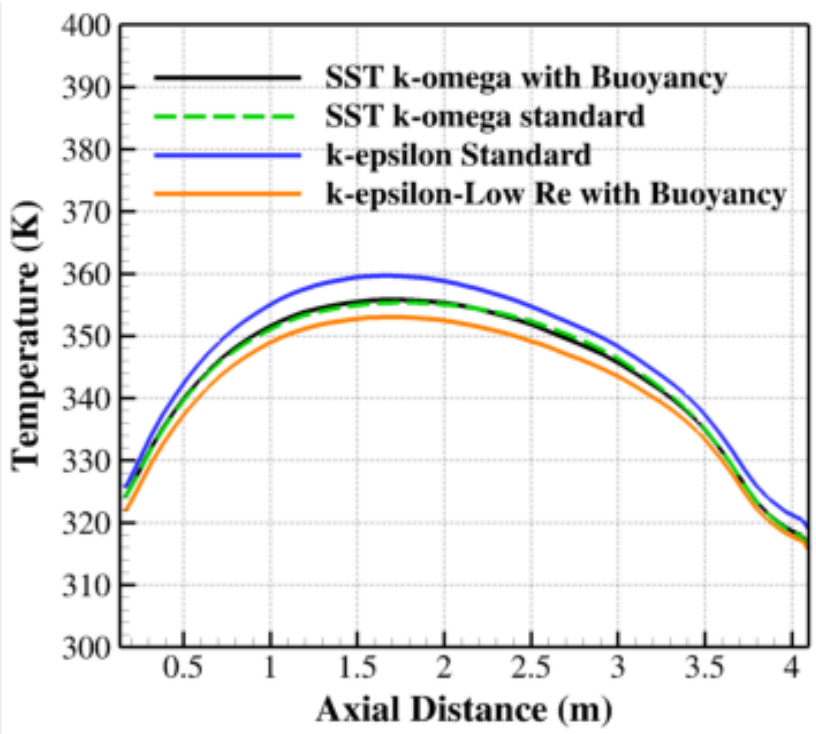

Figure 3-36. Computed temperature distributions along the axial distance for fuel assembly 23: effect of turbulence model for the HSM–1 module

the temperatures are closest to the measured values at all locations. The calculated values of the temperatures for all the turbulence models are listed in Table 3-4. In general, the calculated values are numerically close, with the maximum difference among predicted temperatures being 10.15 K [18.27 °F], at the top central part of the DSC shell.

3.3.3 Effect of Porous Media Resistance

The effects of porous media flow resistance on the computed temperature distribution are shown in Figures 3-37 through 3-40. The cases considered include the baseline case, a higher porous media resistance compared to the baseline case, a lower porous media resistance compared to the baseline case, zero resistance, and one case with no porous media. In the zero resistance case, the porous media settings of the solver were retained, but the individual resistance coefficients were set to zero. For the no porous media case, the porous media settings within the solver were turned off and the fuel assembly region was treated as a regular fluid zone. The higher and lower porous media resistance coefficients were arbitrarily set as one order of magnitude higher and lower than the baseline case. Table 3-5 lists the viscous and resistance coefficients that were used in this study.

Figures 3-37 and 3-38 show the axial temperature distribution on the right side of the DSC shell and on the top of DSC shell for the different values of the porous media resistance. Figures 3-39 and 3-40 show the axial temperature distribution for fuel assemblies 1 and 23, respectively, for the different porous media resistance values. The simulation results show that increasing or decreasing the porous media resistance relative to the baseline value does not significantly affect the temperature distribution.

Table 3-4. Comparison of predicted temperatures for different turbulence models: simulations for HSM–1 module

Location	Baseline case, low re standard k-ε with buoyancy (K) [°F = 1.8 K-460]	Standard k-ε model with scalable wall function and buoyancy effects (K) [°F = 1.8 K-460]	SST k-ω model with low Reynolds number corrections (K) [°F = 1.8 K-460]	SST k-ω model with low Reynolds number corrections and buoyancy effects (K) [°F = 1.8 K-460]
Under grapple ring	324.18	327.99	327.02	326.922
0-m-side-right	323.04	326.92	325.63	325.64
0-m-side-top	325.18	328.82	328.65	328.39
0-m-side-left	322.68	326.78	325.35	321.21
0-m-rail-right	319.05	322.75	321.15	321.26
0-m-rail-left	319.05	322.56	321.05	320.98
0.51-m-side-right	325.74	332.17	329.46	329.83
0.51-m-side-top	336.94	342.38	342.64	342.51
0.51-m-side-left	324.94	332.04	328.83	329.04
0.51-m-rail-right	318.81	323.27	320.52	320.64
0.51-m-rail-left	318.7	323.29	320.21	320.64
1.02-m-side-right	334.35	342.41	338.3	338.68
1.02-m-side-top	346.89	356.68	357.04	355.74
1.02-m-side-left	333.39	342.19	337.29	337.33
1.02-m-rail-right	322.04	327.22	323.25	323.38
1.02-m-rail-left	321.97	327.2	322.9	323.65

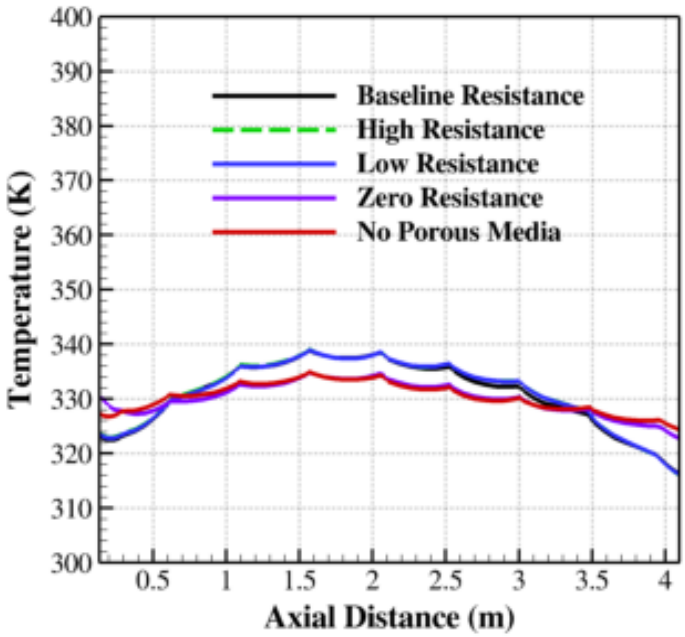

Figure 3-37. Computed temperature distributions along the axial distance for right side of DSC shell: effect of porous media for HSM–1 module

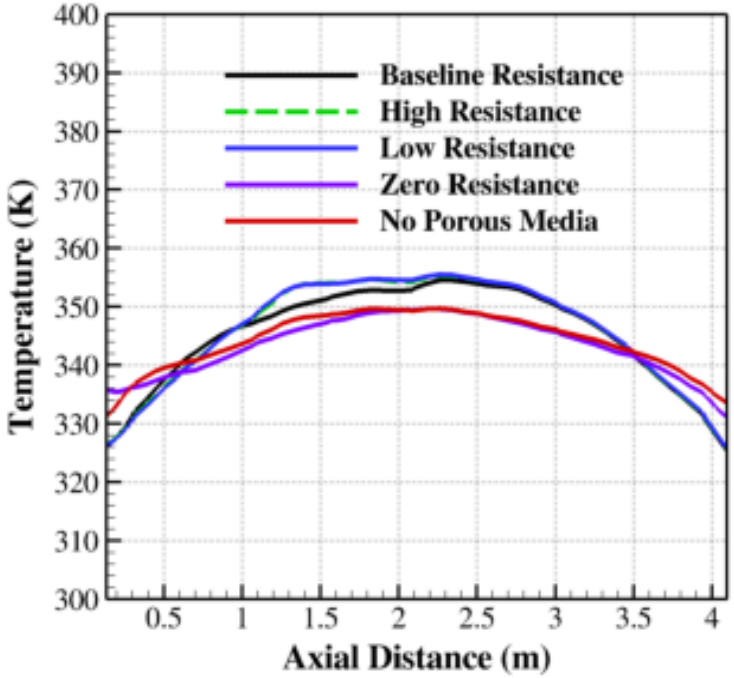

Figure 3-38. Computed temperature distributions along the axial distance for top of DSC shell: effect of porous media for HSM–1 module

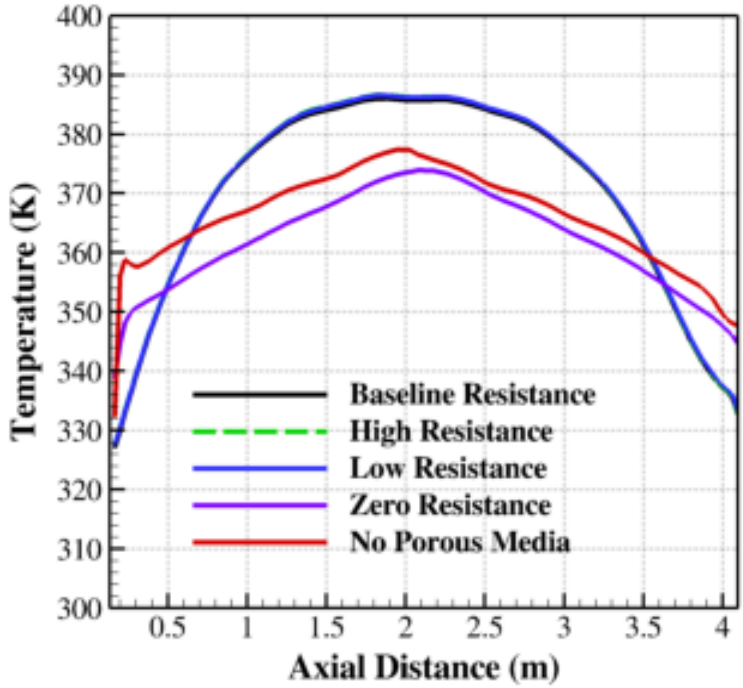

Figure 3-39. Computed temperature distributions along the axial distance for fuel assembly 1: effect of porous media for HSM–1 module

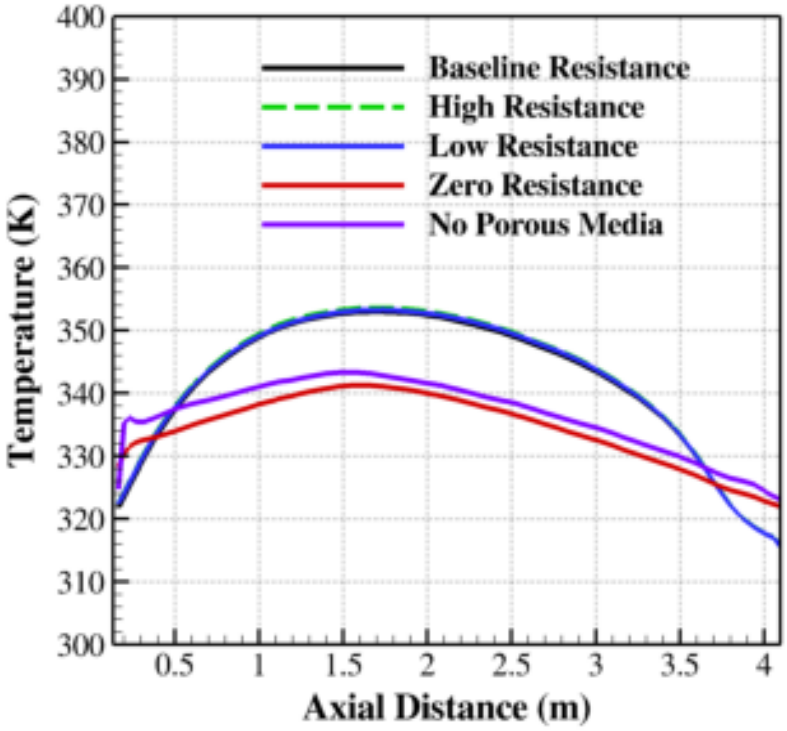

Figure 3-40. Computed temperature distributions along the axial distance for fuel assembly 23: effect of porous media for HSM–1 module

Table 3-5. Resistance coefficients used for porous media resistance parametric study

		Baseline	High resistance	Low resistance	Zero resistance	No porous media
Viscous Resistance ($1/m^2$) [$1/m^2$ = $0.0931/ft^2$]	Axial Direction	1.284×10^5	10^7	1000	0.0	Not specified
	Radial Direction-1	10^8	10^8	10^8	0.0	Not specified
	Radial Direction-2	10^8	10^8	10^8	0.0	Not specified
Inertial Resistance (1/m) [1/m = 0.305 1/ft]	Axial Direction	0.78	10	0.01	0.0	Not specified
	Radial Direction-1	100	100	100	0.0	Not specified
	Radial Direction-2	100	100	100	0.0	Not specified

However, the zero resistance and no porous media cases do alter the basic temperature distribution pattern, particularly for fuel assemblies 1 and 23. The calculated values of the temperatures and their comparisons for all the different porous media resistance cases are shown in Table 3-6. The values listed in the table substantiate the observation that there is no significant difference among the baseline, high resistance, and low resistance cases, with the

Table 3-6. Comparison of predicted temperatures (K) for different porous media resistance values: simulations for HSM–1 module

Location	Baseline (K) [°F = 1.8 K-460]	High resistance (K) [°F = 1.8 K-460]	Low resistance (K) [°F = 1.8 K-460]	Zero resistance (K) [°F = 1.8 K-460]	No porous media (K) [°F = 1.8 K-460]
Under grapple ring	324.18	324.88	324.77	333.12	328.33
0-m-side-right	323.04	323.57	323.48	330.94	327.09
0-m-side-top	325.18	325.68	325.58	334.93	330.08
0-m-side-left	322.68	323.27	323.19	330.40	326.68
0-m-rail-right	319.05	319.88	319.76	324.13	321.75
0-m-rail-left	319.05	319.69	319.56	323.86	321.75
0.51-m-side-right	325.74	326.05	325.85	327.47	328.56
0.51-m-side-top	336.94	335.79	335.46	337.68	339.35
0.51-m-side-left	324.94	325.38	325.34	327.45	327.92
0.51-m-rail-right	318.81	319.39	319.23	319.92	319.61
0.51-m-rail-left	318.7	319.14	318.94	319.68	319.35
1.02-m-side-right	334.35	334.47	334.26	331.40	332.07
1.02-m-side-top	346.89	347.31	347.51	342.85	343.92
1.02-m-side-left	333.39	333.95	333.82	330.81	331.74
1.02-m-rail-right	322.04	322.53	322.34	320.39	320.44
1.02-m-rail-left	321.97	322.25	322.01	320.04	320.04

maximum difference among predicted results being 1.5K [2.7 °F]. But the zero and no porous media approximations yield a significantly different temperature pattern. It is expected that the zero resistance and no porous media specification cases would yield identical outcomes. However, the difference in the patterns of temperature distributions between these two cases indicates that the source terms in the flow solver specified for porous media with zero resistance may have affected the solution, though these sources are expected to be zero. In general, this study shows that the calculated temperatures are not sensitive to the exact resistance coefficients, but the fuel assemblies cannot be assumed as free flow zones with no porous resistance.

3.3.4 Effect of Insolation

The effect of insolation was evaluated using two cases: the baseline case (which includes insolation) and the baseline case modified to omit insolation. The solar insolation loads in the baseline case (see Section 2.4) are taken from the values prescribed in the regulations for packaging and transportation of radioactive material [10 CFR Part 71]. Section 71.71 of 10 CFR Part 71 specifies a solar load of800 g-cal/cm^2 [2,949.35 BTU/ft^2] for horizontal surfaces and 200 g-cal/cm^2 [737.337 BTU/ft^2] for flat non-horizontal surfaces applied over a 12-hour period. For the simulation case without insolation, the simulation settings and the parameters are identical to the baseline case except that no insolation flux is specified. Figure 3-41 shows the axial temperature distribution on the top of DSC shell and on the right side of the DSC shell for the two cases. Figure 3-42 shows the axial temperature distribution for fuel assemblies 1 and 23 for the two cases. Both Figures 3-41 and 3-42 indicate that omitting insolation reduces the simulated temperatures, which is expected because insolation provides an additional heat

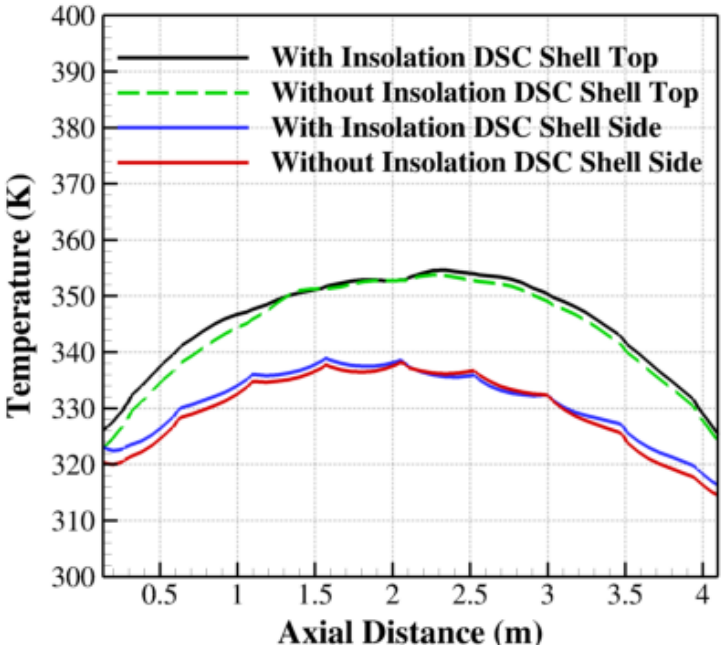

Figure 3-41. Computed temperature distributions along the axial distance for right side and top of DSC shell: effect of insolation for HSM–1 module

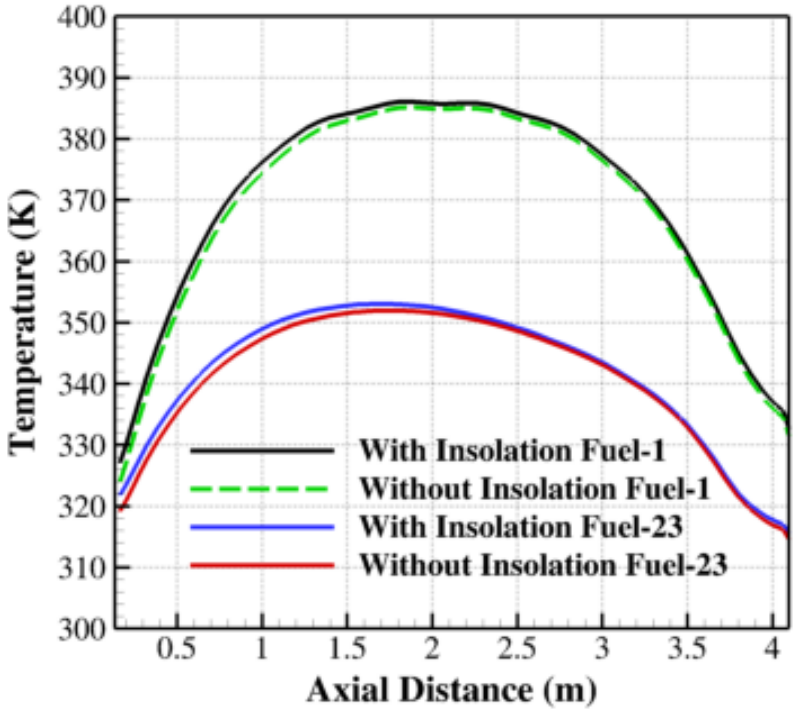

Figure 3-42. Computed temperature distributions along the axial distance for fuel assemblies 1 and 23: effect of insolation for HSM–1 module

load on the external surfaces of the module. Peak temperatures are affected only by approximately 1 to 2 K [2 to 4 °F] by adding insolation, but the temperature patterns differ slightly and temperatures nearer the DSC ends differ by up to 4 K [7.2 °F].

The calculated values of the temperatures for the two cases are shown at the measurement points from Table 3-1 in Table 3-7. The values in the table substantiate that including insolation consistently increases predicted temperatures. The maximum temperature difference between the results obtained using insolation and the baseline case is 3.77 K [6.78 °F]. In general, this study shows that insolation does affect the internal temperature of the storage system and therefore should be considered.

3.3.5 Effect of Including the Surrounding Atmosphere in the Computational Domain

A sensitivity study was performed to analyze the effect of an extended domain on the predicted temperature field. The primary objective of this specific study was to assess the validity of the heat transfer coefficient specified on the outer walls for the baseline cases, which use a computational domain that does not include the extended atmospheric domain. The baseline case uses a constant heat transfer coefficient of 10 W/m^2K [1.70 BTU h^{-1} ft^{-2} $°F^{-1}$] applied on external surfaces; in the sensitivity study, surface-averaged heat transfer coefficients were derived from simulation results. For this study with extended domain, the standard k-ε model with scalable wall function was used. This choice of turbulence model was based on the quality of the grid on the outer surface of the concrete module, which was not as fine as the mesh around the DSC shell. At the outer exterior of the domain, a pressure inlet boundary condition with zero gauge pressure was specified. The bottom surface of the domain was specified as a wall and the back surface of the domain was specified to have a symmetric boundary condition.

Figure 3-43 shows the extended domain used for this study along an axial plane. The domain extends to 2.5 times the height of the HSM–1 module in the vertical direction, 1.5 times the length of the HSM–1 module in the horizontal direction, and 1.5 times the width of the HSM–1 module in the span wise directions. The boundaries of the extended domain are maintained at ambient temperature and pressure. The sensitivity study is expected to slightly underestimate heat transfer coefficients because wind, which acts to cool the module, was not included.

Figures 3-44 and 3-45 show simulated temperatures and velocity magnitudes at an axial mid-plane of the computational domain. Temperatures calculated from the extended domain simulation were compared with computations performed on the regular domain using the same turbulence model (Section 3.3.2). The temperature differences between these two cases in the fuel assembly region were less than 2.5 K [4.5 °F]. The velocity distribution and magnitude within the module are similar to those of the baseline case observed in Figure 3-13; outside the module, the heated air rises vertically. Figure 3-46 shows the computed convective heat transfer coefficient distribution on the external concrete surface. Using simulation results with the extended atmospheric domain to calculate surface-averaged heat transfer coefficients results in values of 9.467 W/m^2K [1.67 BTU h^{-1} ft^{-2} $°F^{-1}$] and 9.240 W/m^2K [1.63 BTU h^{-1} ft^{-2} $°F^{-1}$] for horizontal and vertical surfaces, respectively. These compare well with the value of 10 W/m^2K [1.70 BTU h^{-1} ft^{-2} $°F^{-1}$] used in the baseline simulations and would be expected to increase slightly if wind were included in the study. Accordingly, the heat transfer coefficient used for the baseline case appears to be a reasonable value.

Table 3-7. Comparison of predicted temperatures for with and without insolation: simulations for HSM–1 module

Location	Baseline (K) [°F = 1.8 K-460]	Without insolation (K) [°F = 1.8 K-460]
Under Grapple ring	324.18	320.23
0-m-side-right	323.04	320.11
0-m-side-top	325.18	321.95
0-m-side-left	322.68	319.83
0-m-rail-right	319.05	316.32
0-m-rail-left	319.05	316.28
0.51-m-side-right	325.74	323.92
0.51-m-side-top	336.94	334.09
0.51-m-side-left	324.94	323.19
0.51-m-rail-right	318.81	316.70
0.51-m-rail-left	318.70	316.75
1.02-m-side-right	334.35	332.96
1.02-m-side-top	346.89	344.85
1.02-m-side-left	333.39	331.75
1.02-m-rail-right	322.04	320.23
1.02-m-rail-left	321.97	320.41

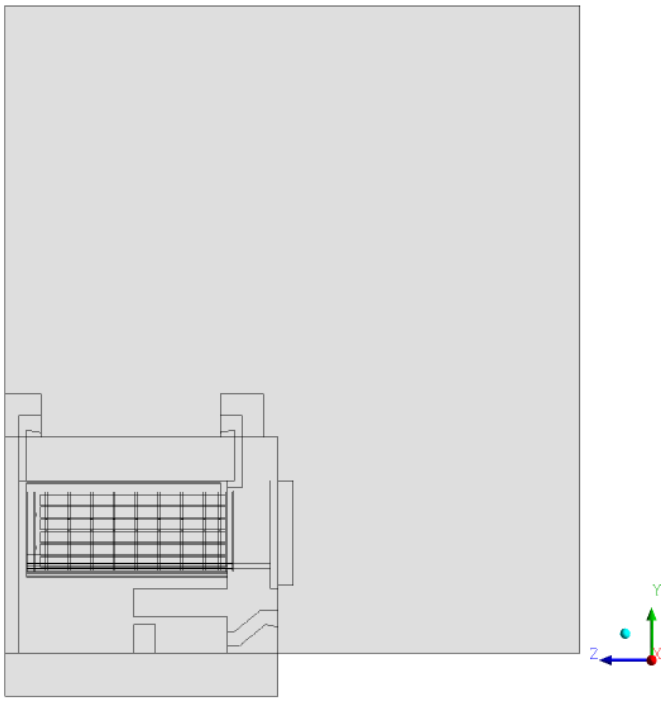

Figure 3-43. Extended domain for the study of the effect of atmosphere for HSM–1 module

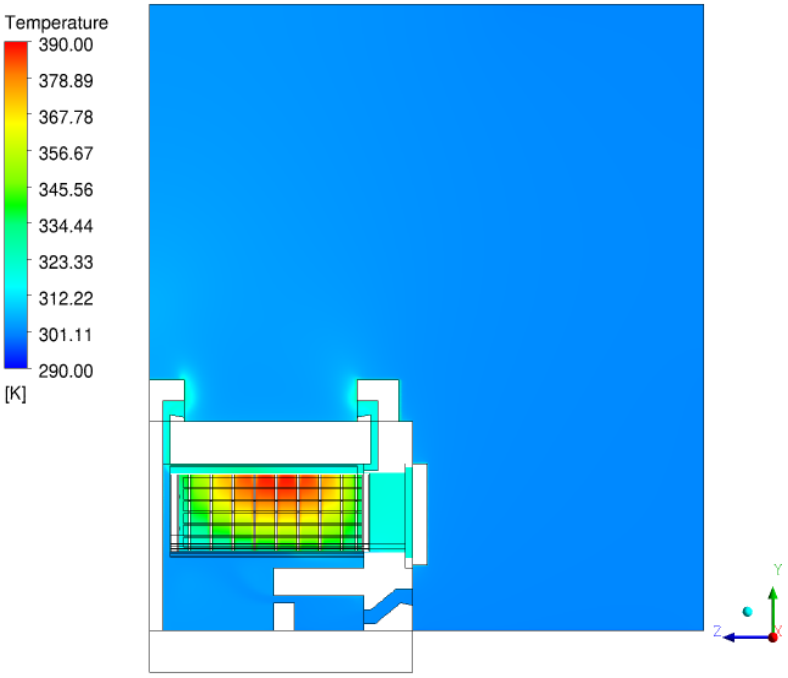

Figure 3-44. Temperature contours at an axial mid-plane of the extended domain: effect of atmosphere for HSM–1 module

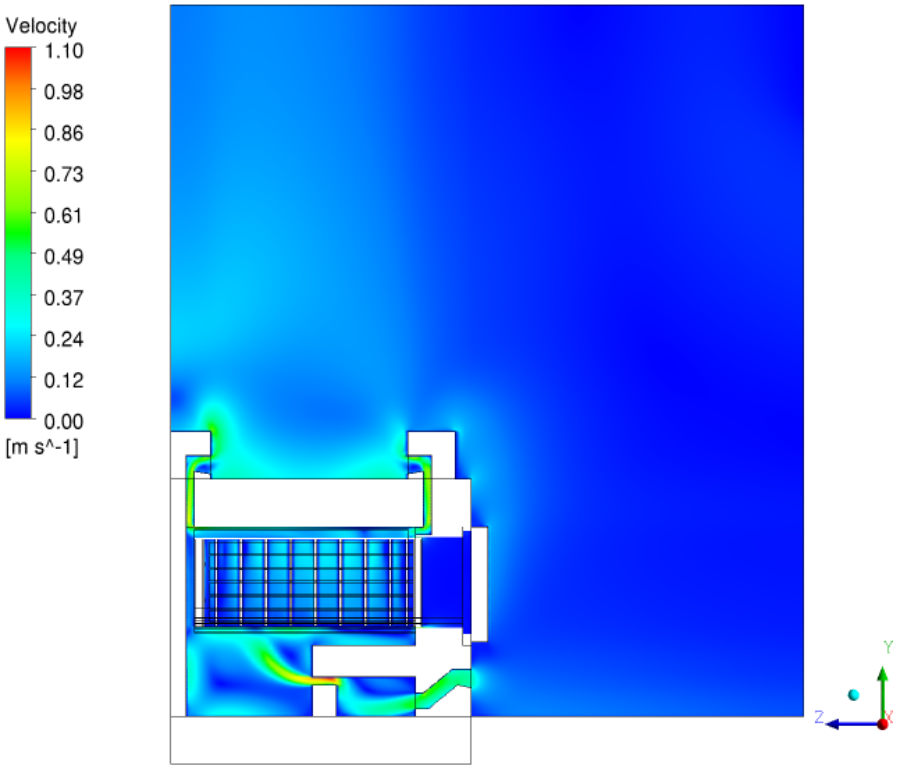

Figure 3-45. Velocity contours at an axial mid-plane of the extended domain: effect of atmosphere for HSM–1 module

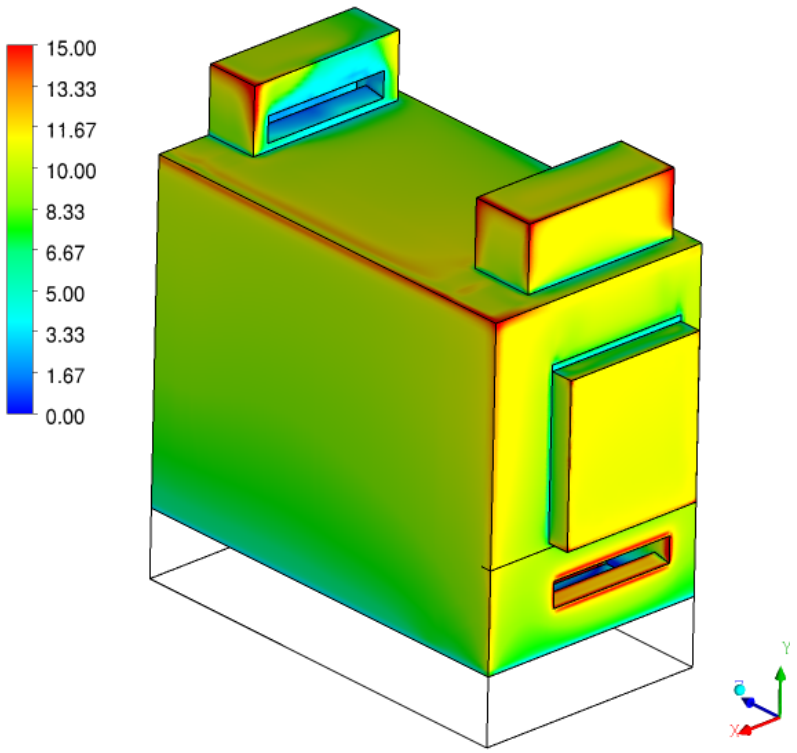

Figure 3-46. Computed heat transfer coefficient distribution over the HSM–1 module: effect of extended domain and atmosphere

3.4 Observations From Benchmark Study

Detailed 3-D computational models were developed for thermal analyses of the HSM–1 and HSM–15 modules. Simulations were performed to benchmark the developed models by comparing the numerical predictions with measured data and to investigate the sensitivity of the results to model assumptions and boundary conditions. The major observations from this benchmark study are as follows:

- The simulations provided valuable insight into the heat transfer process inside the DSC. The buoyancy-driven natural convection flow of the air and the helium gas influences the fuel region temperature and the DSC shell temperature.

- Predicted temperatures were consistently higher than values measured in the field. The measured values are subject to significant uncertainty due to a number of factors, including difficulty in probe insertion, open module doors that permitted atmospheric mixing, and a one-time measurement without any repetition. Therefore, the measured temperatures may not be truly representative of typical operating conditions with a closed door.

- A parametric study of sensitivity of the computed results to y^+ and mesh refinement to improve wall y^+ showed no significant change in overall heat transfer and temperature distribution when the mesh is refined relative to the baseline mesh.

- The baseline low Reynolds k-ε model-predicted temperatures were closest to the measured values. The maximum and minimum deviations for this case were 25.7 K [46.26 °F] and 3.33 K [5.99 °F], respectively.

- A sensitivity study with the turbulence model showed that including the low Reynolds number correction in the k-ε model resulted in lower values of the predicted temperatures on the DSC outer shell.

- An order of magnitude increase or decrease in porous media resistance (compared to baseline) did not affect the temperature distribution. However, zero resistance and assuming no porous media significantly flattened the temperature distribution pattern.

- Omitting the solar flux on external surfaces resulted in a temperature drop of up to 4 K [7.2 °F] and steeper temperature gradients, although peak temperatures were affected by a smaller amount.

- The predicted temperatures with an extended domain were comparable to those obtained from the regular domain simulation using the same turbulence model. The surface-averaged heat transfer coefficient values used in the baseline case were found to be reasonable based on the extended domain study.

4. THERMAL EVOLUTION SIMULATIONS

This chapter presents the results of simulations performed to predict storage module temperatures for up to 300 years of storage in horizontal storage modules HSM–1 and HSM–15. The analysis was performed using a sequence of steady-state simulations based on the projected decay heat over the 300-year period.

4.1 Numerical Approach to Thermal Evolution Analysis

A multi-step, steady-state analysis approach was used to simulate the thermal behavior of the storage modules. In this approach, a steady-state analysis was performed at selected time points covering the 300-year time span. At each time step, quasi-steady behavior of the flow and thermal field within and around the storage modules was assumed. Independently calculated heat loads at the discrete time points were used in the simulations.

For both HSM–1 and HSM–15, a 5-year interval was used to calculate the discrete time points for the first 100 years after storage, while a 10-year interval was used for the remaining 200 years of storage. Simulations were specifically performed for the calendar year 2012 because the observations were made at that time for both HSM-1 and HSM-15. For HSM–1, the fuel was loaded in the storage module in 1993. To span the 300 years of storage, simulations in this study were performed at specified times from 1993 to 2293. For the HSM–15 module, the fuel was loaded in year 1996 and simulations were conducted until year 2297, to cover the 301-year storage time. The span of simulation was extended by a year for HSM-15 to accommodate the calendar year 2012 in the series and maintain time steps of 5 and 10 years. The heat load values specified at discrete time points were based on the decay characteristics of the fuel and inventory, calculated in a separate analysis. The calculated decay heat load values used in the simulations for some specific years are provided in Tables 4-1 and 4-2 for HSM–1 and HSM–15, respectively. The fuel assembly loading identification and locations are shown in Figures 2-13 and 2-14 for HSM–1 and HSM–15, respectively. The heat load calculated for each of the fuel assemblies at different years was applied as a uniform volumetric heat generation rate over the active fuel length within each fuel region. All simulations performed for this analysis used the baseline computational grid and input parameters for both HSM–1 and HSM–15 (see Chapter 2 for a description). Insolation was included and the k-ε turbulence model with low Reynolds number correction and buoyancy effects was used.

Selected simulation results are presented for calendar years 1993, 2093, 2193, and 2293 for HSM–1, and calendar years 1996, 2097, 21967 and 2297 for HSM–15, to highlight the evolution of temperature with time. Chapter 3 presents results for the year 2012 for both HSM–1 and HSM–15 as the baseline simulations.

4.2 Results of Thermal Evolution Simulations

The thermal evolution simulations focus on the maximum and minimum temperatures for particular module components, including the cladding, fuel sleeves, spacer plates, the dry storage canister (DSC) shell, and the heat shield. Snapshots along a transverse cross section for the temperature distribution in the airflow pathways and within the DSC are also provided for context. The maximum and minimum temperatures in the fuel assembly region are used to represent maximum and minimum cladding temperatures, because the fuel assembly region is approximated as a continuous porous region (see Chapter 2).

Table 4-1. Calculated decay heat load values at different years for HSM–1 module

Assembly ID	Calculated 1993 heat load (start of storage) (Watt) 1 Watt = [3.413 BTU/hr]	2012 heat load (current year of measurement) (Watt) 1 Watt = [3.413 BTU/hr]	Calculated 2093 heat load (100 years of storage) (Watt) 1 Watt = [3.413 BTU/hr]	Calculated 2193 heat load (200 years of storage) (Watt) 1 Watt = [3.413 BTU/hr]	Calculated 2293 heat load (300 years of storage) (Watt) 1 Watt = [3.413 BTU/hr]
1A007	181.33	130.5	50.67	33	27.767
1A034	181.7	130.7	50.77	33	27.233
1A035	184.67	133.0	51.7	33.7	28.367
1A023	190.63	137.5	53.6	34.9	29.367
1A041	190.47	137.4	53.5	34.9	29.367
1A059	190.43	137.4	53.5	34.9	29.367
1A029	191.4	138.2	53.8	35.1	28.933
1A054	192.9	139.3	54.3	35.4	29.767
1B032	194.9	139.9	52.8	33.7	28.267
1B013	266.3	183.9	71.3	44.9	36.767
1B053	267.37	184.7	71.5	45.067	36.867
1B079	271.37	187.4	72.6	45.7	37.367
1B046	278.37	192.2	74.4	46.767	38.267
1B044	283.5	195.5	75.7	47.567	38.867
1B004	286.67	197.8	76.5	48.067	39.267
1B018	286.67	197.7	76.5	48	39.267
1B061	287	198	76.6	48.067	39.267
1B003	288.23	198.9	76.9	48.267	39.467
1C005	254.73	175.2	65.1	40.3	32.967
1C103	275.76	189.9	71.3	44.1	35.967
1C107	275.07	189.4	71.1	44	35.867
1C106	287.8	198.3	74.5	46.067	37.567
1C206	296.6	202.1	76.8	47.467	38.67
1C214	296.1	201.7	76.7	47.367	38.567

Table 4-2. Calculated decay heat load values at different years for HSM–15 module

Assembly ID	Calculated 1996 heat load (start of storage) (Watt) 1 Watt = [3.413 BTU/hr]	2012 heat load (current year of measurement) (Watt) 1 Watt = [3.413 BTU/hr]	Calculated 2097 heat load (101 years of storage) (Watt) 1 Watt = [3.413 BTU/hr]	Calculated 2197 heat load (201 years of storage) (Watt) 1 Watt = [3.413 BTU/hr]	Calculated 2297 heat load (301 years of storage) (Watt) 1 Watt = [3.413 BTU/hr]
2F177	346.1	272	83.83	50.46	40.75
2F136	367.3	291	89.09	53.52	43.04
1E 101	404.60	301	98.27	59.79	48.07
2F021	533.97	385	120.90	70.60	55.63
2F024	533.90	385	120.90	70.59	55.63
2F118	360.3	286	87.40	52.53	42.30
2F179	367.1	290	89.04	53.49	43.02
1H115	545.20	406	119.97	69.46	54.48
2G123	568.80	427	123.93	71.43	55.83
1H109	545.80	407	120.07	69.50	54.55
1G018	445.33	327	105.10	62.41	49.74
2F117	359.0	285	87.06	52.33	42.10
2F123	359.3	285	87.15	52.39	42.19
1G027	456.97	340	107.57	63.74	50.68
1H119	547.60	408	120.40	69.68	54.68
1H124	546.10	407	120.10	69.53	54.57
1E 102	404.50	301	98.24	59.77	48.06
1F119	302.93	232	78.96	49.44	40.34
2F166	347.9	272	84.92	51.28	41.38
1E 121	406.60	302	98.70	60.04	48.27
1E 120	406.27	302	98.62	59.99	48.23
1F110	291.93	225	76.11	47.71	39.05
2F125	345.4	274	83.70	50.37	40.65
1F113	294.97	225	77.45	48.67	39.86

The minimum and maximum temperatures decline over the 300 years of storage for all components (Figures 4-1 through 4-5). All components show a consistent trend, with a relatively rapid rate of temperature drop over the first 100 years and a more gradual rate of change thereafter. For example, the maximum cladding temperature decreases by approximately 129 K [232 °F] within the first 100 years and 28 K [50.4 °F] during the remaining 200 years of storage. This decline is driven by the change in decay heat load. The maximum component temperatures show much larger changes than the minimum component temperatures, which are relatively close to the ambient temperature throughout the storage period for all components except the cladding. Most of the minimum component temperatures decline by 10 K [18 °F] or less, reaching an asymptotic value only a few degrees above the ambient temperature partway through the storage period. Maximum component temperatures consistently drop with distance from the fuel rods (i.e., cladding to fuel sleeve to spacer plates to DSC shell to heat shield), as do the minimum temperatures, but at all times the temperature difference between components is much larger for the maximum temperature than the minimum temperature.

Figures 4-6 through 4-9 show the evolution of the temperature distribution in the airflow pathways and within the DSC along a transverse plane in HSM–1 for the same calendar years shown in Figures 4-1 through 4-5. The relative spatial temperature distribution remains consistent from century to century, but the most rapid decline occurs in the high temperature zone in the DSC. The peak temperature in the fuel region decreases from 370 to 320 K [207 to 116 °F] over the 300 years of storage, consistent with Figures 4-1 and 4-4, and the temperature change is greater in the first 100 years than the last 200 years of storage.

Figures 4-10 through 4-18 present the same simulated results for HSM–15 that are shown in Figures 4-1 through 4-9 for HSM–1. There is a similar pattern of temperature change in HSM–1 and HSM–15, except that the simulated temperatures for the HSM–15 module are higher than for HSM–1. Higher temperatures are expected in HSM–15 mainly because the decay heat load is nearly twice as large in HSM–15 (compare Tables 4-1 and 4-2). The corner position of HSM–1 in the module pattern exposes a side to atmospheric cooling, while HSM–15 is surrounded by other modules, but the effect of location is minor in comparison to the effect of the higher decay heat load.

Tables 4-3 and 4-4 present the calculated maximum and minimum cladding and DSC shell temperatures at periodic intervals for the HSM–1 and HSM–15 modules, respectively. These tables confirm that temperatures change most rapidly over the first 100 years of storage and then asymptotically converge to values only mildly above the ambient temperature of 301 K [82 °F].

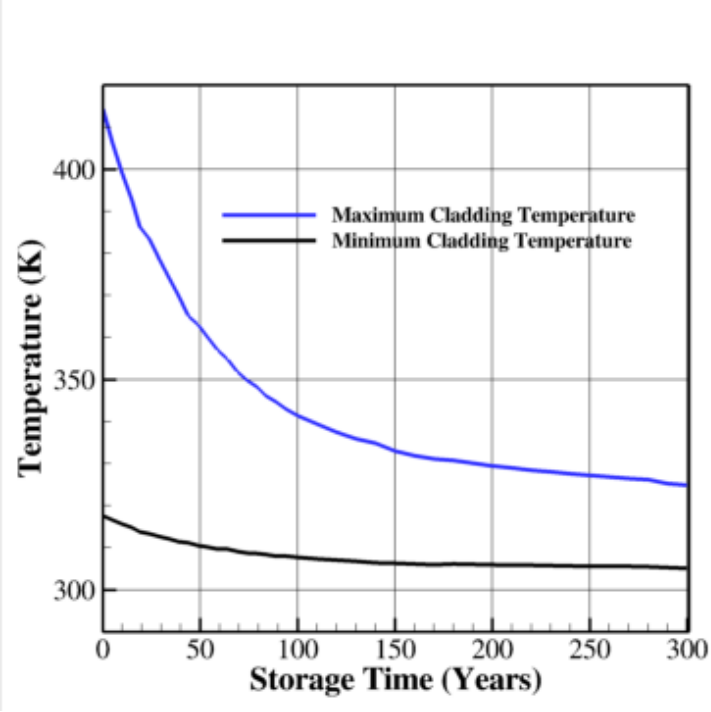

Figure 4-1. Variation of maximum and minimum cladding temperature over 300 years for HSM–1 module

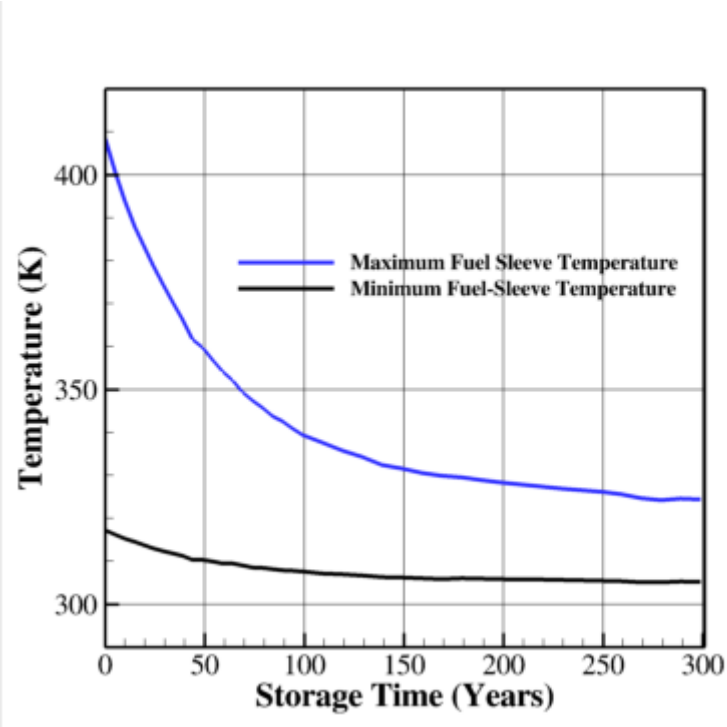

Figure 4-2. Variation of maximum and minimum fuel sleeve temperature over 300 years for HSM–1 module

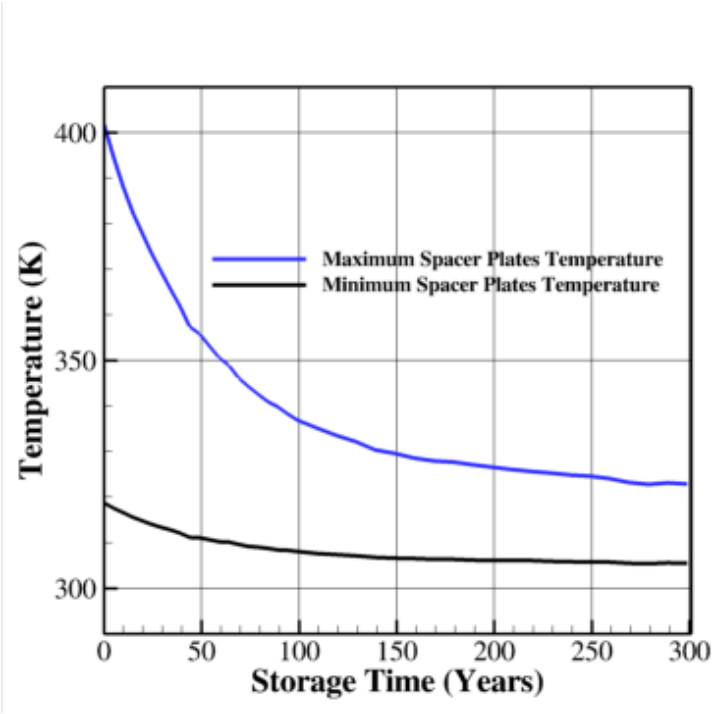

Figure 4-3. Variation of maximum and minimum spacer plates temperature over 300 years for HSM–1 module

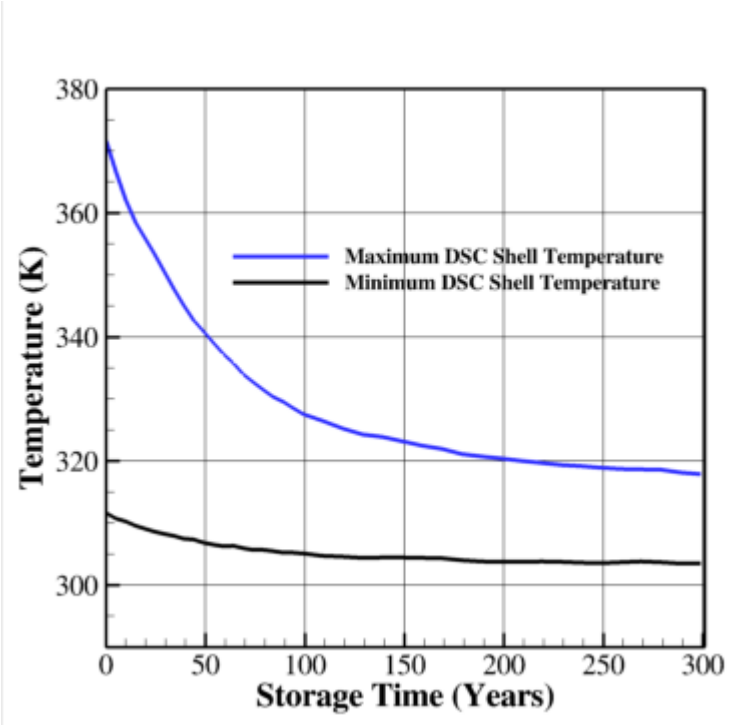

Figure 4-4. Variation of maximum and minimum DSC shell temperature over 300 years for HSM–1 module

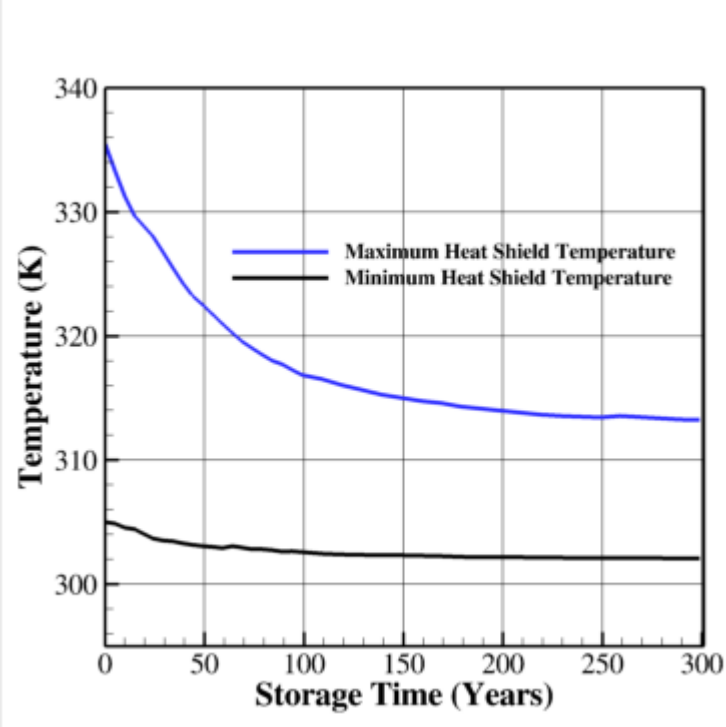

Figure 4-5. Variation of maximum and minimum heat shield temperature over 300 years for HSM–1 module

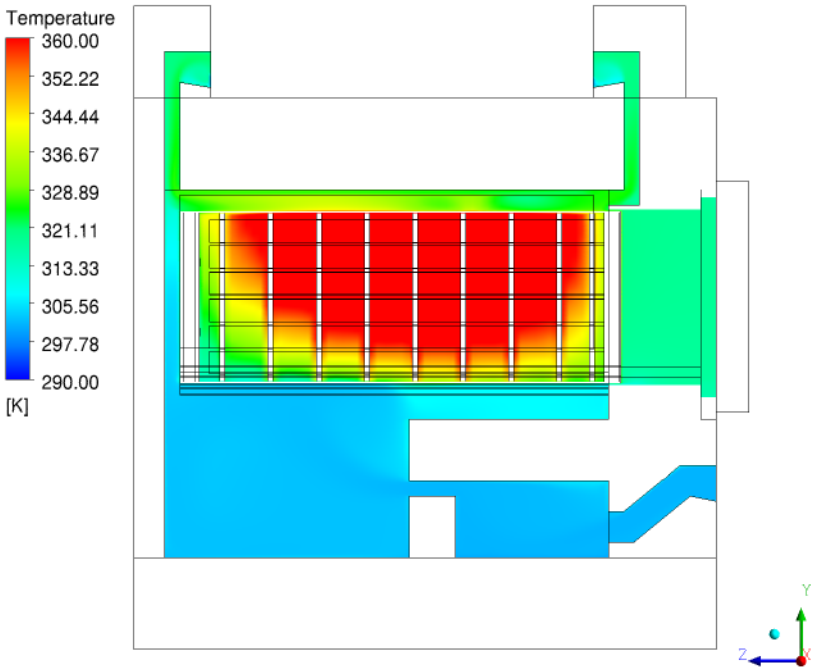

Figure 4-6. Air and helium temperature distributions at a transverse plane for HSM–1: year 1993

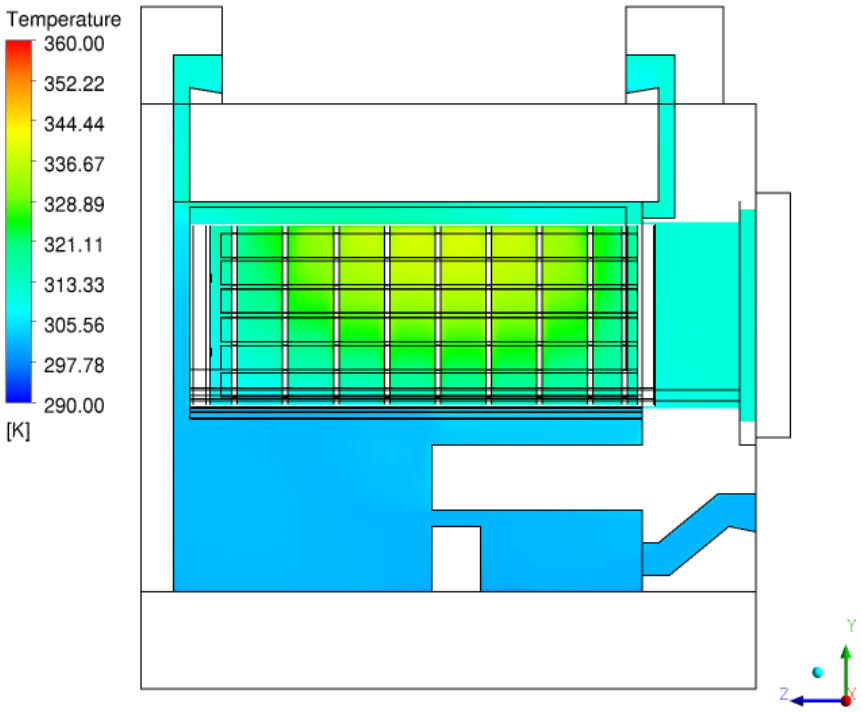

Figure 4-7. Air and helium temperature distributions at a transverse plane for HSM–1: year 2093 (100 years after storage)

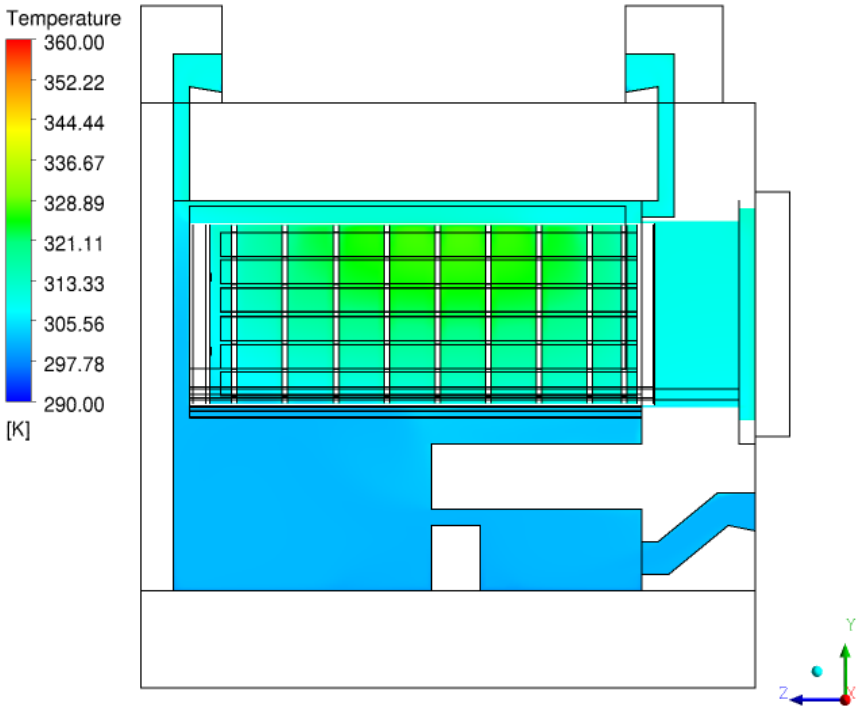

Figure 4-8. Air and helium temperature distributions at a transverse plane for HSM–1: year 2193 (200 years after storage)

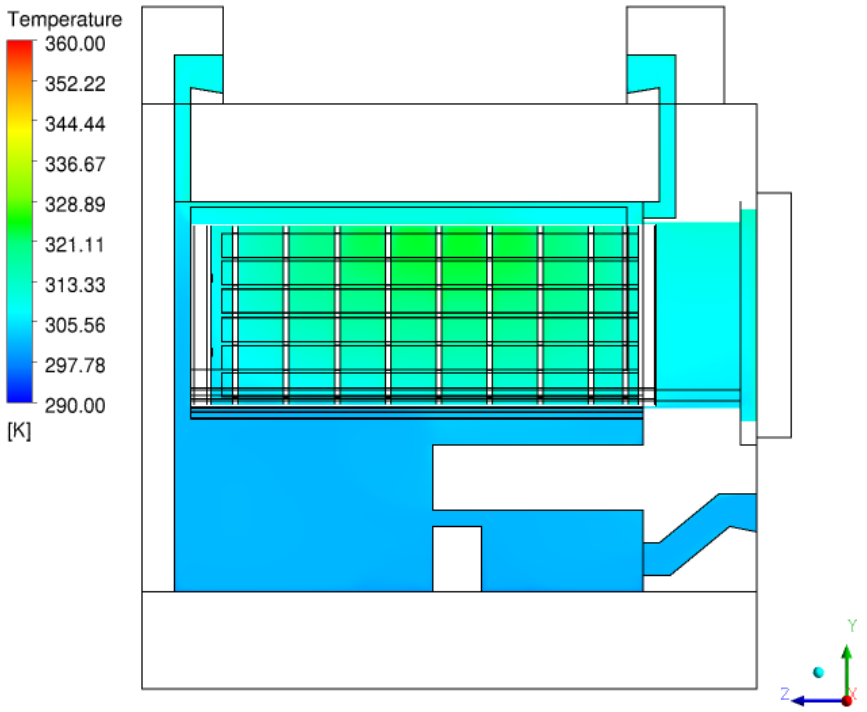

Figure 4-9. Air and helium temperature distributions at a transverse plane for HSM–1: year 2193 (300 years after storage)

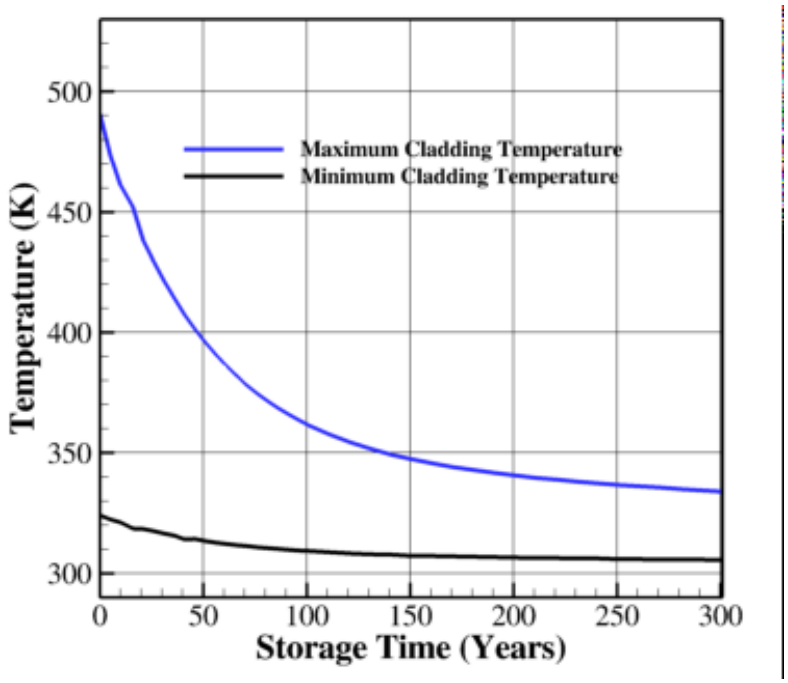

Figure 4-10. Variation of maximum and minimum cladding temperature over 301 years for HSM–15 module

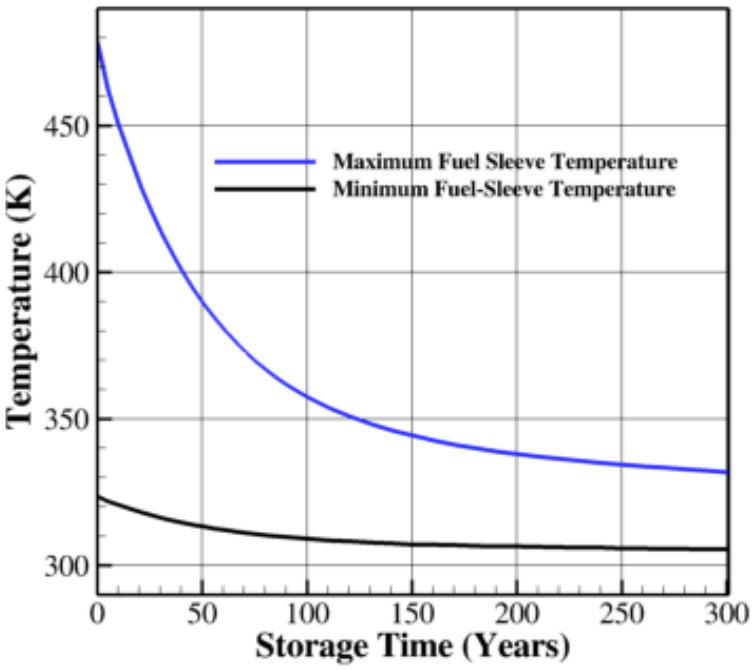

Figure 4-11. Variation of maximum and minimum fuel sleeve temperature over 301 years for HSM–15 module

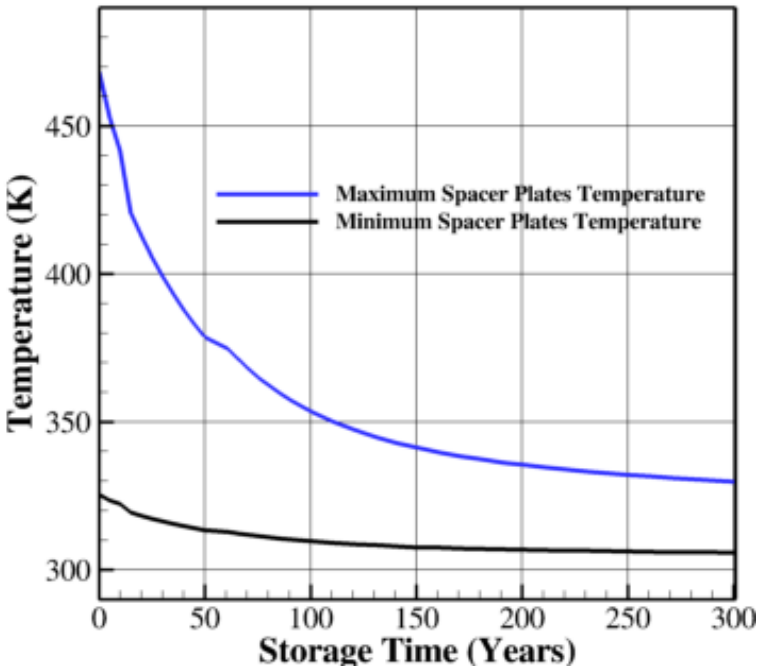

Figure 4-12. Variation of maximum and minimum spacer plate temperature over 301 years for HSM–15 module

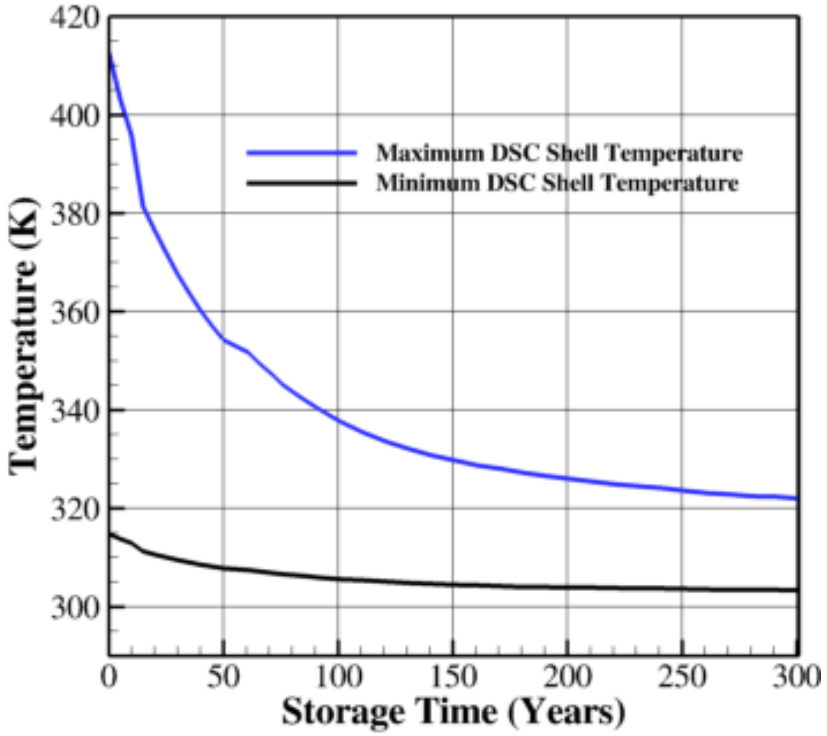

Figure 4-13. Variation of maximum and minimum DSC shell temperature over 301 years for HSM–15 module

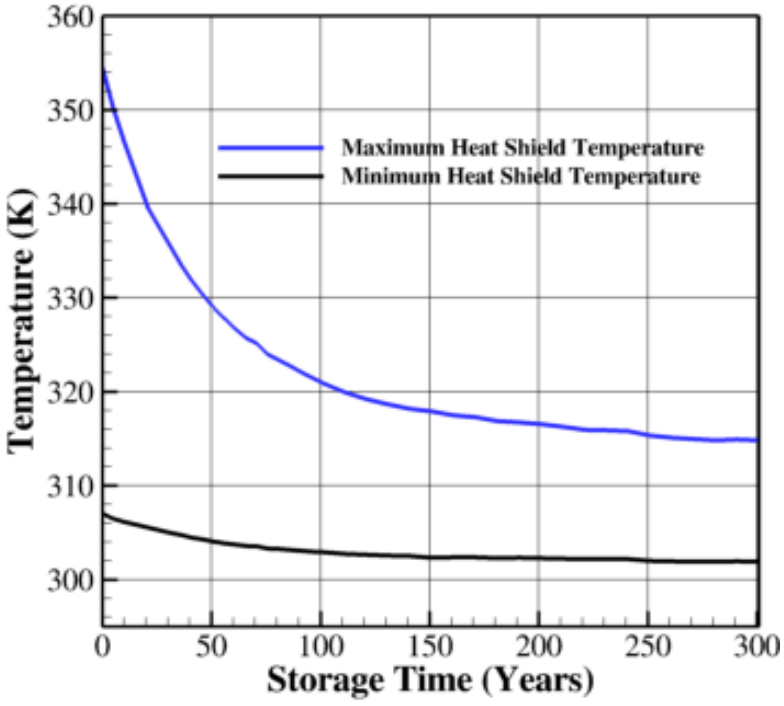

Figure 4-14. Variation of maximum and minimum heat shield temperature over 301 years for HSM–15 module

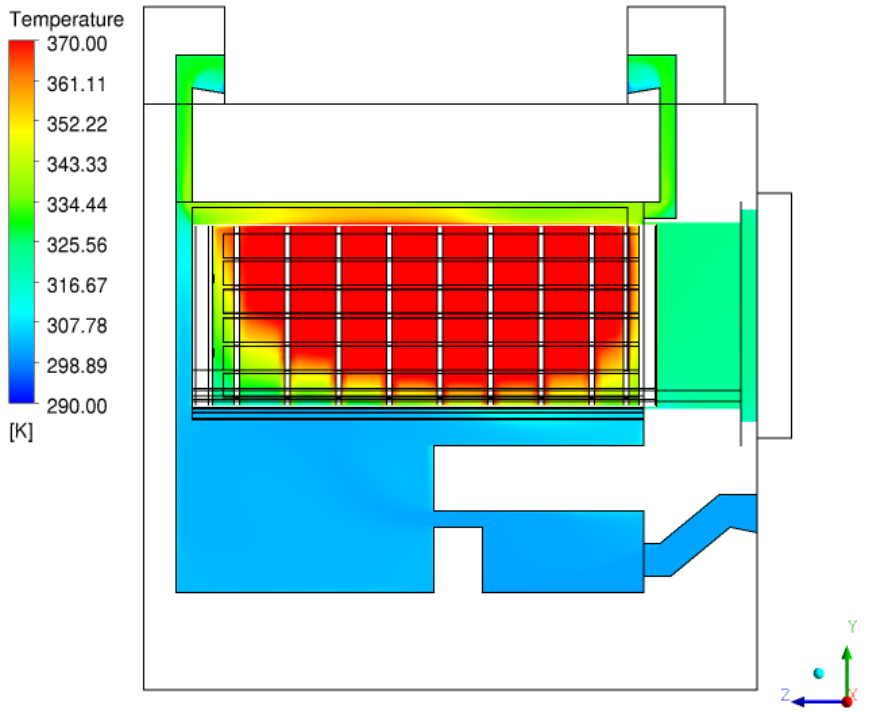

Figure 4-15. Air and helium temperature distributions at a transverse plane for HSM–15: year 1996

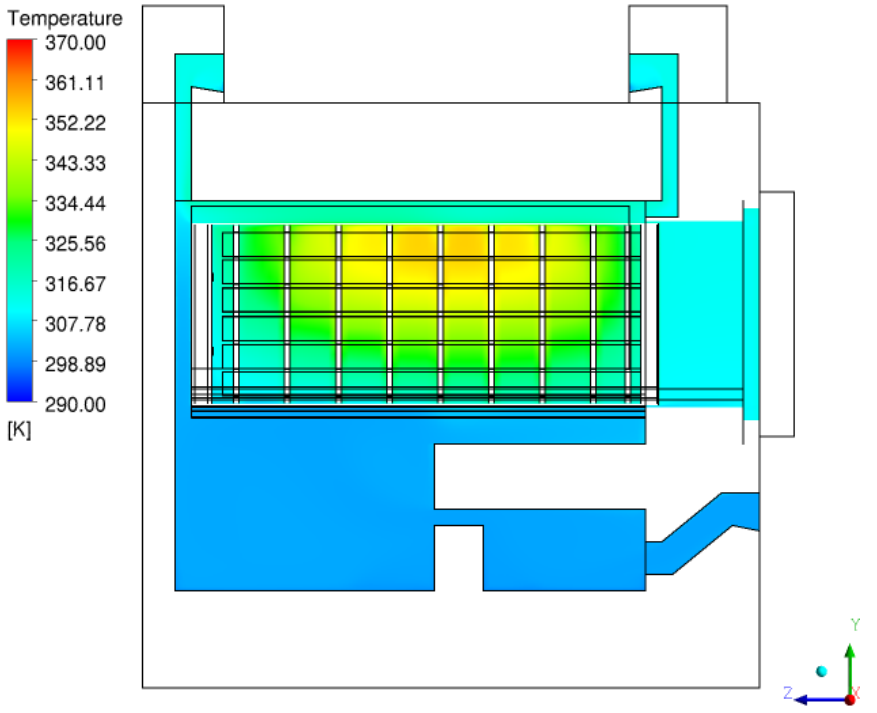

Figure 4-16. Air and helium temperature distributions at a transverse plane for HSM–15: year 2097 (101 years after storage)

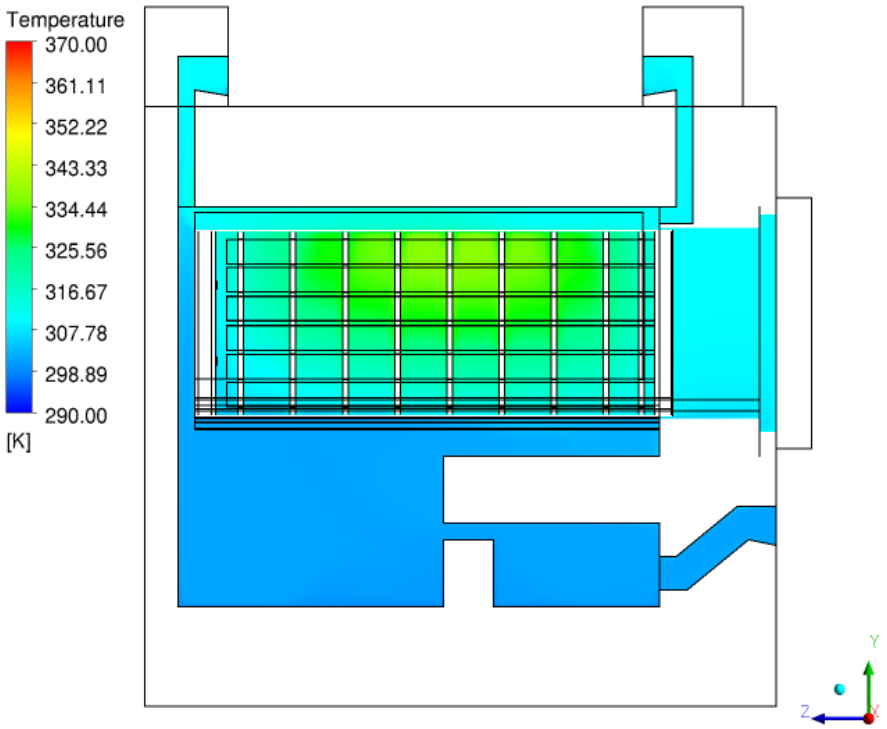

Figure 4-17. Air and helium temperature distributions at a transverse plane for HSM–15: year 2197 (201 years after storage)

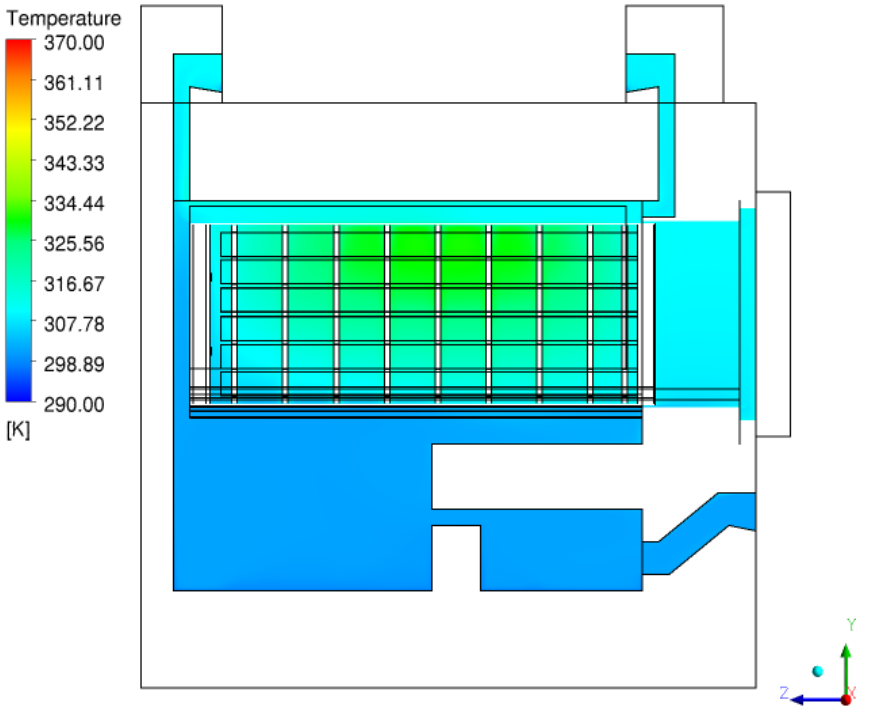

Figure 4-18. Air and helium temperature distributions at a transverse plane for HSM–15: year 2297 (301 years after storage)

Table 4-3. Calculated temperature values at different years for HSM–1 module

Year	Interval (years)	Maximum cladding temperature (K) °F = [1.8K-460]	Minimum cladding temperature (K) °F = [1.8 K-460]	Maximum DSC shell temperature (K) °F = [1.8 K-460]	Minimum DSC shell temperature (K) °F = [1.8 K-460]
1993	0	414.392	317.645	371.69	311.62
2012	19	386.316	313.742	354.01	308.81
2032	39	369.935	311.472	345.19	307.47
2052	59	357.009	309.686	337.28	306.29
2072	79	348.25	308.61	331.54	305.66
2093	100	341.366	307.719	327.55	305.09
2123	130	335.907	306.813	324.29	304.42
2153	160	331.841	306.121	322.51	304.36
2183	190	330.095	305.991	320.76	303.82
2213	220	328.467	305.812	319.67	303.77
2243	250	327.206	305.59	318.95	303.64
2273	280	326.179	305.489	318.57	303.57
2293	300	324.832	305.077	317.91	303.47

Table 4-4. Calculated temperature values at different years for HSM–15 module

Year	Interval (years)	Maximum cladding temperature (K)	Minimum cladding temperature (K)	Maximum DSC shell temperature (K)	Minimum DSC shell temperature (K)
1996	0	490.834	324.149	412.74	314.83
2017	21	438.218	318.443	381.41	311.27
2037	41	407.502	314.087	363.79	308.99
2057	61	386.23	312.261	351.66	307.45
2077	81	371.55	310.47	343.44	306.37
2097	101	361.442	309.194	337.65	305.61
2127	131	351.688	307.962	332.06	304.85
2157	161	345.589	307.183	328.74	304.35
2187	191	341.575	306.676	326.56	303.99
2217	221	338.803	306.288	324.86	303.79
2247	251	336.706	305.902	323.54	303.57
2277	281	335.008	305.66	322.43	303.42
2297	301	333.928	305.561	322.01	303.35

4.3 Observations from the Thermal Evolution Study

Detailed three-dimensional numerical simulations were performed to predict the thermal behavior of the HSM–1 and HSM–15 modules for 300 years of storage time. The analysis used steady-state simulations at multiple discrete time points, each corresponding to late June in a selected calendar year. The major observations from this study are the following:

- The simulations provided valuable insight into the time-dependent variation of maximum and minimum temperatures for cladding and internal components such as fuel sleeves, spacer plates, the DSC shell, and the heat shield. The general pattern of temperature change is similar for all the components, but the degree of variation is different for different components.

- Simulated results for both HSM–1 and HSM–15 show that the maximum temperature of any component drops substantially within the first 100 years of storage, with subsequent changes in temperature being more gradual.

- Simulated results highlight that the temporal variation of minimum component temperatures is small, approximately 10 K [18 °F].

- The general patterns of the temperature changes for HSM–1 and HSM–15 are similar. As with the baseline cases considered in Section 3, simulated temperatures for HSM–15 are uniformly higher than HSM–1 because of the larger decay heat load of the fuel contained in HSM–15 and the greater exposure of HSM–1 to the atmosphere.

5. UNCERTAINTY QUANTIFICATION AND GRID CONVERGENCE INDEX (GCI) ANALYSIS

The credibility and predictive capability of computational fluid dynamics (CFD) is greatly enhanced, and CFD can be considered a reliable tool for engineering analysis, if the numerical errors and uncertainties present in the solution can be reliably estimated [Phillips and Roy 2011; Rezende et al. 2012; Oberkampf and Roy 2010]. Error and uncertainty for a solver and a solution is formally estimated through a verification and validation (V&V) process. In 2009, the American Society of Mechanical Engineers (ASME) published a standard [ASME 2009] explaining the procedures for code verification, solution verification, and validation of CFD studies. The general objective of the V&V process is to estimate the accuracy of a numerical study.

Validation is the process used to determine whether a model accurately represents the physical phenomena of interest and to obtain an estimate of modeling uncertainty. This is primarily done by comparing simulated results with suitable experimental data. Verification deals with the uncertainty of the solution that can be attributed to numerical error, irrespective of how well the solution represents the actual physical process it models. A verification study consists of two components: code verification and solution verification. Code verification is used to demonstrate that the mathematical equations are correctly programmed. It ensures that the solver is free of any error due to coding and that the solution algorithm has been implemented correctly. In general, developers perform code verification based on evaluation of a known problem by the solver. In contrast, solution verification does not deal with the correctness of a code, but involves estimation of the numerical error or uncertainty for specific simulation results and is performed by users of a code. Discretization errors and iteration errors are the two main sources of numerical error. The solution verification process is also known as numerical error estimation [Celik et al. 2008].

This chapter presents the methodology and results from a numerical error estimation analysis performed for the dry cask thermal analysis described in previous chapters. The solution verification process described in ASME V&V 20-2009 [ASME 2009] was used to quantify numerical uncertainty for the calculated temperatures in horizontal storage modules HSM–1 and HSM–15. The uncertainty analysis was performed for solution verification with systematic grid refinement. For this study, two representative variables—maximum and minimum cladding temperature—were used to indicate solution behavior in addressing solution verification. These variables provide convergence criteria for numerical error estimation that are directly applicable to understanding the performance of the entire storage system. Although in principle the spatial location of these representative variables might shift from grid to grid, in practice the locations were observed to be essentially invariant. Therefore, the maximum and minimum cladding temperatures were used as representative parameters for numerical error estimation.

5.1 Uncertainty Analysis: Definitions and Concepts

The V&V process and concepts are briefly described in this section to facilitate the discussion of results, which follow.

5.1.1 Code Validation

The objective of code validation is to estimate (i) how accurately a model represents the physics of a problem and (ii) estimate the modeling error within a specified uncertainty range [ASME 2009]. Generally, this is achieved by comparing the result of a given simulation with an

experiment. Because code validation involves both numerical modeling results and experimental data, the source of uncertainty can be due to model inputs, numerical issues related to the model, or experimental uncertainty. As shown in ASME V&V 20-2009 [ASME 2009], if all these sources of errors are independent, then validation uncertainty can be defined as

$$u_{val} = \sqrt{u_{num}^2 + u_{input}^2 + u_{exp}^2} \qquad \text{Equation (5-1)}$$

where

u_{val} = Validation uncertainty
u_{num} = Numerical uncertainty
u_{input} = Input uncertainty
u_{exp} = Experimental uncertainty.

Numerical uncertainty contributes to the overall assessment of validation and is not the entire measure of the total uncertainty. Numerical uncertainty is estimated through verification (see Section 5.1.2). The present study considers numerical uncertainty without considering input or experimental uncertainty. To accurately measure the total uncertainty associated with a particular solution, all three components of validation uncertainty would need to be evaluated.

5.1.2 Code Verification

Code verification evaluates whether the mathematical formulation and constitutive relationship are correctly coded in the program. Code developers generally perform this exercise. One way of verifying that coding is correct is by simulating a problem that has an exact solution and evaluating whether the code reproduces the exact solution. Generally, code verification should precede solution verification to ensure that an error-free code is being used to obtain the solution of interest. In the present analysis, a commercial CFD package was used and therefore code verification was not performed.

5.1.3 Solution Verification

According to ASME V&V 20-2009 [ASME 2009], solution verification refers to the process of estimating the numerical uncertainty for a particular solution of a problem. The two main sources of errors that contribute to numerical uncertainty are the discretization error and the iteration convergence error. The discretization error is the difference between the result of a particular simulation with a specific grid and the results obtained with systematically refined grids. Discretization error can be estimated using a systematic grid refinement analysis, where the numerical solution is expected to asymptotically converge to the exact solution as the mesh size approaches zero. Systematic grid refinement forms the basis of the solution verification process.

Most CFD codes use iterative methods in which the numerical result must converge to the exact value as the iterations develop. Iteration convergence is related to the number of iterations required to obtain residuals that are sufficiently close to zero, either for a steady-state problem or for each time step in an unsteady problem. Iteration error is estimated using the residual root mean square (RMS) between subsequent iterations of a variable over all the volumes of the computational domain. In general, solutions are checked for iteration convergence by monitoring critical variables as solutions iteratively progress. It is necessary to achieve

complete iteration convergence before any discretization error estimate is performed because incomplete iteration convergence will adversely affect the estimate [Roache 1998, 1997, 1994].

Discretization error is normally calculated using Richardson extrapolation (RE) [Richardson 1910, Richardson and Gaunt 1927]. Richardson extrapolation is formulated to estimate the exact solution to the partial differential equations (PDEs) using the order of accuracy and solutions from two levels of grids. Richardson extrapolation is given by

$$\varphi_h = \varphi_{exact} + Ch^p \qquad \text{Equation (5-2)}$$

where

φ_h = Numerical solution
φ_{exact} = Exact solution to the PDEs
h = Grid size
C = Convergence coefficient
p = Order of accuracy

and the discretization error E_{dis} is given by

$$E_{dis} = \phi(h) - \phi_{exact} = Ch^p \qquad \text{Equation (5-3)}$$

Using Equation (5-3), it is possible to determine the discretization error using solutions from two grid levels if the order of accuracy is known. For most practical problems, however, the order of accuracy realized from the solution is not the same as the formal order of accuracy specified in the model and is not known in advance. Hence, solutions from at least three levels of mesh are needed to determine the actual order of accuracy, p, and the discretization error. Moreover, these grids have to be sufficiently fine such that the grid is in the asymptotic range to obtain a reliable value of p. It is difficult to generate grids in the asymptotic range for complex engineering problems. Researchers have found a number of disadvantages in directly using RE to calculate numerical uncertainty [Roache 1998]. Based on the concept of RE, Roache proposed a method for a numerical uncertainty estimate, known as the grid convergence index (GCI) method [Roache 1994, 2003, 1998; Pelletier and Roache 2006]. The GCI method was developed as a means of converting the discretization error estimates from the RE into uncertainties. The GCI is an estimated 95 percent uncertainty calculated by multiplying the absolute value of the RE error by a factor of safety (F_s) [ASME 2009]. GCI provides the uncertainty of the solutions derived from discretized equations by a numerical and an analytical approach. The GCI calculation formula is detailed in subsequent sections. The present study uses the GCI technique to estimate the numerical uncertainty for the temperature values calculated in HSM–1 and HSM–15.

5.2 Grid Convergence Index Calculation Method

This section describes the sequential steps needed to calculate GCI for three levels of grids. Celik et al. [2008] and ASME V&V 20-2009 [ASME 2009] described the procedure in detail. The procedure involves the following steps.

Step 1: Define a representative cell, mesh, or grid size h. It can be calculated as

$$h = \left[\left(\sum_{i=1}^{N} \Delta V_i \right) / N \right]^{1/3} \qquad \text{Equation (5-4)}$$

where

N = Total number of grids/cells used in the computations
ΔV_i = Volume of the i^{th} cell

Step 2: Generate three significantly different grids through systematic grid refinement. It is desirable that the mesh refinement factor (r), defined as h_{coarse}/h_{fine}, be greater than 1.3. The grid refinement should be done in a systematic way (i.e., the refinement itself should be structured even if the grid is unstructured). Once the grids have been generated, simulations should be run to determine the values of key variables important to the objective of the GCI analysis.

Step 3: For the three grids with representative cell sizes h_1, h_2, and h_3, with $h_1 < h_2 < h_3$, define the mesh refinement factors $r_{21} = h_2/h_1$, $r_{32} = h_3/h_2$ and calculate the apparent (or observed) order, p, of the method using the following three equations

$$p = \left[1/\ln(r_{21})\right]\left[\ln\left|\varepsilon_{32}/\varepsilon_{21}\right| + q(p)\right] \qquad \text{Equation (5-5)}$$

$$q(p) = \ln\left(\frac{r_{21}^{p} - s}{r_{32}^{p} - s}\right) \qquad \text{Equation (5-6)}$$

$$s = 1 \bullet \operatorname{sign}\left(\varepsilon_{32}/\varepsilon_{21}\right) \qquad \text{Equation (5-7)}$$

where $\varepsilon_{32} = \varphi_3 - \varphi_2$ $\varepsilon_{21} = \varphi_2 - \varphi_1$ and φ_k denotes the simulation value of the variable on the k^{th} grid level.

The parameter "s" in Equation (5-6) is the indicator of oscillatory convergence in the solution. When $s = 1$, the grid convergence under consideration is monotonic. When $s = -1$, the grid convergence is oscillatory. By considering "s" in Equation (5-6), one ensures that the calculation procedure provides GCI even if the grid convergence under consideration is oscillatory in nature.

Equations (5-5) through (5-7) can be solved using fixed point iteration with the initial guess equal to the first term (i.e., q = 0) [ASME 2009].

Step 4: Calculate the extrapolated values from the following equations

$$\phi_{ext}^{21} = \left(r_{21}^{p}\phi_1 - \phi_2\right)/\left(r_{21}^{p} - 1\right) \qquad \text{Equation (5-8)}$$

$$\phi_{ext}^{32} = \left(r_{32}^{p}\phi_2 - \phi_3\right)/\left(r_{32}^{p} - 1\right) \qquad \text{Equation (5-9)}$$

Step 5: Calculate the following error estimates along with the observed order of the method p.
Approximate relative error:

$$e_a^{32} = \left| \frac{\phi_2 - \phi_3}{\phi_2} \right| \quad \text{Equation (5-10)}$$

$$e_a^{21} = \left| \frac{\phi_1 - \phi_2}{\phi_1} \right| \quad \text{Equation (5-11)}$$

Extrapolated relative error:

$$e_{ext}^{21} = \left| \frac{\phi_{ext}^{12} - \phi_1}{\phi_{ext}^{12}} \right| \quad \text{Equation (5-12)}$$

The fine grid convergence index is calculated as

$$GCI_{fine}^{21} = \frac{F_s \bullet e_a^{21}}{r_{21}^p - 1} \quad \text{Equation (5-13)}$$

In the previous expression, F_s is the factor of safety that is introduced to ensure a GCI with a 95 percent confidence interval. Originally, F_s was assigned a value of 3 for two-grid studies [Roache 1994], but Roache [1998] recommended a less conservative value of 1.25 for cases using at least three grid solutions and the observed p. According to ASME V&V 20-2009 [ASME 2009], a value of 1.25 should be used for F_s with three-grid studies involving structured grid refinement.

Celik et al. [2008] modified Equation (5-5) in their GCI formula, given by

$$p = \left[1/\ln(r_{21})\right]\left[\left|\ln\left|\varepsilon_{32}/\varepsilon_{21}\right| + q(p)\right|\right] \quad \text{Equation (5-14)}$$

According to Celik and Karatekin [1997], the absolute value of $\varepsilon_{32}/\varepsilon_{31}$ is necessary to ensure extrapolation toward $h = 0.0$. Negative values of $\varepsilon_{32}/\varepsilon_{31} < 0.0$ indicate oscillatory convergence.

5.3 Uncertainty Quantification and GCI Analysis for HSM–1 Module

Solution verification for both HSM–1 and HSM–15 modules was performed using four levels of mesh generated with systematic grid refinement. Simulations were performed using all four levels of mesh at three specific time points, which are calendar years 1993, 2012, and 2093. The objective of this analysis was to determine the numerical uncertainty due to discretization error based on the GCI technique with a 95 percent confidence interval containing the exact solution of the problem and system of equations. Simulations were performed for three calendar years to assess the variation of the apparent order p and GCI values with decreasing thermal load. The levels of grids used in the analysis for the HSM–1 module are provided in Table 5-1, which also lists the mesh refinement factor between two consecutive levels of grids calculated using the procedure described in Step 1 and Step 2 in Section 5-2. For example, the mesh refinement factor r for the baseline mesh is calculated using the grid sizes of the baseline and coarse meshes. Simulation for all the levels of grids was performed with the same input

parameters and the same turbulence model that was used for the baseline simulations for the HSM–1 module described in Chapter 2 of this report.

Table 5-1. Mesh levels used in GCI analysis of HSM–1 module

Mesh type	Total cell number	Mesh refinement factor (r)
Coarse mesh	1,220,596	
Baseline mesh	3,528,864	1.4245
Fine mesh 1	9,214,367	1.3771
Fine mesh 2	25,000,000	1.3856

Figure 5-1 shows temperature contours along the transverse mid-plane for the four mesh levels for HSM–1 simulations at the representative year 1993. It can be observed that there is no significant qualitative difference in the simulated results from the four mesh levels, indicating that mesh refinement does not cause any major deviation in the simulated temperature field. However, temperature contours show that the finest mesh calculation captures the thermal gradient better compared to the coarse mesh and baseline mesh simulations.

Tables 5-2, 5-3, and 5-4 provide the simulated values of the maximum and minimum cladding temperatures for the HSM–1 module for years 1993, 2012, and 2093, respectively, for all four mesh levels. There are only minor differences in the predicted values of the maximum and minimum cladding temperatures from the different grid levels for the HSM–1 module. The maximum temperature difference between the coarse mesh solution and the finest mesh solution is approximately 3 K [5.4 °F] and in most of the cases the variation is less than 1 K [1.8 °F]. Also note that the variation decreases with increased storage time.

To better understand the variability of predicted temperature values, the percentage of variation of the maximum and minimum cladding temperatures with mesh size is plotted in Figure 5-2 for the different grid levels for the HSM–1 module. The percentage of variation is calculated using the following relationship

$$\text{Variation } (\Delta V) = \left(\frac{T - T_{\text{finest-mesh}}}{T_{\text{finest-mesh}}}\right) \times 100 \qquad \text{Equation (5-15)}$$

The x-axis in Figure 5-2 shows the nondimensionalized mesh size ($h/h_{\text{fine-mesh-2}}$), where h is the representative grid size as defined in Step 1 and $h_{\text{fine-mesh-2}}$ is the corresponding grid size for the fine mesh 2 case. Hence, a nondimensional mesh size of 1 corresponds to the finest mesh (fine mesh 2), with higher values for coarser meshes. The calculated deviation is shown along the y-axis. Note that the variation between the solutions from different grid levels is within 1 percent.

The apparent order and the GCI values are calculated for the variables maximum and minimum cladding temperatures. Equation (5-13) was used to calculate the GCI using the modified apparent order p described in Equation (5-14). For the GCI calculations, the factor of safety F_s is taken as 3.0. The values for p and the GCI values for the HSM–1 modules are provided in Table 5-5. The GCI values listed in the table were calculated based on the baseline and two fine-mesh-level solutions.

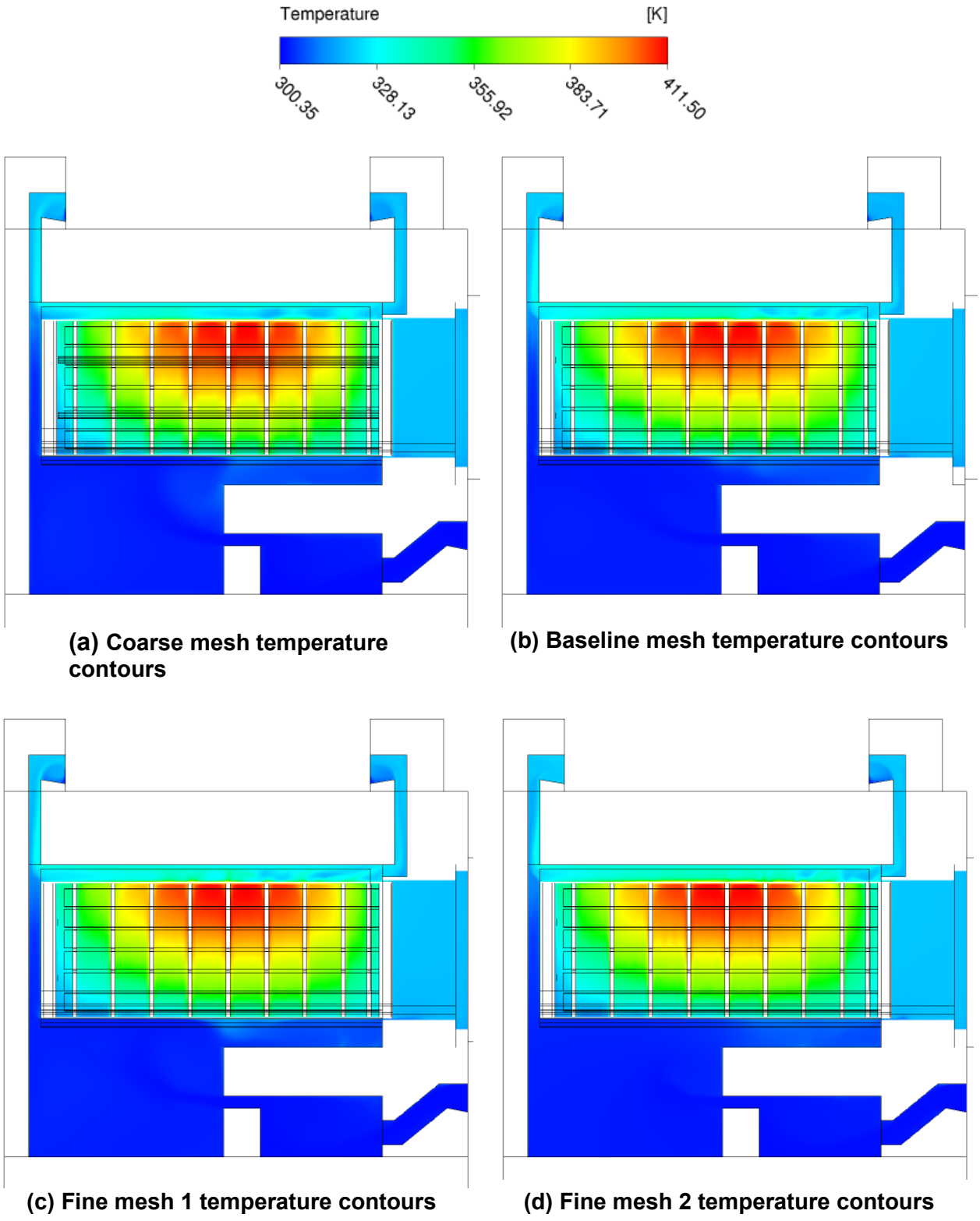

(a) Coarse mesh temperature contours

(b) Baseline mesh temperature contours

(c) Fine mesh 1 temperature contours

(d) Fine mesh 2 temperature contours

Figure 5-1. Temperature contours along the mid-plane for four mesh levels for simulations of HSM–1 at year 1993

Table 5-2. Computed maximum and minimum cladding temperature for HSM–1 module (1993)

Mesh type	Maximum cladding temperature (K) °F = [1.8 K-460]	Minimum cladding temperature (K) °F = [1.8 K-460]
Coarse mesh	421.661	319.41
Baseline mesh	420.363	318.299
Fine mesh 1	421.518	317.69
Fine mesh 2	419.399	316.38

Table 5-3. Computed maximum and minimum cladding temperature for HSM–1 module (2012)

Mesh type	Maximum cladding temperature (K) °F = [1.8 K-460]	Minimum cladding temperature (K) °F = [1.8 K-460]
Coarse mesh	392.017	315.595
Baseline mesh	390.82	314.07
Fine mesh 1	391.676	314.442
Fine mesh 2	390.963	313.577

Table 5-4. Computed maximum and minimum cladding temperature for HSM-1 module (2093)

Mesh type	Maximum cladding temperature (K) °F = [1.8 K-460]	Minimum cladding temperature (K) °F = [1.8 K-460]
Coarse mesh	343.209	308.437
Baseline mesh	342.786	307.659
Fine mesh 1	342.954	307.539
Fine mesh 2	342.537	307.254

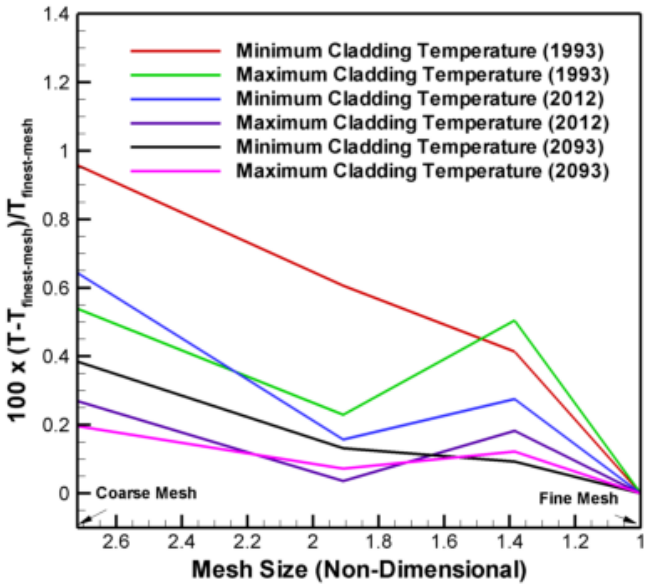

Figure 5-2. Deviation of temperature values calculated at different mesh levels for HSM–1: deviations are calculated as percentage of fine mesh temperatures

Table 5-5. Apparent order (p) and calculated GCI for HSM–1 module

Year	Variable	Apparent order (p)	GCI
1993	Maximum cladding temperature	1.83	1.85
	Minimum cladding Temperature	2.26	1.14
2012	Maximum cladding temperature	0.56	2.67
	Minimum cladding Temperature	2.55	0.84
2093	Maximum cladding temperature	2.75	0.25
	Minimum cladding Temperature	2.56	0.21

The values of p and GCI provide an evaluation of numerical uncertainty in the simulations. The values of GCI (less than 4 percent in most of the cases) in Table 5-5 indicate that there was no significant deviation of the calculated results due to mesh refinement or mesh convergence, further strengthening the observations made in Figures 5-1 and 5-2. For all the simulations, the spatial discretization used was second-order accurate. It can be observed from Table 5-5 that the apparent order of accuracy is not constant and is, in most of the cases, higher than the theoretical order of accuracy (p = 2).

Figure 5-3 shows the variation of calculated p values for the maximum and minimum cladding temperatures at the three calendar years plotted against the nondimensional mesh size ($h/h_{fine\text{-}mesh\text{-}2}$). The apparent order at a mesh point was calculated using a combination of three temperatures. The following combinations were used for the apparent order calculations:

(i) Coarse, baseline, and fine mesh 1 solutions (mesh set 1).

(ii) Coarse, fine mesh 1, and fine mesh 2 solutions (mesh set 2).

(iii) Baseline, fine mesh 1, and fine mesh 2 solutions (mesh set 3).

It is possible to have other combinations of solutions, but these three sets provide representative values as they generally consider progressively refined meshes. The purpose of this plot (Figure 5-3) was to understand the general variability of p with mesh refinement. From the figure, it is clear that the calculated value of p varies significantly for different levels of mesh refinement.

From Figure 5-3 it can also be observed that the calculated values of p are significantly higher in many cases. The theoretical value of p is shown by the red dotted line in Figure 5-3. The dispersivity of the calculated p values is significant for the current simulations. According to Roache [1998], the general disagreement of the calculated p-value and the theoretical p-value is not necessarily a sign that the simulated values or simulations are wrong and unsatisfactory; however, further analysis was performed to understand this behavior.

5.3.1 Assessment of Asymptotic Behavior of the Solution

To find a probable explanation for this behavior, two quantities were calculated and their variations with mesh size were analyzed. The first quantity under consideration is the discretization error that is defined in Equation (5-3).

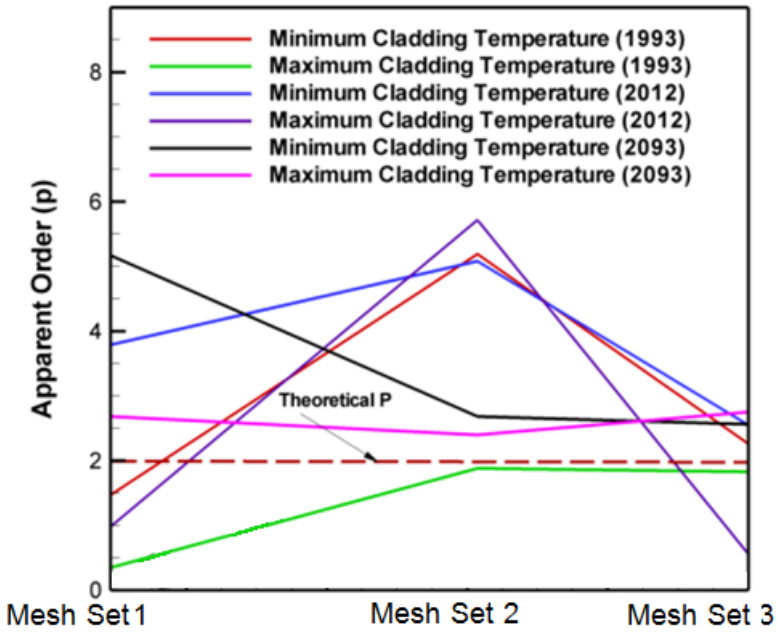

Figure 5-3. Calculated apparent order using different mesh levels for HSM–1

Using Equation (5-3), the convergence coefficient can be defined as

$$C = E_{dis}/h^p \qquad \text{Equation (5-16)}$$

As described in ASME V&V 20-2009 [ASME 2009], for a well-behaved problem the values of the convergence coefficient c should become constant as the grid is refined for a uniformly p^{th} order method. Hence, the slope of the E_{dis} distribution against h should be continuous and constant.

An exact analytical solution for the dry cask thermal problem, however, is not known; according to Roache [2003], the extrapolated solution can be used to calculate the discretization error when the exact solution is not known. In the present study, the discretization error is computed using the extrapolated values obtained from two different solutions using Equation (5-17).

$$\phi_{ext} = \frac{r_{21}^{\,p}\phi_1 - \phi_2}{r_{21}^{\,p} - 1} \qquad \text{Equation (5-17)}$$

For the present study, therefore, the discretization error is calculated using Equations (5-3) and (5-17). From these equations, it is clear that to calculate the discretization error, three sets of solutions are needed.

Figure 5-4 shows the variation of the discretization error with nondimensional mesh size (1 corresponds to finest mesh) at three calendar years (1993, 2012, and 2093). The discretization error at every point was calculated using a set of three solutions. The same combination of solutions described in connection with Figure 5-3 was used to determine discretization errors for Figure 5-4. Note that the curves do not exhibit asymptotic behavior and have sharp discontinuities. To further illustrate the nonasymptotic nature of the discretization

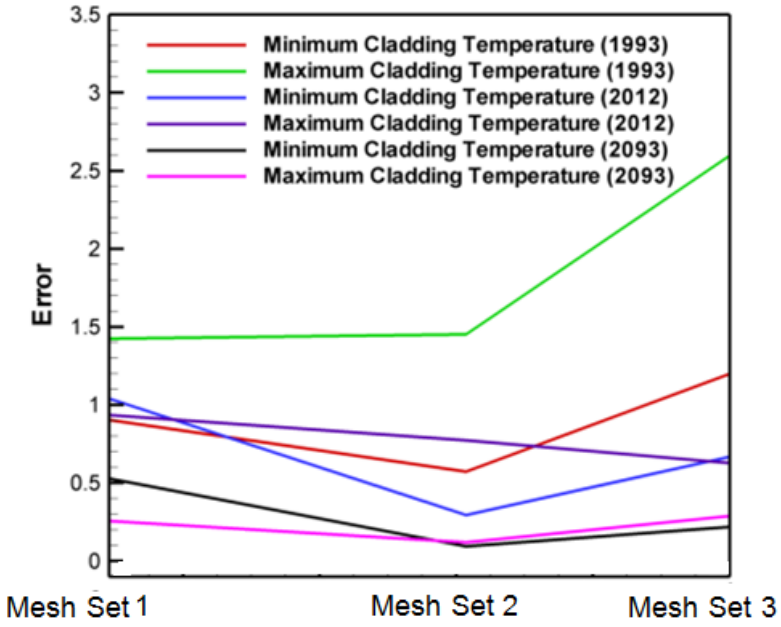

Figure 5-4. Distribution of discretization error with mesh refinement for HSM–1

error and the solution, the variation of the convergence coefficient [C in Equation (5-16)] due to mesh refinement is shown in Figure 5-5. The convergence coefficients were calculated using the same combination of mesh and solutions that were used to determine discretization errors for Figure 5-4. If the solutions are within the asymptotic region, then the convergence coefficient C [slope of Equation (5-3)] should be a constant for all mesh sizes. However, one can see that the variation of C doesn't follow any general pattern. The value of C varies significantly, which indicates oscillatory convergence. Figures 5-4 and 5-5 suggest that the solutions obtained from the systematic mesh convergence study may not all lie in the asymptotic convergence region.

5.3.2 Iteration Convergence

As indicated in Section 5.1.3, one of the important factors in numerical uncertainty estimation calculation is iteration convergence. The possibility of incomplete iteration convergence was explored for the present study. Figure 5-6 shows the variation of the average temperature of selected monitor points with iteration for the baseline case at calendar year 2012. The plot shows an overall convergence with iteration, and the trend indicates that the solution is converged. Figure 5-7 highlights the convergence pattern for the last 6,000 iterations as function of temperature and indicates some minor oscillations. Although one can conclude from Figure 5-6 that the solution has an overall convergence, Figure 5-7 shows that some minor oscillations may still persist. Hence, the calculation of p and GCI essentially depends on the iteration at which the solution was terminated.

5.3.3 Other Numerical Issues

It is clear from Tables 5-2, 5-3, and 5-4 that the calculated temperature values do not change significantly due to mesh refinement and, generally the variation is less than 1K [1.8 ^{0}F]. Essentially, these differences can be attributed to numerical noise and machine error. Because

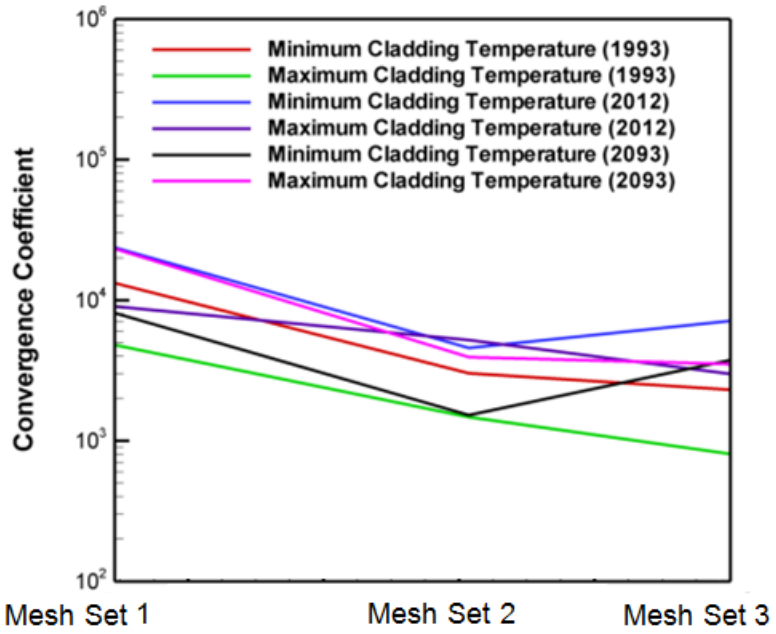

Figure 5-5. Variation of convergence coefficient with mesh refinement for HSM–1

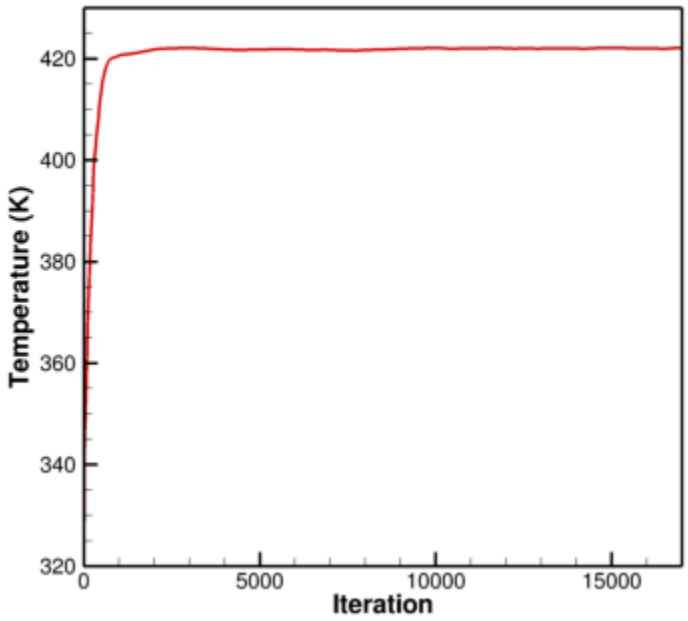

Figure 5-6. Variation of average temperature of selected monitor points with iteration, showing overall convergence for HSM-1

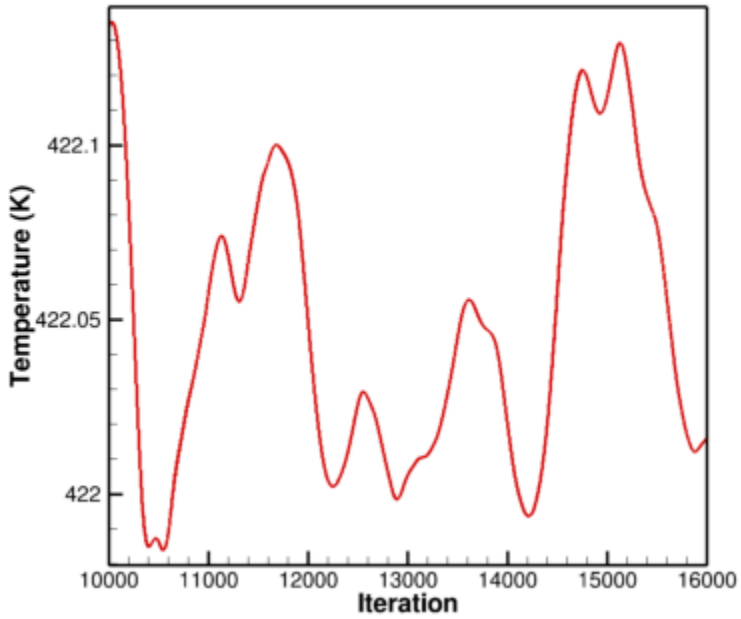

Figure 5-7. Variation of average temperature of selected monitor points with iteration for last 6,000 iterations, highlighting minor oscillations for HSM-1

the values predicted by different mesh levels are very close to each other, such minor oscillations tend to affect some of the terms in Equations 5-8 through 5-14 disproportionally and subsequently affect the calculation of apparent order p and GCI values.

According to Roache [1998], it is difficult to have complete iteration convergence in multiphysics problems with multiple scales of solution and multiple scales in turbulence modeling because different parts of the physics may converge differently. Roache [1998, 1997] indicates that, in multiphysics problems, a grid may be in the asymptotic range for some flow physics, but not in the asymptotic range for other physics. This behavior can be more prominent in problems that involve the laminar to turbulent transition. The present problem involves flow that may be in the transition region, which contributes to the uncertainty. In addition, the present problem involves a complicated geometry that influences the flow path and causes repeated flow separations and reattachments that are difficult to model accurately [Roache 1997]. Additionally, an asymptotic solution requires a systematic mesh refinement in all three coordinate directions. In the present study, an attempt has been made to achieve a systematic mesh refinement in all directions with the same mesh refinement factor. However, due to the complexity of the geometry and certain limitations of the grid generation package, the mesh refinement factor had to be adjusted in small parts of the domain—especially in narrow gaps and annuli. Therefore, the complexity of the flow physics and limitations in mesh refinement may have resulted in nonasymptotic solutions. However, the closeness of the calculated temperature values showed that mesh refinement may have had little impact on the solution.

5.3.4 Modified Estimation of GCI for HSM-1

To obtain a useful bound on the simulated results and a realistic numerical uncertainty estimate, a modified approach to calculate GCI was used. In this approach, a theoretical order of accuracy p=1 was used instead of the apparent order of accuracy. This is because the simulations involved specification of mixed order methods, whereby the spatial discretization was performed using a second order scheme and the body force averaging in the pressure equations was performed using a first order method. In addition, the radiative transport equations in the radiation discrete ordinate model were solved using a first order method. Therefore, the overall solution would be contaminated by these first order approximations and not be second order accurate. Hence, the theoretical order of accuracy for the GCI calculation was assumed to be 1.

The general objective of the GCI calculations described in this chapter was to provide an idea of the numerical uncertainty associated with the benchmark modeling (Chapter 3) and the thermal evolution study over 300 years (Chapter 4). As these studies were performed using the baseline mesh, it was imperative to use the baseline mesh results for the GCI calculations. Therefore, Equations (5-11) and (5-13) were used to calculate the GCI with p=1. The mesh refinement factor r_{21} and the relative error term e_a^{21} were calculated based on baseline and coarse mesh simulations. The calculated values of GCI for HSM-1 using this approach are provided in Table 5-6.

The calculated GCI values are greater for this bounded case compared to the values provided in Table 5-5 but are still low, indicating the minor influence of mesh refinement.

5.4 Uncertainty Quantification and GCI Analysis for HSM–15 Module

The methodology used to perform uncertainty quantification and GCI calculation for HSM-1 was applied also to HSM-15. The four levels of meshes used in the analysis for HSM–15 and the mesh refinement factors are provided in Table 5-7. The mesh refinement factors were calculated using steps 1 and 2 described in Section 5-2 using two consecutive levels of meshes. All four levels of meshes were simulated with the same input parameters and the same turbulence model that were used for the baseline simulations for the HSM–15 module. As for HSM-1, simulations for HSM-15 at every mesh level were performed at three different calendar years, which are years 1996, 2012, and 2097.

Tables 5-8, 5-9, and 5-10 provide the simulated values of the maximum and minimum cladding temperatures for the HSM–15 module for years 1996, 2012, and 2097, respectively. One can generally observe that, similar to the case for the HSM–1 module, there are only minor differences in the predicted values of the maximum and minimum cladding temperatures for the different grid levels for the HSM–15 module. The largest temperature difference between the coarse and fine mesh solutions, observed for the minimum cladding temperature at year 2012, is less than 3 K [5.4 °F]. In most of the cases the difference is less than 1 K [1.8 °F]. As pointed out in Sections 5.3.2 and 5.3.3, these minor differences could be artifacts of machine round-off errors and oscillatory iteration convergence. Figure 5-8 shows the percentage variation of the maximum and minimum cladding temperatures calculated using Equation (5-15) between solutions for the different grid levels for HSM–15. As can be observed, there is insignificant variation of less than 1 percent between the solutions with the different grid levels. While the variability decreases with mesh refinement, the close similarity of computed results shows that the effect of mesh refinement was not significant.

Table 5-6. GCI value for a conservative bounded value of p = 1 for HSM–15 module

Year	Variable	Value from baseline mesh simulation (K) °F = [1.8 K-460]	GCI
1993	Maximum Cladding temperature	420.363	2.181
	Minimum Cladding Temperature	318.299	2.466
2012	Maximum Cladding temperature	390.82	2.16
	Minimum Cladding Temperature	314.07	3.43
2093	Maximum Cladding temperature	342.786	0.872
	Minimum Cladding Temperature	307.659	0.178

Table 5-7. Mesh levels used in GCI analysis of HSM–15 module

Mesh Type	Total cell number	Mesh refinement factor (r)
Coarse mesh	1,136,626	
Baseline mesh	3,278,964	1.4235
Fine mesh 1	9,000,000	1.3744
Fine mesh 2	22,635,832	1.3853

Table 5-8. Computed maximum and minimum cladding temperature for HSM–15 module (1996)

Mesh type	Maximum cladding temperature (K) °F = [1.8 K-460]	Minimum cladding temperature (K) °F = [1.8 K-460]
Coarse mesh	502.23	327.56
Baseline mesh	502.61	326.49
Fine mesh 1	503.04	325.19
Fine mesh 2	502.4	324.96

Table 5-9. Computed maximum and minimum cladding temperature for HSM–15 module (2012)

Mesh type	Maximum cladding temperature (K) °F = [1.8 K-460]	Minimum cladding temperature (K) °F = [1.8 K-460]
Coarse mesh	463.13	323.29
Baseline mesh	462.83	321.66
Fine mesh 1	462.21	321.40
Fine mesh 2	461.63	320.50

Table 5-10. Computed maximum and minimum cladding temperature for HSM–15 module (2097)

Mesh type	Maximum cladding temperature (K) °F = [1.8 K-460]	Minimum cladding temperature (K) °F = [1.8 K-460]
Coarse mesh	364.77	310.22
Baseline mesh	364.70	309.21
Fine mesh 1	364.20	309.56
Fine mesh 2	364.08	308.87

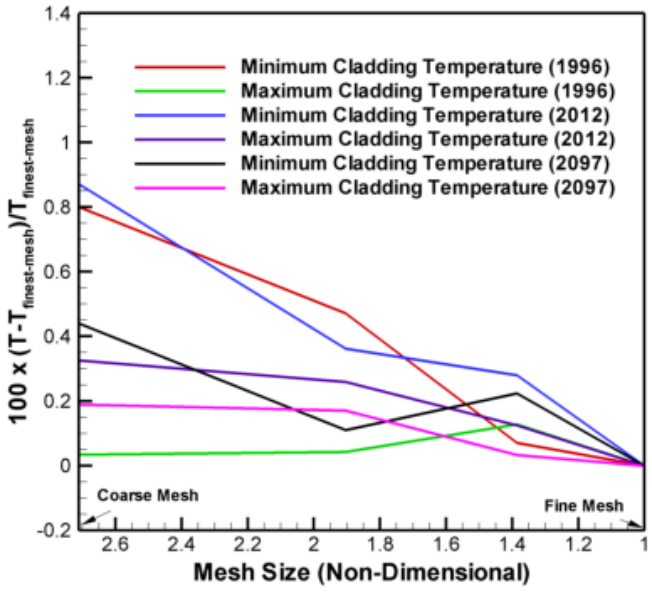

Figure 5-8. Deviation of temperature values calculated at different mesh levels for HSM–15: deviations are calculated as percentage of fine mesh temperatures

The values for apparent order p and GCI for HSM–15, calculated using the baseline, fine mesh 1, and fine mesh 2 solutions, are provided in Table 5-11. The values of calculated GCI indicate again that the variability between the solutions obtained at different mesh levels. As observed in connection with HSM-1, the apparent order of accuracy p for HSM-15 is not constant and some of the calculated values are higher than the theoretical order of accuracy. Figure 5-9 shows the calculated p values for the maximum and minimum cladding temperatures at the three calendar years for HSM-15. As was the case for HSM-1, the apparent order at a mesh point was calculated using a combination of three temperatures. The following combinations were used for the apparent order calculations:

(i) Coarse, baseline, and fine mesh 1 solutions (mesh set 1).

(ii) Coarse, fine mesh 1, and fine mesh 2 solutions(mesh set 2).

(iii) Baseline, fine mesh 1, and fine mesh 2 solutions (mesh set 3).

The general objective of this plot was to determine whether the value of p remains constant and lies in the asymptotic region. The figure indicates that p is not constant and varies significantly.

Further analysis was performed to understand solution behavior variation with mesh refinement. Figure 5-10 shows the distribution of the discretization error for different mesh sizes for HSM–15 at three calendar years. The discretization error was computed using Equation (5-3) and the

Table 5-11. Apparent order (p) and calculated GCI for HSM–15 module

Year	Variable	Apparent order	GCI
1996	Maximum cladding temperature	1.2	0.79
	Minimum cladding temperature	5.48	0.04
2012	Maximum cladding temperature	1.94	0.423
	Minimum cladding temperature	3.6	0.37
2097	Maximum cladding temperature	4.5	0.03
	Minimum cladding temperature	2.05	0.70

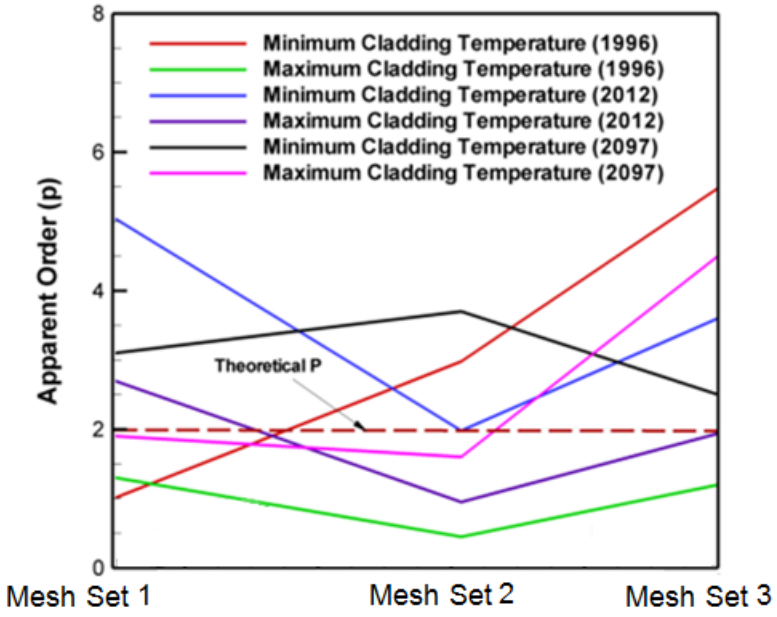

Figure 5-9. Calculated apparent order using different mesh levels for HSM–15

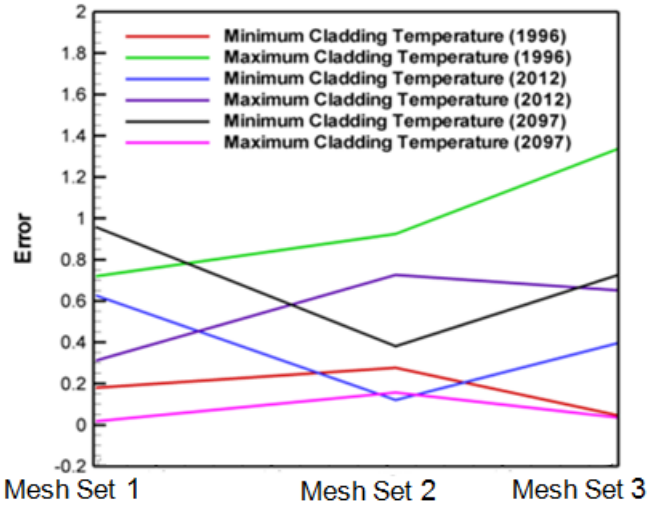

Figure 5-10. Distribution of discretization error with mesh refinement for HSM–15

same combination of meshes used in Figure 5-9. It is clear from the figure that the behavior is not asymptotic with mesh refinement. The convergence coefficient C is plotted in Figure 5-11 using the same combination of meshes. The figure shows that the pattern of distribution for C is also not asymptotic. Hence, Figures 5-10 and 5-11 are suggestive of oscillatory convergence. The possible causes of this pattern are similar to those observed in connection with HSM–1, as discussed in Sections 5.2.2 and 5.2.3. These potential explanations include incomplete iteration convergence, numerical effects such as machine error, complex geometry and flow physics, and limitations in systematic mesh refinement. Since the internal geometrical configurations of HSM-1 and HSM-15 are the same and both involve the same basic flow physics, these factors had similar effects on the HSM-15 solutions and contributed to the nonasymptotic patterns with mesh refinement.

As for HSM-1, a modified approach to calculate GCI for HSM-15 was adopted in order to obtain a useful bound of the simulated results and a realistic numerical uncertainty estimate. The detailed rationale behind the modified approach was explained in Section 5.3.4. A theoretical order of accuracy p=1 was used, instead of the apparent order of accuracy, in order to reflect the fact that some of the equations were solved using first order approximations that would affect the overall accuracy of the solution. In addition, the baseline mesh was used to calculate the GCI values because the benchmark modeling, parametric analysis, and thermal evolution study used the baseline mesh. The mesh refinement factor r_{21} and the relative error term e_a^{21} were calculated using the baseline and coarse mesh simulations. The calculated values of GCI for HSM-15 using this approach are provided in Table 5-12. Again, the small calculated GCI values, even using a lower order of accuracy, indicate limited variability due to mesh refinement.

5.5 Observations from GCI Analysis

The major observations from the GCI and uncertainty analysis are as follows.

- For maximum and minimum cladding temperatures, differences among the solutions from different mesh levels are not significant.

- The apparent order of accuracy calculated using different combinations of solutions was not constant and was in many of the cases higher than the theoretical order of accuracy ($p = 2$).

- A detailed discretization convergence analysis showed that the solutions may not all lie in the asymptotic convergence zone.

- A number of factors may have influenced the calculated order of convergence p and GCI. These include (i) minor variation in the solution even when the system achieved an overall iteration convergence and (ii) machine errors.

- The present problem involves turbulent natural convection through a geometrically intricate domain, in which different aspects of the physics may converge differently, making the determination of GCI a challenging exercise. As mentioned in Section 2.5, the flow behaviors in HSM–1 and HSM–15 both involve the laminar-turbulent transition. With the higher heat load in HSM–15, the flow is even less likely to be in the fully turbulent regime. A modified approach, with a low apparent order of 1 and a high factor of safety, was employed to calculate the GCI.

- The calculated GCI values showed minor variation in results, indicating that mesh refinement may not have a significant impact on temperature calculations for HSM–1 and HSM–15.

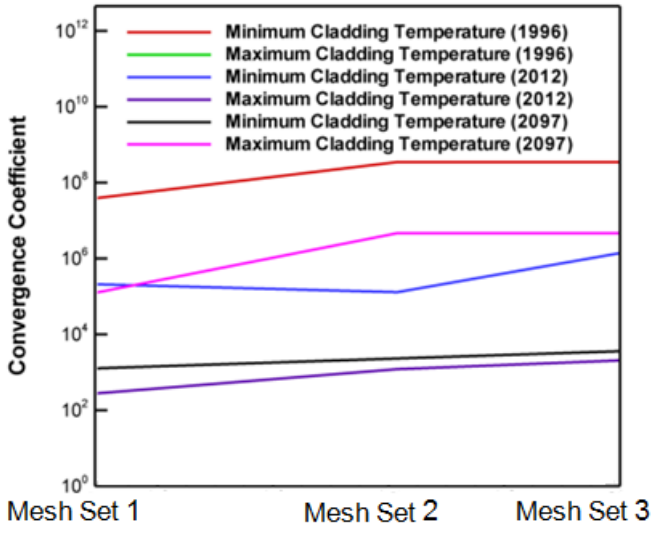

Figure 5-11. Variation of convergence coefficient with mesh refinement for HSM–15

Table 5-12. GCI value for a conservative bounded value of p = 1 for HSM–15 module

Year	Variable	Value from baseline mesh simulation (K) °F = [1.8 K-460]	GCI
1996	Maximum cladding temperature	502.61	0.534
	Minimum cladding temperature	326.49	2.314
2012	Maximum cladding temperature	462.83	0.13
	Minimum cladding temperature	321.66	2.33
2097	Maximum cladding temperature	364.70	0.469
	Minimum cladding temperature	309.21	3.59

6. SUMMARY AND CONCLUSIONS

A three-dimensional (3-D) computational fluid dynamics (CFD) model was developed for ventilated horizontal storage modules HSM–1 and HSM–15 at the Calvert Cliffs Independent Spent Fuel Storage Installation (ISFSI). These horizontal storage modules contain a modified version of the NUHOMS dry storage canister (DSC) that stores 24 pressurized water reactor (PWR) fuel assemblies. Each assembly accommodates a 14 × 14 arrangement of Combustion Engineering (CE) fuel rods. The CFD model, developed using the commercial package ANSYS-FLUENT® Version 14.5, explicitly models the concrete storage units, DSC shells, and internal structures such as spacer plates, tie rods, fuel assemblies, and the supporting rails. The storage system was meshed using unstructured hexahedral grids with mesh refinement in regions expected to have higher gradients of temperature and velocity. Individual fuel rods within a fuel assembly were not represented explicitly; the volume within each fuel assembly was modeled as a continuous porous medium. A separate 3-D CFD model of a fuel assembly was developed to determine the inertial and frictional flow resistance factors, which were used in the study to account for the pressure drop within the fuel assemblies. A separate calculation based on the CE 14 × 14 fuel configurations was done to determine the orthotropic-temperature-dependent thermal conductivity in the fuel assembly area. For the baseline case simulations, the low Reynolds number k-ε model with buoyancy effect was used for the turbulence model. The discrete ordinate (DO) radiation model was used for radiation. The decay heat was specified as a volumetric heat generation rate within the fuel assemblies and was applied over the active fuel length within each fuel region and modified using an axial peaking factor to include axial variation.

6.1 Baseline Simulations and Comparison of Simulated to Measured Temperatures

Baseline simulations for HSM–1 and HSM–15 were performed to understand the flow and temperature field within the storage system. Simulation results yielded buoyancy-driven natural convection flow patterns within the module, in which cooler air enters the system through the opening and absorbs the decay heat, lowering the air density, and the warmed air exits through the outlet vent at the top of the structure. The simulated patterns of temperature distribution for the DSC shell are similar for HSM–1 and HSM–15. The temperature gradually increases toward the mid-section of the DSC from relatively low values at the front and back end sections. This pattern can be attributed to the decay heat load distribution and axial peaking factor and to the asymmetric airlow around the DSC in the axial direction. The high-temperature region on the upper half of the curved surface of the DSC shell is due to the buoyancy-driven upward flow of heated air around the DSC and helium flow within the DSC. The highest simulated temperature for the HSM–15 module DSC shell {391.46 K [245.2 °F]} is significantly higher than the highest simulated temperature for the HSM–1 DSC shell {355 K [180 °F]}. This is principally because the decay heat load is higher in the HSM–15 module. Another factor likely contributing to the lower overall temperature in HSM–1 is the fact that one side of the HSM–1 module is exposed to the atmosphere.

Computed temperatures for the HSM–1 and HSM–15 modules were compared to temperatures measured on June 27 and 28, 2012, as part of the Used Fuel Disposition Campaign of the U.S. Department of Energy [Suffield et al. 2012]. Due to constraints on access to the different regions of the DSC and safety constraints, temperature measurements were obtained only on the DSC shell outer surfaces. The front door of each module was opened to obtain the limited temperature measurements. The simulated temperatures for both modules were, on average, 10–12 K [18–22 °F] higher than the measured values. The differences between the computed

and measured values were smaller on the end cap of the DSC shell and the differences were larger for locations away from the end cap. The measured temperatures have significant uncertainty because of the difficulties in obtaining accurate measurements in the narrow gap between the DSC and storage module wall and may reflect mixing of ambient air with the internal air through the open doors. The measurements also show a relatively flat temperature distribution along the axial direction of the DSC shell top wall; this distribution is unlikely given the magnitude and axial distribution pattern of the heat load. Hence, a thorough assessment of experimental uncertainty is needed to make a meaningful comparison with computed data and use it to assess the validity and accuracy of the numerical solution.

6.2 Sensitivity Analyses

A series of sensitivity studies was performed using the baseline simulation. The following features were studied: (i) near wall mesh refinement, (ii) turbulence model, (iii) porous media resistance, (iv) insolation loading, and (v) extension of computational domain.

A study was conducted by adapting and refining the mesh near the DSC shell outer wall to understand the effects of y+ and mesh spacing on temperature predictions. Three levels of mesh refinement were performed, with surface averaged y+ of 2.974, 1.575, and 0.8193. A comparison of temperature distributions obtained from simulations using these different meshes showed nearly identical values and patterns. Minor deviations were observed near the top of the DSC shell, where the flow is characterized by higher gradients. In general, the close agreement among the simulated temperatures demonstrates that the baseline mesh is adequate for the present study.

The turbulence models considered in the sensitivity analysis included the baseline low Reynolds number k-ε model, the standard k-ε model with scalable wall function and buoyancy effects, the shear stress transport k-ω model with low Reynolds number corrections, and the shear stress transport k-ω model with buoyancy effects. Sensitivity analyses for the turbulence models showed that the simulated results with the baseline low Reynolds k-ε model predicted the lowest temperatures.

For the sensitivity analysis on the porous media model, four cases were simulated: higher porous media resistance than the baseline, lower porous media resistance than the baseline, zero resistance, and no porous media assumption. The study revealed that varying porous media resistance to a higher or lower value compared to baseline did not affect the temperature distribution. However, studies with zero resistance in the porous media and with no porous media showed a relatively flat temperature distribution pattern that is markedly different from the other cases.

A sensitivity analysis was performed to understand the effect of insolation. Comparing temperatures from the baseline simulations (which consider insolation) with temperatures from simulations that omit insolation, the HSM component temperatures specified on the outer surfaces are sensitive to insolation by several degrees, although extreme temperatures are less sensitive.

A separate study was performed to check the accuracy of the convective heat transfer coefficient specified as the boundary condition on the outer walls of the storage modules. This was done by solving the baseline problem using an extended domain that included the surrounding atmosphere, where the external surface heat transfer was calculated from the flow variables in the solution without the need for an explicit specification of the boundary condition.

The average convective heat transfer coefficient calculated from the extended domain study was comparable to the value used in the baseline simulations.

6.3 Simulation of Long-Term Storage Conditions

The baseline computational models for HSM–1 and HSM–15 were used to predict thermal behavior for 300 years of storage. Analyses for the 300-year duration used simulations assumed to be quasi-steady-state at multiple discrete points in time. The steady-state simulations were performed at 5-year intervals for the first 100 years and at 10-year intervals thereafter. 300-year simulations for both HSM–1 and HSM–15 configurations show (i) the drop in maximum cladding temperature with time is relatively rapid in the first 100 years and is gradual thereafter and (ii) the minimum cladding temperature varies only a small amount as time progresses. Both these temperature distributions exhibited an asymptotic decay with increased time to a temperature slightly above the ambient temperature. The time evolution of temperature was also studied for other components, such as spacer plates, the fuel sleeve, and heat shield. All component temperatures showed similar trends of asymptotic decay to a temperature slightly above ambient, similar to the trend observed for cladding temperatures. The general pattern of the temperature variations for the HSM–1 and the HSM–15 modules were similar. However, the simulated temperatures for HSM–15 were consistently higher than the temperatures obtained from the HSM–1 simulations due to the higher decay heat load and location of the HSM–15 module.

6.4 Uncertainty Analysis

Finally, the numerical uncertainty of the simulated temperatures was evaluated using the grid convergence index (GCI) method. The GCI method is based on the principles of the classical Richardson extrapolation approach for calculating discretization error and is widely used to quantify the numerical uncertainty of the computed solution. In the present study the technique proposed by Roache [1998] and modified by Celik et al. [2008] was performed to determine the apparent order p and the GCI. The analysis used the extreme minimum and maximum temperatures for the cladding as convergence criteria of particular relevance to the performance of the storage module.

Four levels of mesh were used in the analysis: the baseline grid, a coarser grid obtained from systematically coarsening the baseline grid, and two levels of finer grids obtained by systematically refining the baseline grid. Simulations at three discrete time points within the 300-year period were performed using these four grid levels for both HSM–1 and HSM–15 to obtain an accurate sense of the numerical uncertainties. The maximum cladding temperature and minimum cladding temperature were selected as the two representative variables for performing the GCI calculations. Other component temperatures are expected to have similar levels of numerical uncertainty as these two variables.

Computed temperature data obtained from simulation runs using different grid levels showed little variation. The apparent order of accuracy (p) calculated using different combinations of solutions at different mesh levels was not constant, indicating oscillatory convergence. In most of the cases, the calculated order p was higher than the theoretical order of accuracy. As a result, the GCI determined using these p values was low, indicating a small band of numerical uncertainty. This is most likely caused by the small differences in temperature from different mesh levels, which disproportionally affects some terms in the equation for apparent order of accuracy and results in an artificially high value of p. Other factors, such as minor oscillations in a solution that shows overall convergence, may have affected the GCI calculations.

An alternative estimate of the numerical uncertainty was calculated using a theoretical order of accuracy p = 1 and a higher factor of safety of 3. This approach accommodated the fact that mixed order methods were used in some of the calculations and the radiative transport equations were solved using a first order technique. Because the benchmark study, parametric analysis, and thermal evolution study employed the baseline mesh, the final GCI calculation used the baseline mesh results. It was found that the GCI is still less than 4 percent, indicating that the level of discretization error in the solution is not significant and the associated numerical uncertainty of the results is low.

7. REFERENCES

Adkins, H.E., J.A. Fort, S.R. Suffield, J.M. Cuta, and B.A. Collins, "Thermal Modeling Studies for Active Storage Modules in the Calvert Cliffs ISFSI," Proceedings of the International High-Level Radioactive Waste Management Conference April 28–May 2, 2013, American Nuclear Society, Albuquerque, New Mexico, 2013.

ANSYS, Inc, "ANSYS FLUENT Version 14.5, User's Guide," ANSYS, Inc, Canonsburg, Pennsylvania, 2012.

ANSYS, Inc, "ANSYS CFDPOST Version 14.5, User's Guide," ANSYS, Inc. Canonsburg, Pennsylvania, 2012b.

Arya, M.S. and M. Keyhani, "Convective Heat Transfer in a Sealed Storage Cask Containing Spent-Fuel Canisters," *Nuclear Science and Engineering,* Vol. 105, pp. 391–403, 1990.

ASME, "Standard for Verification and Validation in Computational Fluid Dynamics and Heat Transfer," ASME V&V 20-2009, American Society of Mechanical Engineers, New York City, New York, 2009.

Bahney, R.H. and T.L. Lotz, "Spent Nuclear Fuel Effective Thermal Conductivity Report," BBA000000-01717-5705-00010 REV00, Prepared by TRW Environmental Safety Systems, Inc., for the U.S. Department of Energy, Washington, DC, Jul 11, 1996.

Banken, G., K. Tavassoli, and J. Bondre, "Validation of Computational Fluid Dynamics Code Models for Used Fuel Dry Storage Systems," Proceedings of the CFD for Nuclear Reactor Safety Applications (CFD4NRS-3) Workshop, Validation and Application of CFD and CMFD Codes to Nuclear Reactor Safety Issues, September 14–16, 2010, U.S. Nuclear Regulatory Commission, Washington, DC, 2010.

Bergman, T.L., A.S. Lavine, F.P. Incropera, and D.P. DeWitt, *Fundamentals of Heat and Mass Transfer,* Seventh Edition, John Wiley & Sons New York City, New York, 2011.

Canaan, R.E. and D.E. Klein, "A Numerical Investigation of Natural Convection Heat Transfer Within Horizontal Spent-Fuel Assemblies," *Nuclear Technology,* Vol. 123, No. 2, pp. 193–208, 1998.

Celik, I. and O. Karatekin, "Numerical Experiments on Application of Richardson Extrapolation With Nonuniform Grids," *Journal of Fluids Engineers,* Vol. 119, No 3, pp. 584–590, 1997.

Celik, I.B., U. Ghia, P.J. Roache, C.J. Freitas, H. Coleman, and P.E. Raad, "Procedure for Estimation and Reporting of Uncertainty Due to Discretization in CFD Applications," *ASME Journal of Fluids Engineering* (Special Publication), Vol. 130, 2008.

Cha, J., S.N. Kim, and K.W. Choi, "Thermal Safety Analysis of a Dry Storage Cask for the Korean Standard Spent Fuel," Paper No. ICEM2009-16159, Proceedings of the 12th International Conference on Environmental Remediation and Radioactive Waste Management (ICEM 2009), Liverpool, United Kingdom, October 11–15, 2009, American Society of Mechanical Engineers, New York City, New York, 2009.

Coleman, H.W. and F. Stern, "Uncertainties in CFD Code Validation," *ASME Journal of Fluids Engineering,* Vol. 119, pp. 795–803, 1997.

Das, K., D. Basu, J. Solis, and G. Zigh, "Computational Fluid Dynamics Modeling Approach to Evaluate VSC–17 Dry Storage Cask Thermal Designs," Proceedings of the CFD for Nuclear Reactor Safety Applications (CFD4NRS-3) Workshop, Validation and Application of CFD and CMFD Codes to Nuclear Reactor Safety Issues, September 14–16, 2010, U.S. Nuclear Regulatory Commission, Washington, DC, 2010.

Elizade-Blancas, F., E. Karaismail, and I.B. Celik, "Application of Error Scaling Method in Conjunction with GCI," Proceedings of the 3rd Workshop on CFD Uncertainty Analysis, October 23–24, 2008, Instituto Superior Técnico, Lisbon, Portugal, 2008.

Gomez, P., E. Araya, and M. Greiner, "Simulations of Heat Transfer Within the Fuel Assembly/Backfill Gas Region of Transport Packages," PVP2005-71070, Proceedings of 2005 ASME Pressure Vessels and Piping Division Conference, July 17–21, 2005, American Society of Mechanical Engineers, Denver, Colorado, 2005.

Harrington, P., "Design and Engineering Update," Presentation to the U.S. Department of Energy, Nuclear Waste Technical Review Board, May 9, 2006, U.S. Department of Energy. McLean, Virginia, 2006.

Heng, X., G. Zuying, and Z. Zhiwei, "A Numerical Investigation of Natural Convection Heat Transfer in Horizontal Spent-Fuel Storage Cask," *Nuclear Engineering and Design,* Vol. 213, pp. 59–65, 2002.

Hoo, S.H., H.C. No, H.M. Kom, and E.H. Lee, "Full-Scope Simulation of a Dry Storage Cask Using Computational Fluid Dynamics," *Nuclear Engineering and Design,* Vol. 240, pp. 4,111–4,122, 2010.

Kern, D.Q., *Process Heat Transfer,* McGraw Hill Publisher, New York City, New York, 1950.

McKinnon, M.A., R.E. Dodge, R.C. Schmitt, L.E. Eslinger, and G. Dineen, "Performance Testing and Analyses of the VSC–17 Ventilated Concrete Cask," TR–100305, Electric Power Research Institute, Palo Alto, California, 1992.

Nishimura, M., H. Shibazaki, S. Fujii, and I. Maekawa, "Natural Convection Heat Transfer in the Horizontal Dry Storage System for the LWR Spent Fuel Assemblies," *Journal of Nuclear Science and Technology,* Vol. 33, pp. 821–828, 1996.

NRC, "Identification and Prioritization of the Technical Information Needs Affecting Potential Regulation of Extended Storage and Transportation of Spent Nuclear Fuel," ML120580143. U.S. Nuclear Regulatory Commission, Washington, DC, 2012a.

NRC, NUREG–2152, "Computational Fluid Dynamics Best Practice Guidelines for Dry Cask Applications," U.S. Nuclear Regulatory Commission, Washington, DC, 2012b.

Oberkampf, W.L. and C.J. Roy, *Verification and Validation in Scientific Computing*. Cambridge University Press, Cambridge, Massachusetts, 2010.

Pelletier, D. and P.J. Roache, *Chapter 13*: *Verification and Validation of Computational Heat Transfer, Handbook of Numerical Heat Transfer,* 2nd Edition, W.J. Minkowycz, E.M. Sparrow, and Y. J. Murthy, editors, John Wiley & Sons, New York City, New York, 2006.

Perry, R.H. and D.W. Green, *Perry's Chemical Engineers' Handbook,* 8th Edition, McGraw-Hill Publisher, New York City, New York, 1997.

Phillips, T.S. and C. Roy, "Evaluation of Extrapolation-Based Discretization Error and Uncertainty Estimators," AIAA-2011-215, Proceeding of the 49th AIAA Aerospace Sciences Meeting including the New Horizons Forum and Aerospace Exposition, American Institute of Aeronautics and Astronautics, Orlando, Florida, 4-7 January, 2011.

Rezende, H.C., A.A. Santos, M.A. Navarro, and E. Jordao, "Verification and Validation of a Thermal Stratification Experiment CFD Simulation," *Nuclear Engineering and Design,* Vol. 248, pp. 72–81, 2012.

Richardson, L.F., "The Approximate Arithmatical Solution by Finite Differences of Physical Problems Involving Differential Equations, With an Application to the Stresses in a Masonry Dam," *Transactions of the Royal Society of London,* Series A, Vol. 210, pp. 307–357, 1910.

Richardson, L.F. and J.A. Gaunt, "The Deferred Approach to the Limit," *Philosophical Transaction of the Royal Society of London,* Series A, Vol. 226, pp. 299–361, 1927.

Roache, P.J., "Conservatism of the GCI in Finite Volume Computations on Steady State Fluid Flow and Heat Transfer," *ASME Journal of Fluids Engineering,* Vol. 125, No. 4, pp. 731–732, 2003.

Roache, P.J., "Error Bars for CFD," AIAA-2003-0408, AIAA 41st Aerospace Sciences Meeting and Exhibit, American Institute of Aeronautics and Astronautics, Reno, Nevada, 2003.

Roache, P.J. *Verification and Validation in Computational Science and Engineering,* Hermosa Publishers, Albuquerque, New Mexico, 1998.

Roache, P.J., "Quantification of Uncertainty in Computational Fluid Dynamics," *Annual Review of Fluid Mechanics,* Vol. 29, pp. 123–160, 1997.

Roache, P.J., "Perspective: A Method for Uniform Reporting of Grid Refinement Studies," *ASME Journal of Fluids Engineering,* Vol. 116, pp. 405–413, 1994.

Rohsenow, W.M., J.P. Hartnett, and Y.I. Cho, *Handbook of Heat Transfer,* 3rd Edition, McGraw-Hill, New York, New York, 1998.

Shibazaki, H., M. Nishimura, N. Takahashi, S. Fujii, and I. Maekawa, "A Study of Heat Transfer Characteristics for a Horizontal Dry Storage System for LWR Spent Fuel Assemblies," *Heat Transfer-Japan Resources,* Vol. 27, pp. 284–298, 1998.

Suffield, S.R., J.M Cuta, J.A. Fort, B.A. Collins, H.E. Adkins, and E.R. Siciliano, "Thermal Modeling of NUHOMS HSM-15 and HSM-1 Storage Modules at Calvert Cliffs Nuclear Power Station ISFSI," PNNL–21788, Pacific Northwest National Laboratory, Richland, Washington, October 2012.

TECPLOT, Inc, "TECPLOT 360 Version 2009," TECPLOT, Inc., Bellevue, Washington, 2009.**Walavalkar, A.Y.** and D.G. Schowalter, "3-D CFD Simulation of a Ventilated Concrete Cask Used for Spent Nuclear Fuel Storage," Proceedings of the WM'04 Conference, February 29 – March 4, 200, Tucson, AZ, Paper WM-4314.

Zigh, A. and J. Solis, "Computational Fluid Dynamics Best Practice Guidelines in the Analysis of Storage Dry Cask," Proceedings of the Waste Management 2008 (WM2008) Conference, Phoenix, Arizona, February 24–28, 2008, WM Inc. Symposia, Tucson, Arizona, 2008.

Zoldners, N.G., "Thermal Properties of Concrete Under Sustained Elevated Temperatures," ACI Publication, Paper SP25-1, American Concrete Institute, Detroit, Michigan, 1970.

APPENDIX A

NATURAL CONVECTION CORRELATION AND MODEL FOR VENT SCREENS AT INLET

APPENDIX A: NATURAL CONVECTION CORRELATION AND MODEL FOR VENT SCREENS AT INLET

A.1 Natural Convection Correlation

Convective heat transfer coefficients were specified at the exposed external surfaces of the horizontal storage modules HSM–1 and HSM–15. This appendix discusses how these coefficients were calculated using correlations for natural convection flows. All these correlations are expressed in terms of dimensionless parameters such as the Nusselt number (Nu), Rayleigh number (Ra), and Prandtl number (Pr).

The Nusselt number is the dimensionless ratio of the convection and conduction heat transfer coefficient and is defined as

$$\mathrm{Nu} = \frac{\mathrm{hL}}{\mathrm{k}} \qquad \text{Equation (A–1)}$$

where

Nu = Nusselt number
h = Convection heat transfer coefficient
L = Length over which convection heat transfer takes place (characteristic length scale)
k = Thermal conductivity of the fluid.

The Prandtl number is a dimensionless number that is the ratio of momentum diffusivity (kinematic viscosity) to thermal diffusivity. It is expressed as

$$\mathrm{Pr} = \frac{\nu}{\alpha} \qquad \text{Equation (A–2)}$$

where

Pr = Prandtl Number
ν = Kinematic viscosity of fluid
α = Thermal diffusivity of fluid.

The Rayleigh number is a dimensionless parameter that estimates the relative importance of convective heat transfer due to buoyancy-driven flow to heat conduction through the gas. It is expressed as

$$\mathrm{Ra} = \frac{\mathrm{g}\beta\Delta\mathrm{T}\mathrm{L}^3}{\nu\alpha} \qquad \text{Equation (A–3)}$$

where

g = Gravitational acceleration
β = Thermal expansion coefficient
ΔT = Temperature difference between the heated surface and fluid
L = Characteristic Length.

The characteristic lengths used in the present study are the vertical or horizontal surface lengths of the external surfaces of HSM–1 and HSM–15. This appendix provides the correlations to calculate the Nusselt number for both horizontal and vertical flat plates. These correlations are

obtained from Rohensow et al. [1998] and Bergman et al. [2011] and were derived for walls with uniform temperatures. Though the external wall surface temperatures of HSM-1 and HSM-15 are not constant, the difference in the maximum and minimum temperature for a surface does not exceed 5K [9^0 F]. Hence, application of these correlations provide a reasonable value of the heat transfer coefficient.

A.1.1 Correlations for Vertical Flat Plates

The Nusselt number for flow over a vertical flat plate with uniform wall temperature in laminar regimes is calculated as follows

$$\mathrm{Nu}_l = \frac{2.0}{\ln[1 + 2.0/(\mathrm{C}_l \mathrm{Ra}^{1/4})]}$$ Equation (A–4)

where

$$\mathrm{C}_l = \frac{0.671}{[1 + (0.492/\mathrm{Pr})^{9/16}]^{4/9}}$$ Equation (A–5)

The Nusselt number in the turbulent region is given by

$$\mathrm{Nu}_t = \mathrm{C}_v (\mathrm{Ra})^{1/3} / (1 + 1.4 \times 10^9 \, \mathrm{Pr}/\mathrm{Ra})$$ Equation (A–6)

where

$$C_v = \frac{0.13 \, \mathrm{Pr}^{0.22}}{\left(1 + 0.61 \, \mathrm{Pr}^{0.81}\right)^{0.42}}$$ Equation (A–7)

Once the laminar and turbulent Nusselt numbers are obtained, they are used to calculate the actual Nusselt number as

$$\mathrm{Nu} = \left[(\mathrm{Nu}_l)^m + (\mathrm{Nu}_t)^m \right]^{1/m}$$ Equation (A–8)

where the constant m = 6 [Rohensow et al. 1998]. Equations (A–4) and (A–6) are valid for 10^{-1} < Ra < 10^{12}.

A.1.2 Correlations for Horizontal Flat Plates

For horizontal plates with uniform wall temperature, the Nusselt number (Nu) for the laminar region is given by

$$\mathrm{Nu}_l = \frac{1.4}{\ln[1 + 1.4/(0.835 \mathrm{C}_l \mathrm{Ra}^{1/4})]} = \frac{1.4}{\ln[1 + 1.677/(\mathrm{C}_l \mathrm{Ra}^{1/4})]}$$ Equation (A–9)

C_l is provided in Equation (A−5).

The Nusselt number for the turbulent regime is given by

$$Nu_t = 0.14\left(\frac{1+0.0107\,Pr}{1+0.01\,Pr}\right)(Ra)^{1/3}$$ Equation (A–10)

Equations (A−9) and (A−10) are valid for $1 < Ra < 10^{10}$.

The actual Nusselt number is based on the laminar and turbulent Nusselt number and is given by

$$Nu = \left[(Nu_l)^m + (Nu_t)^m\right]^{1/m}$$ Equation (A–11)

where the constant m = 10 [Rohensow et al. 1998].

A.2 Modeling of Vent Screens at Inlet

Both the HSM–1 and HSM–15 modules at the Calvert Cliffs Independent Spent Fuel Storage Installation (ISFSI) include a number of screens to protect the inlet and outlet vents. These screens will reduce the effective flow area and cause a pressure drop at the inlet and outlet. In the ANSYS-FLUENT [ANSYS 2012] models of HSM–1 and HSM–15, the inlets and outlets are modeled as vents, where a dimensionless pressure loss coefficient is specified to account for the resistance offered by the screens.

The pressure drop coefficient was calculated using the methodology Perry and Green [1997] suggested for incompressible flows through screens. The following equation [Perry and Green 1997] provides a functional relationship between pressure loss and momentum loss

$$\Delta p = K\frac{\rho V^2}{2}$$ Equation (A–12)

where

Δp = Pressure drop
ρ = Fluid density
V = Superficial velocity based upon the gross area of the screen
K = Pressure loss coefficient, given by

$$K = \left(\frac{1}{C^2}\right)\left(\frac{1-\varepsilon^2}{\varepsilon^2}\right)$$ Equation (A–13)

where

C = Discharge coefficient
ε = Screen porosity.

The discharge coefficient is expressed as

$$C = 0.1263\ln(Re) + 0.2043 \quad (\text{For } Re<20)$$ Equation (A–14)

$$C = 0.1\,(Re)^{0.5}$$ Equation (A–15)

Re is the screen Reynolds number

$$Re = \frac{D_s V \rho}{\varepsilon \mu}$$ Equation (A–16)

where

D_s = aperture length
μ = fluid viscosity

Equations (A–13) through (A–15) show that the pressure loss coefficient is a function of flow velocity. The pressure loss coefficient was calculated for a number of velocities, covering the range expected in the present study. In the calculations, it was assumed that the screens will reduce the flow area by 27 percent, and the aperture length of the screen is 0.0013716 m [0.054 in] [Suffield et al. 2012]. These pressure loss coefficients were specified as a piecewise linear function of normal velocities at the inlet and outlet vents of the ANSYS-FLUENT model.

APPENDIX B

MATERIAL PROPERTIES USED IN THE SIMULATIONS

APPENDIX B: MATERIAL PROPERTIES USED IN THE SIMULATIONS

Table B–1. Properties of air used in the simulations
[Bergman et al. 2011]

Temperature	Specific heat		Thermal conductivity		Viscosity	
	J/kg-K	BTU/lb-°F	W/m-K	Btu/[ft h °F]	Pa-s	lbf-s/ft^2
250 K [−9.7 °F]	1,006	0.2402	0.0223	0.013	1.60×10^{-05}	3.341×10^{-07}
300 K [80.3 °F]	1,007	0.2405	0.0263	0.015	1.85×10^{-05}	3.863×10^{-07}
350 K [170.3 °F]	1,009	0.241	0.03	0.017	2.08×10^{-05}	4.344×10^{-07}
400 K [260.3 °F]	1,014	0.242	0.0338	0.019	2.30×10^{-05}	4.803×10^{-07}
450 K [350.3 °F]	1,021	0.244	0.0373	0.021	2.51×10^{-05}	5.242×10^{-07}
500 K [440.3 °F]	1,030	0.246	0.0407	0.023	2.70×10^{-05}	5.639×10^{-07}
600 K [620.3 °F]	1,051	0.251	0.0469	0.027	3.06×10^{-05}	6.391×10^{-07}
800 K [980.3 °F]	1,099	0.262	0.0573	0.033	3.70×10^{-05}	7.727×10^{-07}

Table B–2. Properties of helium used in the simulations
[Kern 1950]

Temperature	Specific heat		Thermal conductivity		Viscosity	
	J/kg-K	BTU/lb-°F	W/m-K	Btu/[ft h °F]	Pa-s	lbf-s/ft^2
260 K [8.3 °F]	5,193	1.24	0.137	0.079	1.80×10^{-05}	3.76×10^{-07}
300 K [80.3 °F]	5,193	1.24	0.152	0.087	1.99×10^{-05}	4.16×10^{-07}
400 K [260.3 °F]	5,193	1.24	0.187	0.108	2.43×10^{-05}	5.07×10^{-07}
500 K [440.3 °F]	5,193	1.24	0.220	0.127	2.83×10^{-05}	5.91×10^{-07}
700 K [800.3 °F]	5,193	1.24	0.291	0.168	3.50×10^{-05}	7.31×10^{-07}
1,000 K [1,340.3 °F]	5,193	1.24	0.354	0.204	4.46×10^{-05}	9.31×10^{-07}

Table B–3. Properties of concrete used in the simulations
[Zoldners 1970]

Temperature	Specific heat		Thermal conductivity		Density	
	J/kg-K	BTU/lb-°F	W/m-K	Btu/[ft h °F]	Kg/m^3	lbm/ft^3
311 K [100.13 °F]	1046.7	0.25	2.02	1.169	2,242	140
366.5 K [200.03 °F]	1046.7	0.25	1.97	1.139	2,242	140
533 K [499.73 °F]	1046.7	0.25	1.79	1.035	2,242	140
811 K [1,000.13 °F]	1046.7	0.25	1.38	0.798	2,242	140

Table B–4. Properties of carbon steel used in the simulations
[Kern 1950]

Temperature	Specific heat		Thermal conductivity		Density	
	J/kg-K	BTU/lb-°F	W/m-K	Btu/[ft h °F]	Kg/m^3	lbm/ft^3
300 K [80.13 °F]	434	0.103	60.5	34.98	7,845	489.7
400 K [260.03 °F]	487	0.116	56.7	32.78	7,845	489.7
600 K [620.3 °F]	559	0.133	48	27.75	7,845	489.7
800 K [980.3 °F]	685	0.163	39.2	22.66	7,845	489.7
1,000 K [1,340.3 °F]	1,169	0.279	30	17.34	7,845	489.7

Table B–5. Properties of stainless steel used in the simulations [Bergman et al. 2011]

Temperature	Specific heat		Thermal conductivity		Density	
	J/kg-K	BTU/lb-°F	W/m-K	Btu/[ft h °F]	Kg/m^3	lbm/ft^3
300 K [80.13 °F]	480	0.114	15.1	8.73	8,055	502.8
400 K [260.03 °F]	512	0.122	17.3	10.00	8,055	502.8
600 K [620.3 °F]	559	0.133	20	11.56	8,055	502.8
800 K [980.3 °F]	585	0.139	22.8	13.18	8,055	502.8
1,000 K [1,340.3 °F]	606	0.144	25.4	14.68	8,055	502.8

Table B–6. Properties of lead used in the simulations [Bergman et al. 2011]

Temperature	Specific heat		Thermal conductivity		Density	
	J/kg-K	BTU/lb-°F	W/m-K	Btu/[ft h °F]	Kg/m^3	lbm/ft^3
300 K [80.13 °F]	129	0.0308	35.3	20.41	11,340	707.9
400 K [260.03 °F]	132	0.0315	34	19.65	11,340	707.9
600 K [620.3 °F]	142	0.0339	31.4	18.15	11,340	707.9

Table B–7. Emissivity of materials used in the simulations [Bergman et al. 2011]

Material	Emissivity
Stainless Steel	0.46
Concrete	0.9
Carbon Steel	0.65

APPENDIX C

POROUS MEDIA MODEL

APPENDIX C: POROUS MEDIA MODEL

Dry storage canister (DSC) shells hold 24 pressurized water reactor (PWR) fuel assemblies in both the HSM–1 and HSM–15 horizontal storage modules. Each of these fuel assemblies houses an arrangement of Combustion Engineering (CE) 14 × 14 fuel rods. The most accurate method for simulating the fuel assembly would involve explicitly modeling each fuel rod in the assembly, along with all the accessories such as spacer grids and guide thimbles. However, such explicit modeling would be computationally intensive. A widely employed and realistic alternative is to use a continuous porous medium to represent the volume within a fuel assembly instead of modeling all the internal components. In general, the helium flow velocity is expected to be low within the fuel assemblies and characterized by a large pressure drop across the length of the assembly due to the presence of a large number of solid obstacles. In the porous media approximation, predetermined flow resistances are specified in each flow direction to simulate the effect of pressure loss due to the presence of the fuel rods and other obstacles.

In ANSYS-FLUENT, the porous media model uses a volume-based source term in the momentum equation to account for the pressure loss throughout the porous zone [ANSYS Inc. 2012]. The pressure drop due to flow resistance in the porous region is expressed in the following equation

$$\frac{dp}{dx} = \vec{D} \bullet \mu V + \vec{C} \bullet \frac{1}{2}\rho V^2 \qquad \text{Equation (C–1)}$$

where

μ = Viscosity of helium
ρ = Density of helium
V = Velocity magnitude in axial direction
p = Pressure

The first term in Equation (C–1) represents viscosity-dominated (frictional) losses and the second term provides the inertia-dominated loss. The constants C and D are known as inertial and frictional flow resistance factors, respectively. For the present study, these flow resistance factors need to be specified for the actual configuration of the fuel assembly.

To obtain the inertial and frictional flow resistance parameters C and D, a separate analysis was performed using a three-dimensional (3-D) computational fluid dynamics (CFD) simulation of an isolated fuel assembly. The computational domain consisted of a quadrant of the assembly to take advantage of the symmetry in the fuel arrangement. In the axial direction, the computational domain spanned the entire assembly length. Figure C–1 shows a three-dimensional (3-D) view of the entire computational domain. Fuel and control rods were explicitly modeled as solid cylindrical objects. Figure C–2 provides a closer look into the domain and shows the arrangement of fuel and control rods in the quadrant. Table C–1 lists the pertinent dimensions used in this analysis. The computational domain was meshed using a hexahedral mesh, as shown in Figure C–3. At the inlet, a velocity boundary condition was used. At the outlet, a pressure of one atmosphere—that is, a zero gauge pressure—was specified.

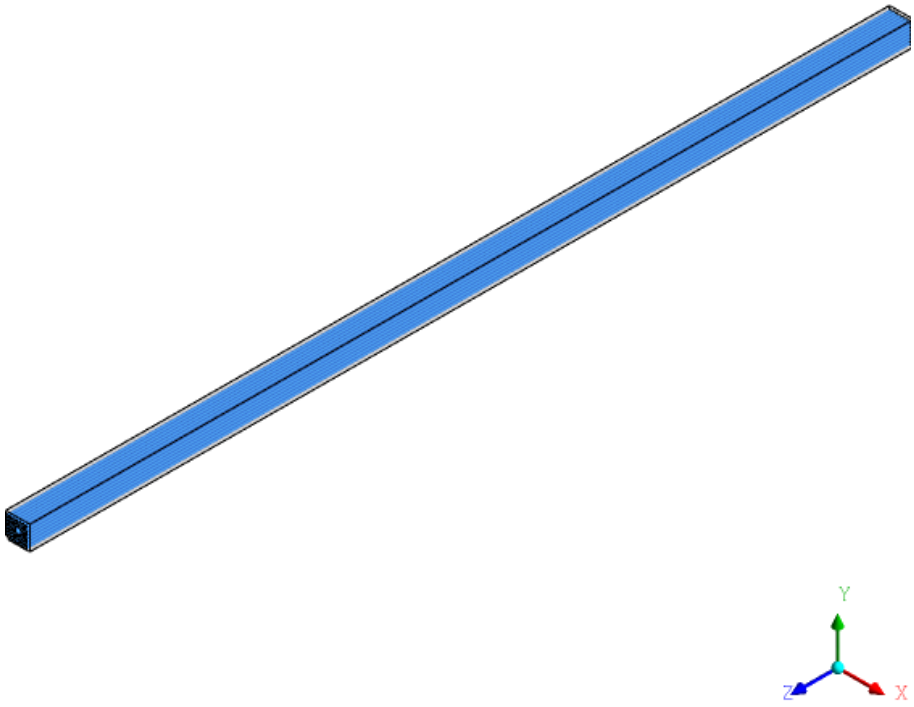

Figure C–1. Longitudinal full view of the computational domain for the CE 14 × 14 fuel assembly for porous media parameter calculation showing the fuel rod

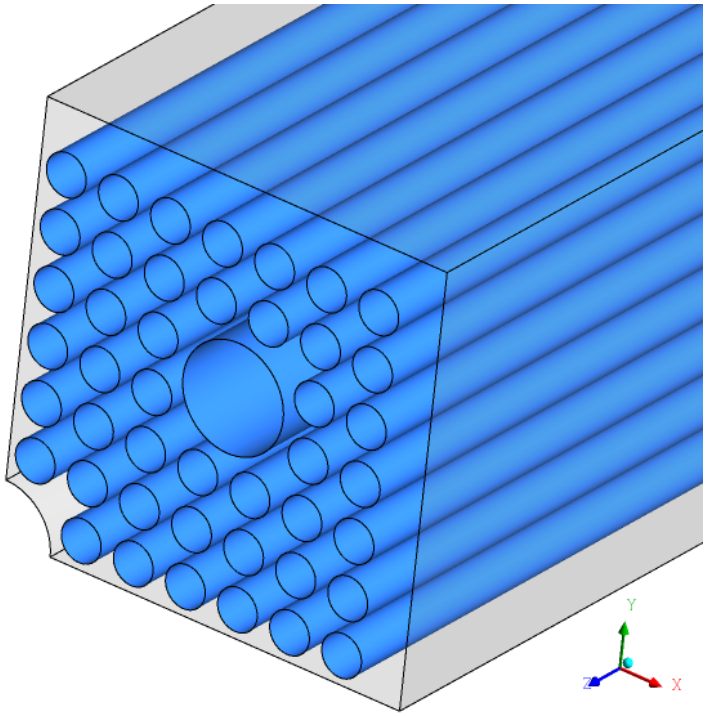

Figure C–2. 1/4th cross-sectional domain for the CE 14 × 14 fuel assembly for porous media parameter calculation

Table C–1. Dimensions used in the simulations

Length of the tube	4.1275 m [13.54 ft]
Fuel rod diameter	0.011176 m [0.037 ft]
Guide tube diameter	0.028321 m [0.093 ft]
Cross sectional area at inlet/outlet	0.007695 m^2 [0.083 ft^2]

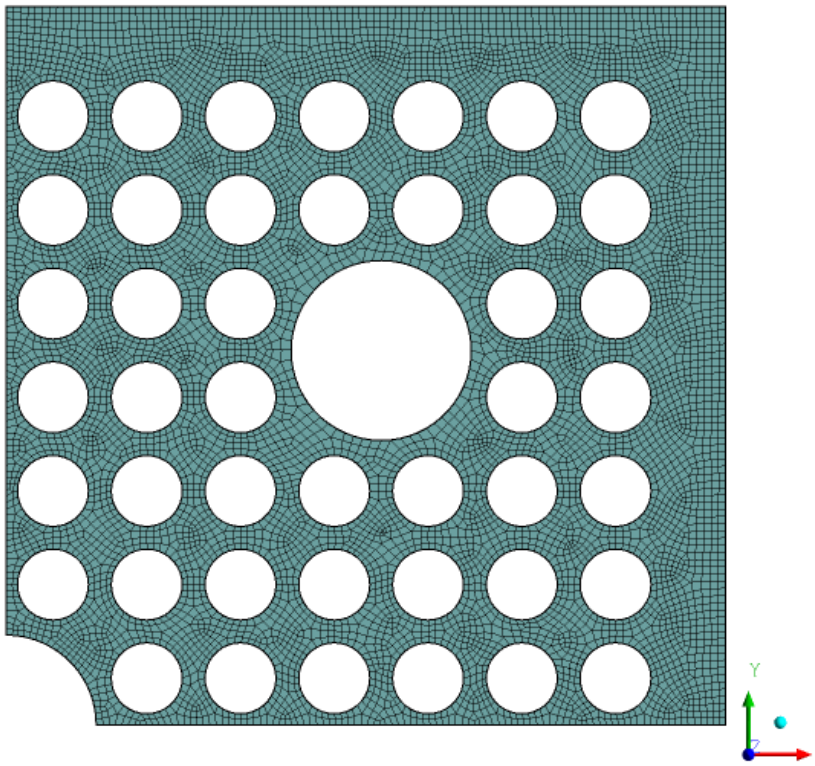

Figure C–3. Two-dimensional view of the computational domain for the CE 14 × 14 fuel assembly for porous media parameter calculation

From Equation (C–1), it can be seen that the pressure drop is a function of velocity through the porous medium. Hence, to determine the frictional and inertial loss factors, the simulations need to be performed for at least two inlet velocity sets. Based on the computed pressure drops obtained from these simulations, the loss factors can be determined. For the present study, a series of inlet velocities was used to cover the range expected under normal operating conditions for the storage system. Using several pairs of the inlet velocity–pressure drop sets listed in Table C–2 , a set of values for C and D in equation C–2 was determined. The average values of the calculated C and D from this set were used in the simulations. The calculated average inertial (C) and viscous pressure loss factors (D) are 0.78 1/m (0.2377 1/ft) and 1.2848×10^5 $1/m^2$ (3730.2883 $1/ft^2$), respectively. Note that these factors are only for the axial flow direction. Due to the presence of the wall and a large number of obstructions, it was assumed that the flow resistances in the transverse directions are much higher. Consequently, arbitrarily high inertial and viscous pressure loss factors (two orders of magnitude higher than the axial direction) was used for the transverse directions. A sensitivity study, reported in Chapter 3, was conducted to assess the effect of the resistance factors.

Table C–2. Inlet condition and parameters for calculation of loss factors

Inlet velocity	Pressure drop (Δp)
0.01 m/s [0.032 ft/s]	0.1056 Pa [2.206×10^{-3} lbf/ft^2]
0.02 m/s [0.064 ft/s]	0.2112 Pa [4.411×10^{-3} lbf/ft^2]
0.04 m/s [0.128 ft/s]	0.4226 Pa [8.826×10^{-3} lbf/ft^2]
0.06 m/s [0.192 ft/s]	0.6342 Pa [1.325×10^{-2} lbf/ft^2]
0.08 m/s [0.260 ft/s]	0.8461 Pa [1.767×10^{-2} lbf/ft^2]
0.10 m/s [0.32 ft/s]	1.0582 Pa [2.21×10^{-2} lbf/ft^2]

APPENDIX D

CALCULATION OF FUEL EFFECTIVE THERMAL CONDUCTIVITY

APPENDIX D: CALCULATION OF FUEL EFFECTIVE THERMAL CONDUCTIVITY

The fuel assemblies inside the dry storage canister (DSC) shell contain a complex arrangement of fuel rods and associated accessories. It would be computationally intensive to explicitly model every fuel rod; therefore, the fuel assemblies are modeled as a continuous porous zone having an anisotropic thermal conductivity. The effective thermal conductivity will represent the effective conduction and radiation heat transfer in the fuel assemblies. The anisotropy in thermal properties is caused by significant differences in thermal conductivities in radial and axial directions. The thermal conductivity in the radial direction is interrupted by gaps between rods that are occupied by helium, whereas in the axial direction, heat flow primarily occurs through the fuel cladding walls. Heat transfer between the fuel rods and assembly walls is dominated by radiation heat transfer, which is dependent on the temperature difference between participating walls, so the effective thermal conductivity is a function of temperature. This appendix describes the analysis that was done to calculate the axial and effective thermal conductivities for the Combustion Engineering (CE) 14 × 14 fuel rods under the storage conditions expected in HSM-1 and HSM-15.

D.1 Radial Thermal Conductivity

To calculate the radial effective thermal conductivity, a two-dimensional (2-D) ANSYS-FLUENT [ANSYS 2012] model was developed to represent an axial cross section of the fuel assembly with fuel rods. The 2-D model is based on a quarter cross section of the CE 14 × 14 assembly and includes the full geometrical details of the fuel rods and Zircaloy cladding. The fuel rods were modeled as a homogeneous solid material region with a specified, uniform heat generation rate. Thermal conductivities of the UO_2 fuel and Zircaloy were used for the fuel and cladding region, respectively. The interstitial space between the fuel rods and the assembly walls was assumed to be occupied by the helium backfill gas and, consequently, the thermal conductivity of helium is used in the interstitial space. The computational domain and the grids used in the 2-D simulations are shown in Figure D–1. A uniform, volumetric heat generation rate {8,522 W/m^3 [824.03 BTU/hr ft^3]} was applied to the fuel region, and uniform temperature was applied to the edges of the 2-D computational domain. The volumetric heat generation rate used in the current analysis was calculated by dividing the total decay heat load of the fuel region by the equivalent volume of the fuel region. Radiation was modeled using the Discrete Ordinate (DO) model. Symmetry conditions were used for the left and lower sides of the domain. Temperature values were specified for the top and right sides of the domain, which represent the outer bound of the fuel assembly.

A number of steady-state simulations were performed for a range of boundary temperatures: 300, 350, 400, and 900 K [80.3, 170.3, 260.3, and 1,160.3 °F]. Figure D–2 shows the temperature distribution for a simulation with an edge temperature of 300 K [80.3 °F]. Based on the temperature distribution and temperature gradient obtained from the series of steady-state simulations, the fuel effective thermal conductivity in the radial direction was determined using the k_{eff} methodology described by Bahney and Lotz [1996]. The values of effective radial thermal conductivities for the fuel region are listed in Table D–1. These values were used in the ANSYS-FLUENT model as an orthotropic temperature-dependent radial conductivity within the fuel assembly, approximated as a porous medium.

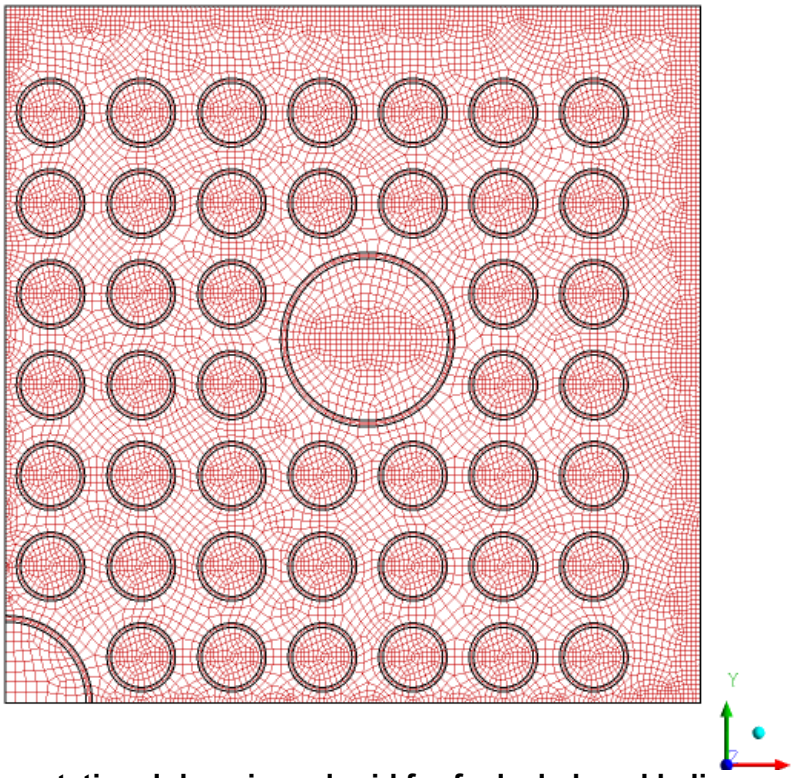

Figure D-1. Computational domain and grid for fuel, clad, and helium gas grids in the effective thermal conductivity calculation

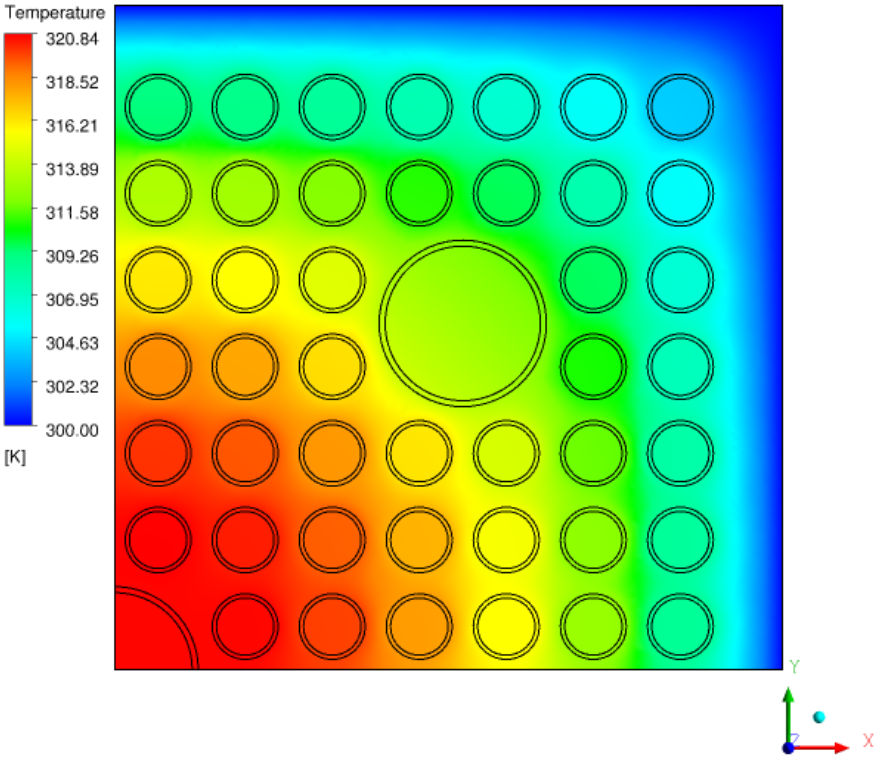

Figure D–2. Predicted temperature contours for an edge temperature of 300 K [80.3 °F]

Table D–1. K_{eff} of fuel region in the radial direction with helium backfill

Temperature (K) [°F]	K_{eff} (radial) (W/m-k) [Btu/(ft h °F)]
307.09 K [93.1 °F]	0.3728 [0.22]
405.08 K [269.4 °F]	0.5203 [0.30]
503.70 K [447 °F]	0.7144 [0.41]
602.74 K [625.26 °F]	0.9647 [0.56]

D.2 Axial Thermal Conductivity

The effective thermal conductivity in the axial direction was determined using an area-weighted average of the thermal conductivities of the materials within the fuel area (i.e., K_{UO2}, K_{helium}, and $K_{Zircaloy}$). The relationship used to calculate the effective thermal conductivity in the axial direction is shown in Equation (D–1).

$$K_{effective} = K_{UO_2} \times A_{ratio-UO_2} + K_{helium} \times A_{ratio-helium} + K_{Zircaloy} \times A_{ratio-Zircaloy} \quad \text{Equation (D–1)}$$

Equation (D–1) uses the area ratio of each material (i.e., $A_{ratio-UO2}$, $A_{ratio-helium}$, and $A_{ratio-Zircaloy}$) with respect to the total area of the cross section of the fuel region and calculates the effective thermal conductivity in the axial direction. The calculated values of temperature dependent effective axial thermal conductivity are presented in Table D–2.

These listed values were specified as temperature-dependent orthotropic effective conductivity in the axial direction within the fuel assembly volumes, approximated as continuous porous media.

Table D–2. K_{eff} of fuel region in the axial direction with helium backfill

Temperature (K) [°F]	K_{eff} (axial) (W/m-k) {Btu/[ft h °F]}
300 K [80.33 °F]	2.5689 [1.49]
400 K [260.33 °F]	2.6250 [1.52]
500 K [440.33 °F]	2.7141 [1.57]
600 K [620.33 °F]	2.7656 [1.6]]

APPENDIX E

FUEL ASSEMBLY LOADING

APPENDIX E: FUEL ASSEMBLY LOADING

The decay heat load was defined for each of the 24 active fuel assemblies within the dry storage canister (DSC) in horizontal storage modules HSM–1 and HSM–15 based on decay heat load data from the Calvert Cliffs Independent Spent Fuel Storage Installation (ISFSI). The fuel structure and fuel identification location for HSM–1 and HSM–15 are shown in Figures E–1 and E–2, respectively. The total decay heat load for the DSC in the HSM–1 module is calculated at approximately 4.1 kW [13,990 BTU/hr] as of June 2012. The total decay heat load for HSM–15 as of June 2012 is 7.6 kW [25,933 BTU/hr]. Tables E–1 and E–2 show the decay heat load values for each fuel region in the HSM–1 and HSM–15 modules as of June 2012. This value of the heat load is divided by the volume of the active fuel region for each assembly and used in the simulations.

The decay heat load was applied as a uniform volumetric heat generation rate over the active fuel length within each fuel region. The volumetric heat generation rate was modified to include the axial variation. This was done by multiplying the volumetric heat generation rate by an axial peaking factor. The peaking factor was based on Combustion Engineering (CE) 14 × 14 representative burn up data from the Calvert Cliffs ISFSI [Suffield et al. 2012]. The data were obtained from a 2006 study at Calvert Cliffs to determine the thermal and radiological source terms for the standard CE 14 × 14 fuel assemblies in the spent fuel pool. The axial variation of peaking factor was implemented as a combination of linear segments in the energy source term specified in the ANSYS-FLUENT model [ANSYS Inc. 2012]. Figure E–3 shows the axial distribution of the peaking factor against nondimensional axial length (length of fuel region). This distribution is used in all the simulations for HSM–1 and HSM–15.

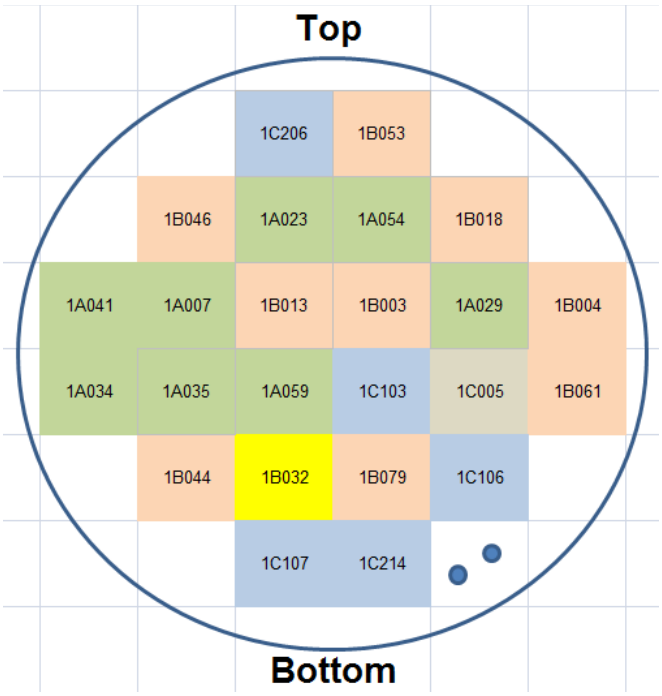

Figure E–1. Fuel assembly loading identification structure for HSM–1 module

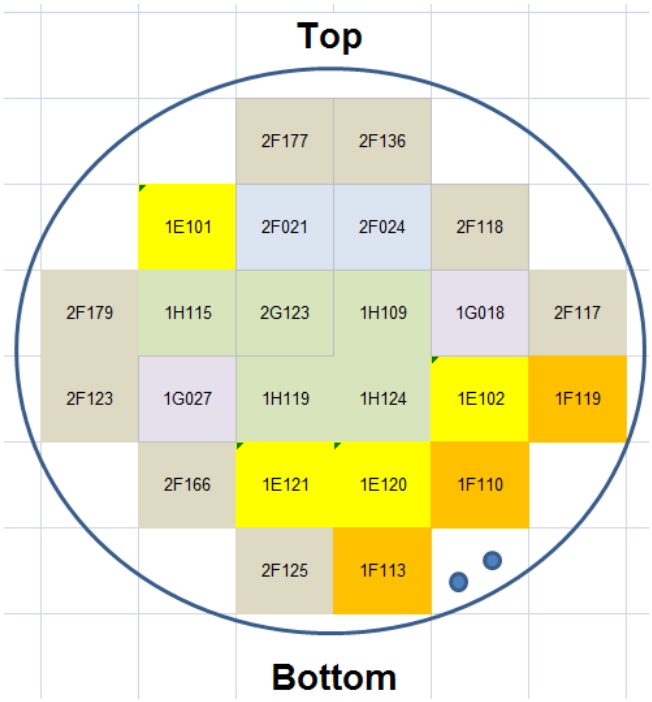

Figure E–2. Fuel assembly loading identification structure for HSM–15 module

Table E–1. Calculated decay heat load values at year 2012 for HSM–1 module

Assembly ID (fuel region) for HSM-1 module	2012 heat load (Current year of measurement) (Watt) 1 Watt = [3.413 BTU/hr]
1A007	130.5
1A034	130.7
1A035	133.0
1A023	137.5
1A041	137.4
1A059	137.4
1A029	138.2
1A054	139.3
1B032	139.9
1B013	183.9
1B053	184.7
1B079	187.4
1B046	192.2
1B044	195.5
1B004	197.8
1B018	197.7
1B061	198
1B003	198.9
1C005	175.2
1C103	189.9
1C107	189.4
1C106	198.3
1C206	202.1
1C214	201.7

Table E–2. Calculated decay heat load values at year 2012 for HSM–15 module

Assembly ID for HSM–15 module	2012 heat load (current year of measurement) (Watt) 1 Watt = 3.413 BTU/hr
2F177	272
2F136	291
1E 101	301
2F021	385
2F024	385
2F118	286
2F179	290
1H115	406
2G123	427
1H109	407
1G018	327
2F117	285
2F123	285
1G027	340

Table E–2. Calculated decay heat load values at year 2012 for HSM–15 module (continued)

Assembly ID for HSM–15 module	2012 heat load (current year of measurement) (Watt) 1 Watt = 3.413 BTU/hr
1H119	408
1H124	407
1E 102	301
1F119	232
2F166	272
1E 121	302
1E 120	302
1F110	225
2F125	274
1F113	225

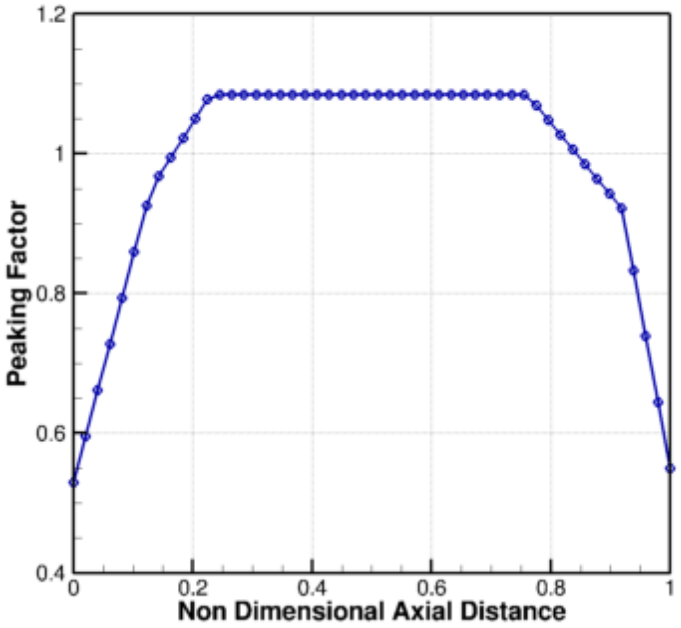

Figure E–3. Axial distribution of the peaking factor used in current simulations

NRC FORM 335
(12-2010)
NRCMD 3.7

U.S. NUCLEAR REGULATORY COMMISSION

BIBLIOGRAPHIC DATA SHEET

(See instructions on the reverse)

1. REPORT NUMBER
(Assigned by NRC, Add Vol., Supp., Rev., and Addendum Numbers, if any.)
NUREG/CR-7191

2. TITLE AND SUBTITLE
Thermal Analysis of Horizontal Storage Casks for Extended Storage Applications

3. DATE REPORT PUBLISHED

MONTH	YEAR
December	2014

4. FIN OR GRANT NUMBER

5. AUTHOR(S)
Kaushik Das, Debashis Basu, Gary Walter

6. TYPE OF REPORT
Final

7. PERIOD COVERED (Inclusive Dates)

8. PERFORMING ORGANIZATION - NAME AND ADDRESS (If NRC, provide Division, Office or Region, U. S. Nuclear Regulatory Commission, and mailing address; if contractor, provide name and mailing address.)
Center for Nuclear Waste Regulatory Analyses
Southwest Research Institute
6220 Culebra Road
San Antonio, TX 78238-5166

9. SPONSORING ORGANIZATION - NAME AND ADDRESS (If NRC, type "Same as above", if contractor, provide NRC Division, Office or Region, U. S. Nuclear Regulatory Commission, and mailing address.)
U.S. Nuclear Regulatory Commission
Office of Nuclear Regulatory Research
Division of Systems Analysis

10. SUPPLEMENTARY NOTES

11. ABSTRACT (200 words or less)
A computational fluid dynamics (CFD) model that can be used to reliably predict temperature distributions for long-term storage was developed for the ventilated horizontal dry storage system containing pressurized water reactor (PWR) fuel at the Calvert Cliffs Independent Spent Fuel Storage Installation (ISFSI). The model was developed systematically by (i) constructing a three dimensional (3-D) model for two horizontal modules at this ISFSI, (ii) comparing model results with measured temperature data, (iii) performing a parametric analysis to assess the impact of model inputs on temperature predictions, (iv) using the developed model to predict temperature distributions of critical components for a storage period of 300 years, and (v) conducting numerical uncertainty analyses of the solutions using the grid convergence index (GCI) method.

12. KEY WORDS/DESCRIPTORS (List words or phrases that will assist researchers in locating the report.)
Horizontal Storage Cask
Extended Dry Cask Storage
CFD

13. AVAILABILITY STATEMENT
unlimited

14. SECURITY CLASSIFICATION
(This Page)
unclassified
(This Report)
unclassified

15. NUMBER OF PAGES

16. PRICE

Federal Recycling Program

UNITED STATES
NUCLEAR REGULATORY COMMISSION
WASHINGTON, DC 20555-0001

OFFICIAL BUSINESS

NUREG/CR-7191

Thermal Analysis of Horizontal Storage Casks for Extended Storage Applications

December 2014